Effects of surface chemical treatment on silicon negative electrodes for lithium-ion batteries: an in situ infrared spectroscopic study

Daniel Alves Dalla Corte

Thèse présentée pour obtenir le grade de
DOCTEUR DE L'ECOLE POLYTECHNIQUE

<u>Spécialité</u>: science des matériaux

Par

Daniel ALVES DALLA CORTE

Sujet

Effets du traitement chimique de la surface d'une électrode négative en silicium amorphe pour batterie lithium-ion: étude par spectroscopie infrarouge in situ

Soutenue le 4 octobre 2013 devant le jury composé de:

Danielle GONBEAU	DR CNRS – UPPA	Rapporteur
Bernard LESTRIEZ	MCF-HDR Univ. Nantes – IMN	Rapporteur
Philippe MARCUS	DR CNRS – Chimie ParisTech	Examinateur
Jean-Marie TARASCON	Professeur – UPJV	Président du jury
Christian JORDY	Ingénieur Dir. Recherche – SAFT	Examinateur
François OZANAM	DR CNRS – École Polytechnique	Directeur de thèse
Michel ROSSO	DR CNRS – École Polytechnique	Examinateur

GENERAL INTRODUCTION

Lithium-ion battery has brought high-energy density, good power performance and no memory effect into the world of portable energy storage devices; nowadays it has become the main power source in mobile electronics applications. Even though it has allowed a great evolution in the field of energy storage, lithium ion battery has not considerably improved its capacity of energy storage since its first commercialization by Sony in 1991. With the constant development of high energy consuming portable devices, the field of energy storage systems searches for a breakthrough technology which will help to fulfill the need for high energy density batteries. In this case, silicon offers the possibility of a significant improvement in the energy density of anode materials, reaching a specific capacity about ten times higher than the typical carbonaceous electrodes present in most of the commercial lithium-ion batteries.

However, when silicon is submitted to a massive lithiation, it undergoes an intense volume expansion which results in a poor capacity retention with along the cycle life. The main strategy to overcome such problems is the use of nanosized silicon geometries. On the other hand, with such a geometry, the surface area of the electrode is maximized and consequently all the surface related side reactions increase. Therefore, the important role played by the solid electrolyte interphase on the performance of lithium-ion batteries becomes an essential factor to be controlled for the development of silicon based electrodes.

The present project started in this context, at the initiative and with the support of SAFT Company. During the internship of A. Kocan, in 2008, preliminary results suggest that silicon surface modification could have a positive impact on the electrochemical performance of amorphous thin film electrodes for lithium-ion batteries.[1] The applied surface treatments were consisting in the creation of monomolecular layers by covalent grafting to the silicon surface. It has therefore been decided in the framework of the present thesis to make a detailed study of those aspects using an in situ analytical technique. For that purpose, coupling of infrared spectroscopy to the electrochemical environment of Li-ion systems has been at the core of the present work. This has been achieved in a geometry of *attenuated total reflection* using thin-film electrodes. The present report is then organized in four successive parts.

In the first introductive chapter, some experimental issues associated to the studies on thin-film silicon electrodes are specifically addressed. These aspects could be at first considered as more or less trivial issues, but they are actually crucial in order to obtain significant, reproducible results. The second chapter is devoted to surface chemical treatments. Various molecular species have been grafted on amorphous silicon surface, and the electrochemical impact of these surface modifications has been closely looked at during the first lithiation/delithiation cycle. The third chapter is devoted to in-situ studies by infrared spectroscopy under electrochemical control. A special attention has been put on the characterization of the SEI layer, for electrodes with a surface modified according to some of the surface treatments previously investigated, and for two different electrolytes. The last chapter is aimed at differentiating between surface phenomena responsible for irreversible processes in Li-ion system, on which surface treatments may have an impact, and bulk phenomena which also contribute to these irreversible processes. For that purpose, a-$Si_{0.9}(CH_3)_{0.1}$:H, a promising material with a bulk composition modified as compared with a-Si:H, has been considered.

Acknowledgments

Firstly, I would like to express my gratefulness towards François Ozanam, Michel Rosso and Thierry Gacoin who jointly advised me over the last years. I was very fortunate to have their support, guidance and friendship. I am also deeply thankful to Ionel Solomon who encouraged me in different aspects of this work.

I am deeply indebted to Christian Jordy and Georges Caillon. Their knowledge and support strongly contributed in this work. Additionally, they were very patient and tolerant with this scientific adventure.

I would also like to thank you Viacheslav Kubytskyi, Nguyen Le Thang Long, Lucie Devys and Jongwook Kim whom I have benefited from discussions of all sorts, for your friendships and support. I am also deeply thankful to all the members of the laboratory for all the care and help. You helped in making these years of work and study a pleasant journey.

Finally, I would like to thank my parents and French family whose love and support have brought me to where I am today.

Summary

Chapter 1 | Silicon as active material for Li-ion batteries

This chapter briefly introduces the principles of Li-ion batteries, demonstrating the challenges on the development of silicon based anode materials. It also reveals important experimental requirements in the study of thin film electrodes.

1 – SILICON AS ACTIVE ANODE MATERIAL FOR Li-ION BATTERIES

1.1 – Introduction to Li-ion batteries

The development of new mobile electronics has regularly increased in the last few years. With the competitive market of smartphones, tablet PCs and electrical vehicles this trend will increase in the following years. This new era of communications and mobility would not have been possible without energy storage solutions to power these mobile devices.

Among a wide range of energy storage systems, secondary electrochemical accumulators are currently the dominant technology for powering portable devices, mostly due to their capability of delivering electrical energy with high power density and rechargeability. This is the case of lithium-ion batteries, which were first commercialized by Sony in 1991 and represented a breakthrough in terms of energy density and high operating voltage.[2]

A lithium-ion system consists of an electrochemical cell containing a positive and a negative electrode separated by an ionic conductor electrolyte. Metal oxides are often employed as active materials for the positive electrode and the negative electrode usually consists of carbon. The electrolyte is imbibed in a porous separator which also acts as a physical barrier avoiding the contact between electrodes but allowing for transporting Li$^+$ ions. Under discharge, lithium ions flow spontaneously from the negative to the positive electrode through the electrolyte. During charge, the ions move in the opposite direction flowing from the positive to the negative electrode, as demonstrated in Fig. 1. Safety issues related to the growth of lithium dendrites and the risk of internal short-circuit on Li-metal batteries contribute to the development of the so-called Li-ion technology, which have both positive and negative electrodes based on Li hosting materials.[3]
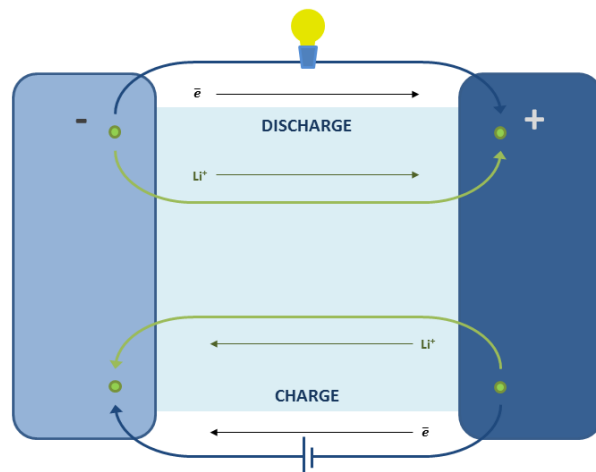
Fig. 1 – Li-ion battery representative scheme.

The quantity of electrical energy that a battery is able to deliver is a function of the cell potential (V) and capacity (mAh g^{-1}), which are related to the intrinsic property of the materials that form the cell electrodes. Energy density is generally expressed per unit of mass (Wh kg^{-1}) or unit of volume (Wh l^{-1}). Fig. 2 represents the energy density of different battery technologies. The evolution of electrochemical energy storage systems can be identified along the improvement on energy density.[3,4]
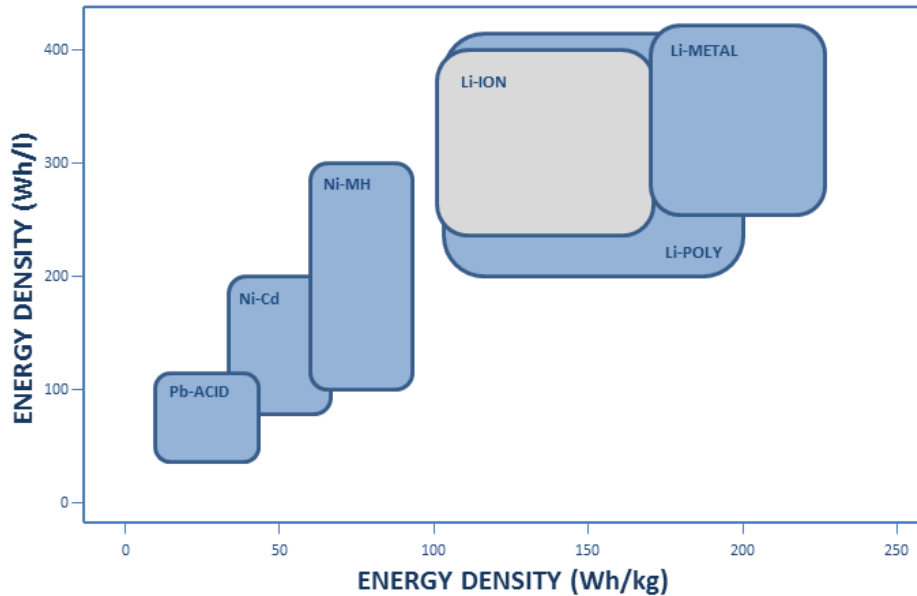
Fig. 2 – Volumetric and gravimetric energy densities of different battery technologies.

Despite the evolution of energy storage achieved by developments on electrochemical accumulators, the capabilities of lithium battery technology are constantly being challenged by the modern multifunctional portable devices which are increasingly requiring higher performance in terms of power density. Energy storage was not able to improve with the same rate as the electronic industry progress.

1.2 – Silicon based Li-ion electrodes

Lithium-ion batteries play an important role in power supplies for portable devices in a wide range of applications, with a great need for improvement in the energy density of the current energy storage devices. In this case, for an effective development of high energy density batteries, the development of high capacity electrode materials, for both positive and negative electrode, is an essential factor. Regarding negative-electrode materials, in general, commercially available systems are based on graphite anodes with a theoretical specific capacity of 372 mAh g^{-1}.
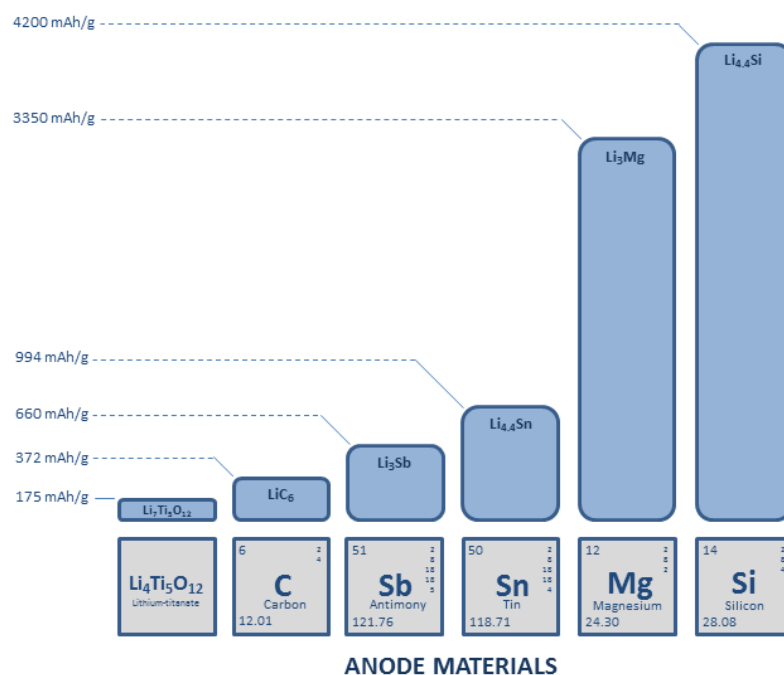
Fig. 3 – Theoretical specific capacity of main anode materials for Li-ion batteries.

As shown in Fig. 3, the specific capacity of carbon is relatively low when compared to promising anode materials. Among them, silicon has been appointed as an important material for the next generation of Li-ion batteries. The use of silicon as negative-electrode material can represent a high improvement in energy density on Li-ion batteries due to its high specific capacity and the low charge/discharge potentials. As compared to graphite, silicon can store a much higher amount of lithium, reaching a theoretical specific capacity of 4200 mAh g^{-1}.[5] It is about 10 times higher than the current technology. Besides, silicon is an abundant element on earth and with technological processes well developed for the industry of semiconductors.

Silicon volume expansion upon lithiation

The high specific capacity of silicon comes from its alloying reaction with lithium, which allows for insertion of up to 4.4 atoms of lithium per atom of silicon. Such a massive quantity of lithium inserted into silicon has harmful consequences to the hosting structure. A metallic Li atom has a radius of 2.05 Å, which is far higher than those of the commonly studied host atoms (Sn: 1.72 Å, Si: 1.46 Å, Sb: 1.53 Å, Mg: 1.45 Å). Because of this steric constrain, a lithiated material will always develop a larger volume than the original unlithiated one. A full lithium insertion into silicon leads to a volume expansion of about 300%.[6]

The volume change of silicon is not dependent on its original structure: both amorphous and crystalline silicon are submitted to similar levels of stress during cycling. As sketched in Fig. 4 the atomic theoretical volume varies nearly linearly during lithiation/delithiation, proportionally to the content of inserted lithium. The values presented in Fig. 4 are strictly applicable for crystalline systems described by the Li-Si phase diagram,[7] however a great similarity of volume expansion is expected for amorphous silicon.
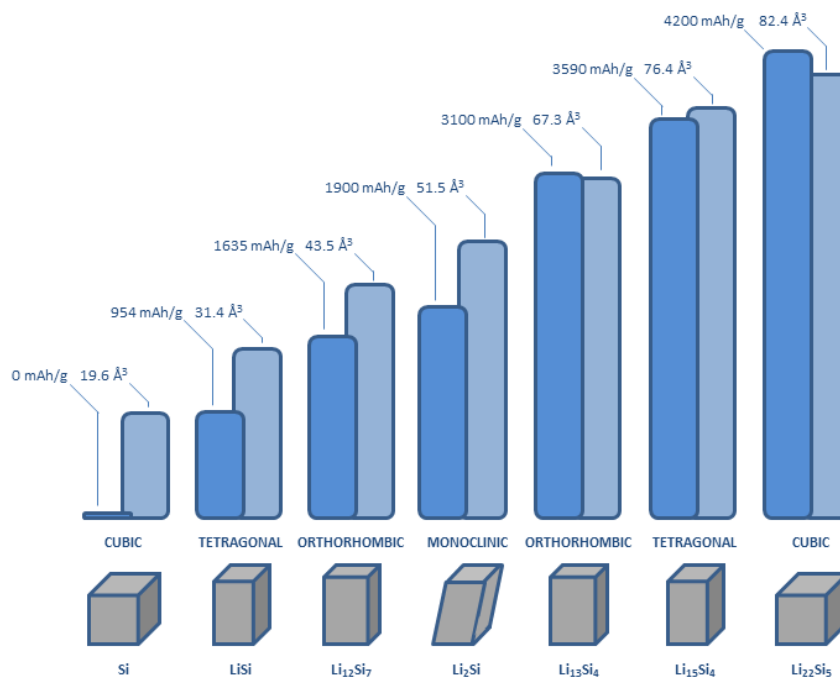
Fig. 4 – Crystal structure, theoretic capacity and volume per Si atom for the Li-Si system.

Crystalline silicon undergoes phase transitions during lithiation, resulting in an amorphous structure after complete delithiation, the so called electrochemically-driven solid-state amorphization phenomenon.[8,9] However, deep silicon lithiation at room temperature leads to a silicon amorphization until approximately a limit of 60 mV vs Li/Li$^+$

and a composition of Li_7Si_2 is reached. Beyond this limit a crystalline $Li_{15}Si_4$ phase is produced.[10] Pursuing silicon lithiation beyond this limit makes the process not totally reversible, since lithium cannot be completely extracted from $Li_{15}Si_4$. Upon delithiation, this crystalline phase turns into an amorphous Li_xSi phase (with x between 1 and 2) which is responsible for a partial irreversible charge.[10] Therefore, in order to avoid the formation of the irreversible $Li_{15}Si_4$ phase we will avoid the use of deep lithiation limits in most part of the electrochemical tests performed in this work. In this case, we assume that once the $Li_{15}Si_4$ phase is not formed, the theoretical specific capacity value for silicon is 3590 mAh g^{-1}, which will be taken as a reference value for all the calculations of specific capacity presented here.

A large volume change in the active material during cycling results in loss of mechanical integrity, cracking, pulverization and the disconnection of the active particles from the conductive current collector.[11,12] The breakdown of the conductive network between active particles and current collector can be evidenced by the rise of the internal resistance.[13] In the case of silicon, compressive stresses are experienced during lithiation as a result of volume expansion. However, initiation and propagation of cracks are normally promoted by tensile stresses instead of compressive stresses. Such phenomena occur during delithiation, where the contraction of silicon results in large tensile stresses, leading to cracking.[14] All these facts contribute to the isolation of lithiated silicon particles, where the delithiation reaction was not completed. In consequence, the electrical access of these residual particles becomes impossible contributing to the irreversible capacity increase encountered on silicon electrodes.

Despite all detrimental consequences from volume change in silicon, important volume changes upon cycling are also faced by the most efficient and popular electrochemical systems – Lead-Acid and Ni-Cd batteries. The negative electrode in Lead-Acid batteries ($Pb/PbSO_4$ reaction) undergoes a volume change of 120%, while the negative electrode of Ni-Cd batteries ($Cd/Cd(OH)_2$ reaction) is submitted to volume expansion of 130%. It exemplifies that the volumetric expansion is not an irremediable drawback and that electrode processing and additives are key issues for the success of an emerging system.[6]

Solid electrolyte interphase formation in Li-ion anodes

In a first approach, the electrochemical processes present on lithium ion batteries appear to be quite simple, basically consisting on reversible exchange of lithium ions between two electrodes. However, in practice the operation of this electrochemical system encompasses more complex aspects.

Lithium-ion batteries work at voltages that are beyond the electrochemical stability of the main organic solvents present in the electrolyte. This high voltage enables such

batteries to deliver high power as well as to promote the reduction and decomposition of the electrolyte. During the first charge of a Li-ion battery, the electrolyte undergoes reduction at the negatively polarized electrode. This process occurs at the interface between electrode and electrolyte at low potentials, consuming charge and lithium ions in an irreversible way. The product of this reaction is basically a mixed layer of Li_2CO_3, lithium alkyl carbonates, lithium alkoxides and other salt by-products (e.g. LiF for electrolytes based on $LiPF_6$ salt); all these species form the so-called solid electrolyte interphase (SEI). Fig. 5 sketches the gradual formation of the SEI by the electrochemical reduction of the electrolyte all along the surface between active electrode material and electrolyte. This decomposition layer is mainly formed at the beginning of the lithiation process, especially during the first cycle.
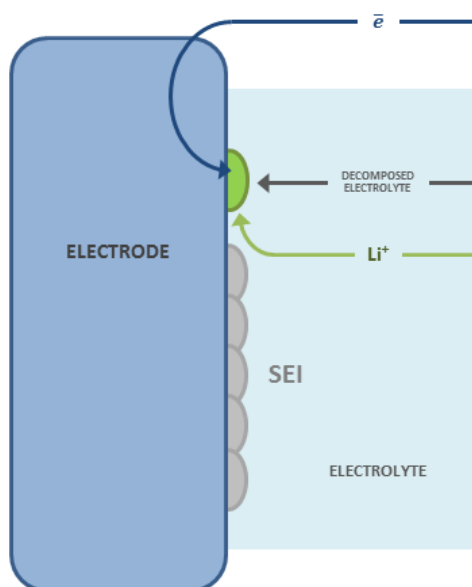
Fig. 5 – Scheme of SEI formation on Li-ion electrodes.

Two competitive reaction mechanisms have been proposed for the electrochemically induced reduction of electrolytes based on carbonated solvents. As shown in Fig. 6, one possible reaction path (reaction I) leads to the formation of a Li_2CO_3 rich SEI layer, with ethylene as a co-product. It is believed that this reaction results in a weakly stable SEI. Another possible reaction path (reaction II) leads to the formation of lithium alkyl carbonate, with a smaller amount of gaseous products, yielding a more stable and compact SEI layer.[15]

Different studies observed that electrode morphology and surface chemistry can affect these two mechanisms, leading to the preferential formation of one of the two species. This preferential effect associated with the electrode characteristics was specifically confirmed for graphite electrodes where the SEI composition of basal planes was found to

be rich in organic products, while the prismatic edge of the graphite structures developed an inorganic composition.[16,17] This gives evidences of the role played by the surface properties on the SEI composition and consequently its effects on the passivation properties. Therefore, by controlling the species present on the electrode surface one can tailor the SEI composition in order to obtain improved passivation properties.
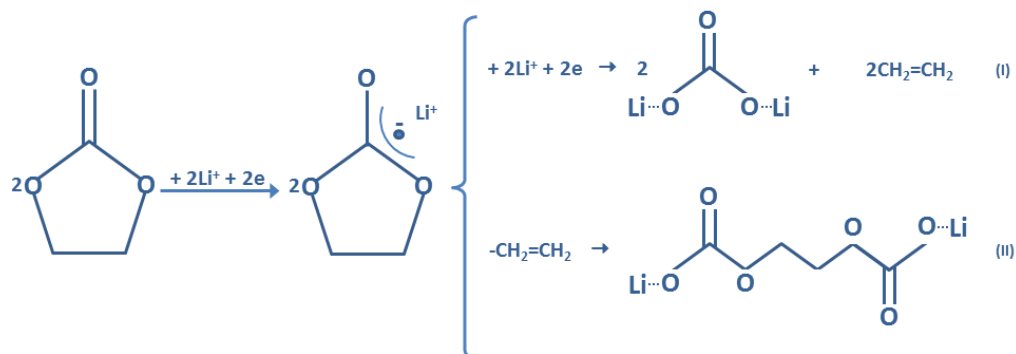
Fig. 6 – Reaction mechanisms for SEI formation.

Even though SEI is formed from the electrolyte partial decomposition and could be thought to be detrimental to the electrode processes, the properties of this layer are unique and play an important role in the entire Li-ion system. The SEI is in first approximation permeable to lithium ions and rather impermeable to other electrolyte components and electrons. The characteristics of the SEI layer formed at the electrode/electrolyte interface can influence the kinetics of lithiation/delithiation and the interfacial stability during prolonged electrochemical cycling. Also, it offers a reasonable protection for electrolyte compounds from further decomposition and prevents electrode from corrosion.[18]

The cycling capability and lifetime in Li-ion batteries are dependent on the nature of the interfaces between electrodes and electrolyte, whereas safety is a function of the stability of the electrode materials and interfaces. Therefore, the performance and safety of Li-ion batteries are intrinsically related to the features of the SEI layer present in the system.

Having in mind the importance of the SEI on the performance of the Li-ion batteries, some electrolyte additives are used to intentionally react during cell operation and chemically coat the active materials with an organic film. Vinylene carbonate (VC) is part of a group of reduction-type electrolyte additives, where the presence of one or more polymerizable carbon-carbon bond makes possible its reduction during cell operation. VC is electrochemically reduced prior to electrolyte solvents, forming an insoluble solid product which decreases the subsequent electrolyte decomposition. The high reduction efficiency of VC makes its presence sufficient for stabilizing the SEI layer even at small concentration (1 to 2 wt.%).[15] In the case of silicon active material VC is responsible for a smooth and uniform SEI formation, allowing for superior electrochemical performances.[19]

Another class of additives may not be reduced during cell operation but will act as a collector for the radical anions formed during the intermediate steps of the electrolyte reduction, or coupling agent with the final products of the SEI, assisting its stabilization.[15] One example of such additives is mono-fluoroethylene carbonate (FEC). Under cell operation, such a compound it is responsible for producing smoother and more stable SEI in silicon electrodes, resulting in improvements in the reversible capacity and coulombic efficiency.[20]

Amorphous silicon thin films

The present study was achieved on silicon thin film electrodes, which constitute a simple system for studying the physicochemical effects of silicon lithiation. This configuration allows for getting more direct information on the silicon electrochemical evolution and electrode/electrolyte interactions, avoiding parasitic effects associated to binders or conducting additive materials. It also allows for using surface-characterization techniques in a well-defined geometry, providing more easily interpretable results.

Hydrogenated amorphous silicon thin film (a-Si:H) electrodes were prepared by plasma enhanced chemical vapor deposition (PECVD) in a low-power regime where silane (SiH_4) molecules are decomposed to form a deposit on the surface of a heated substrate, as schematically shown in Fig. 7. Pure SiH_4 precursor results in a hydrogenated amorphous silicon deposit, where part of the silicon bonds is passivated by hydrogen and where a substantial content of free atomic hydrogen is present in the material. When a mixture of silane and methane (SiH_4/CH_4) is used instead, methyl groups (CH_3) are incorporated in the silicon network producing a so called methylated amorphous silicon deposit (a-Si$_{1-x}$(CH$_3$)$_x$:H).[21]
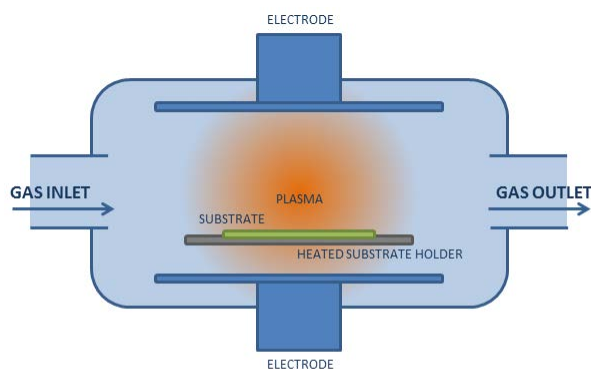
Fig. 7 – Schematic description of a PECVD chamber.

The deposition is usually performed on 250°C heated substrates, with a pressure of 40 mTorr and a SiH_4 flow of 2 L h^{-1}. During the deposition, the SiH_4 plasma is assisted by a 13.56 MHz radio frequency excitation delivering to the plasma a power of 0.10 W cm^{-2}. These parameters result in a deposition rate of 3 nm s^{-1}. The thickness of the electrodes was kept rather thin, varying from 10 to 200 nm, in order to prevent or decrease mechanical electrode degradation of the electrode due to the large volume change during electrochemical cycling and the associated loss of active material. Higher capacity retention

on amorphous thin films upon cycling can be achieved by decreasing the thickness of the film[22] and/or increasing the methyl content concentration.[23]

1.3 – Electrochemical characterizations

At first sight, thin-film based electrodes offer ideal conditions for electrochemical measurements: the planar geometry allows the active surface to be accurately determined. The absence of binder or conductive additives gives intrinsic results related to the thin film material and improved resistance against fracture formation. However, thin-film geometry contains a very small mass of active material, which results in a low value of capacity per area of electrode. In the case of a 100 nm thick a-Si:H electrode (a typical value in the present work), assuming a density of 2.3 g cm^{-3} and a theoretical capacity of 3590 mAh g^{-1}, the cell capacity can be estimated on 59.5 µAh. This value is extremely low, especially when compared with commercial cells (e.g. Sony 18650 cell with a nominal capacity of 2400 mAh).[2] Working with such low capacity values makes any parasite reaction have important consequences on the charge values measured during cell operation. In order to identify and minimize the role played by experimental conditions on the charge consumed during electrochemical cycling, different experimental aspects were tested.

Electrochemical characterization of a-Si:H thin films

Galvanostatic cycling with potential limitation (GCPL) is a method for electrochemical evaluation of battery materials. This technique consists in applying a constant current to the electrochemical cell while its potential is monitored and kept between two potential limits. Each time a potential limit is reached the current is reversed and this procedure is repeated according to the chosen number of cycles. The time (t) under constant current (I) of each step of charge/discharge is used to determine the quantity of electrical charge (C) per mass of active material (m) of the tested material, as Eq. 1 describes. C is commonly expressed in mAh g^{-1} and represents the gravimetric specific capacity of the material.

$$C = I \cdot t / m \qquad\qquad\qquad\qquad \text{Eq. 1}$$

Current density is another important parameter for battery testing. Here the current density is determined as a function of the cycling rate conventionally described as *C/n*, which means that a full charge or discharge of the cell is achieved in *n* hours. For example, assuming that silicon lithiation has a theoretical specific capacity of 3590 mAh g^{-1}, a cell containing 1 g of silicon would charge or discharge in 1 hour using a current of 3590 mA. The same principle of calculation can be applied for thin film electrodes. Table 1 presents the values of capacity and current density calculated for thin film electrodes based on silicon theoretical specific capacity of 3590 mAh g^{-1}, assuming a surface area of 0.72 cm^2 and deposit density of 2.3 g cm^{-3} for a-Si:H.[24]

Table 1 – Theoretical capacity and current density[*] values of a-Si:H thin film electrodes.

Thickness (nm)	C (µAh)	C (mC)	$i_{C/1}$ (µA cm^{-2})
10	5.9	21.2	8.3
30	17.8	64.1	24.8
60	35.7	128.5	49.5
100	59.5	214.2	82.6
150	89.2	321.1	123.9
200	118.9	428.0	165.1

Silicon electrodes and associated lithiation and delithiation reactions represent the half-cell correspondent to the negative electrode in a lithium-ion system. However, for experimental purposes the silicon half-cell is assembled with a lithium half-cell, based on a metallic lithium electrode, where in this case silicon is considered as the positive electrode. Therefore, in a lithium-ion system silicon undergoes lithiation upon charge and delithiation during discharge or vice-versa when using a metallic lithium foil as counter-electrode in electrochemical half-cell.

During the first discharge, the electrolyte is reduced on the negative electrode triggering the SEI layer formation. Subsequently, silicon lithiation starts to take place as moving phase boundary in the electrode.[25] This electrochemical lithiation is characterized by the plateau on the potential (*E*) versus specific capacity (*C*) plot, Fig. 8. After the lower potential limit is reached, silicon undergoes delithiation and the E vs. C curve exhibits a delithiation plateau. From the complete cycle, reversible (Q_{REV}) and irreversible (Q_{IRR}) charges can be determined, as sketched in Fig. 8.

---

[*] Current density for a cycling rate of C/1
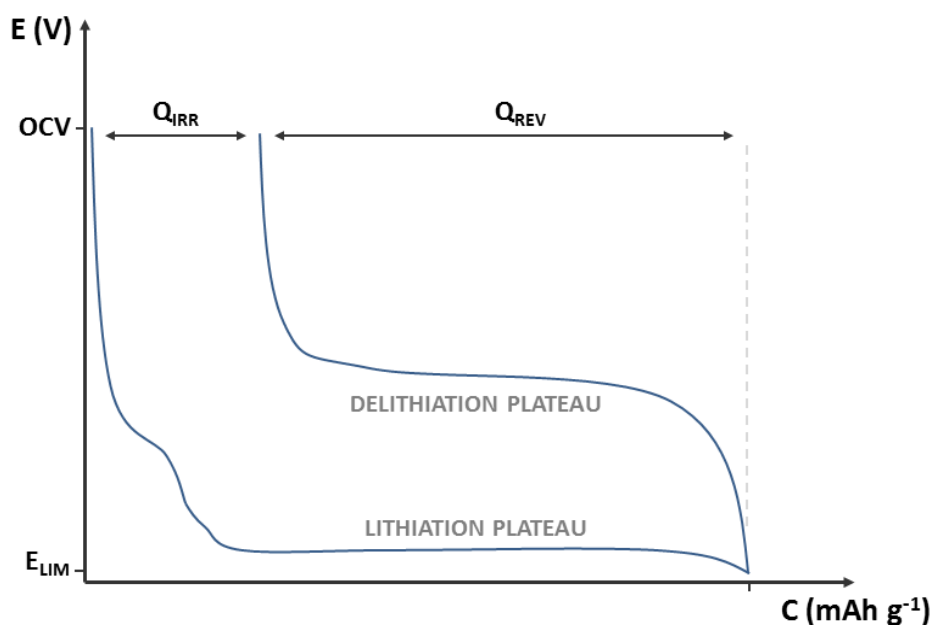
Fig. 8 – Typical electrochemical cycling of silicon.

Cell design and substrate influence on the irreversible charges

Another challenge for the study of thin film materials by electrochemical processes is to determine the surface of contact between the thin film and the electrolyte. The amount of electrochemical signal in a thin film configuration is entirely dependent on the surface area exposed to the electrolyte, highlighting the importance of a precise determination of this experimental parameter. Commercially available cell designs for battery applications are usually not well suited to the study of thin film electrodes. On these common cell designs, the control of the electrode surface in contact with the electrolyte is hardly reproducible. A precise way of certifying this contact area consists in using a standard electrochemical cell where the contact between electrode and electrolyte is achieved through an aperture. This type of electrochemical cell stores the electrolyte and keeps the distance between electrodes constant, avoiding the use of a separator, but at the expense of using a larger electrolyte volume. The coupling of the electrode and the cell is assured by an O-ring seal, enabling a constant area of contact and protecting the system against leakages.

Galvanostatic cycling with potential limitation (GCPL) was performed in different cell geometries in order to check the influence of the cell design on the electrochemical performance of thin film electrodes. Electrochemical experiments were carried out using 1M LiClO$_4$ in propylene carbonate as electrolyte, a 30 nm thin film a-Si:H deposited onto stainless steel as working electrode, a lithium foil mounted on a copper current collector as counter electrode, a current density of 25 µA cm^{-2} and potential limits between 0.01 V and

2 V vs. Li/Li$^+$. Bare stainless steel electrodes were also tested for the purpose of investigating the substrate effect on the electrochemical results.

Two cell designs were tested, one based on a commercially available cell typically employed for testing materials for Li-ion batteries (here called Swagelok-like cell) and the other one based on an O-ring sealed standard electrochemical cell. The first cell makes use of an electrolyte imbibed separator and does not offer any restriction for the excess of electrolyte present in the separator. In comparison, the O-ring sealed standard electrochemical cell offers a precise control of the contact surface between electrode and electrolyte.

As shown in Fig. 9a, the lithiation profile E vs. C of a-Si:H thin film electrodes depend on the cell design used for the experiment. The capacity values are shown in terms of mC in order to compare the results obtained for silicon electrodes with tests performed on bare stainless steel. These tests demonstrate that bare stainless steel react most irreversibly with lithium, representing a source of irreversible charge (gray line in Fig. 9a). In a Swagelok-like cell, schematically represented on Fig. 9b, the excess of electrolyte spreads inside the cell when it is sealed, increasing the area of stainless steel in contact with the electrolyte. This increases the amount of irreversible charge created by side reactions not related to the electrochemical processes on silicon active material. It is assumed that the enormous value of lithiation capacity measured for the thin film in the Swagelok-like cell (black line in Fig. 9a) is due to the contribution of the substrate and internal cell walls in contact with the excess of electrolyte. This problem cannot be minimized by decreasing the quantity of electrolyte present in the separator because, in such cell configuration, the use of a low quantity of electrolyte makes the wetting of the entire electrode surface critical. A reduced amount of electrolyte can also make the system become extremely sensitive to the pressure applied on the separator.

Using a standard electrochemical cell, as schematically represented on Fig. 9c, the lithiation feature of a-Si:H becomes similar to what is observed in the literature[6] (blue line in Fig. 9a), with a capacity value close to the theoretical value (for a 30 nm thick a-Si:H deposit, a value of 80 mC corresponds to about 3700 mAh g^{-1}).
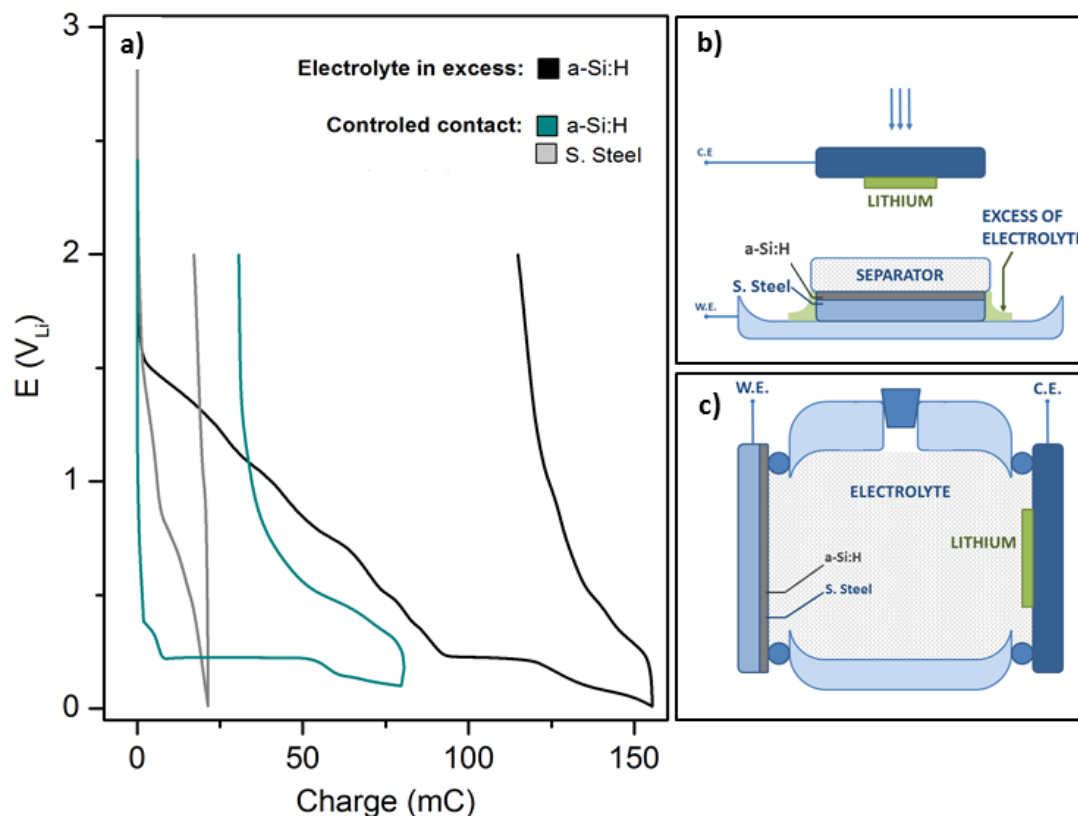
Fig. 9 – Effect of cell designs on electrochemical performance of thin film based electrodes (a) performed in swagelok-like (b) or standard (c) electrochemical cells. a-Si:H electrodes are based on 30 nm thick deposits with theoretical capacity of ≈64 mC (equivalent to 3590 mAh g^{-1}).

Electrochemical measurements on thin film electrodes are also extremely dependent on the surface preparation of the substrates. Charge consumption due to SEI formation is proportional to the real surface area of the electrode. In this case, surface roughness of the substrate play an important role on the electrochemical measurements, justifying the importance of roughness control.

For the purpose of quantifying the roughness of stainless steel substrates, surface profiles were measured using a surface profiler (Dektak 150). On these measurements stainless steel button cells were also tested as one possible option of substrate. As shown in Fig. 10, pristine button cells and stainless steel plates exhibit high average surface roughness (R_a)[†] and important dispersion of results, represented by the standard deviation bars. A reduction in the results dispersion was achieved by simply polishing with emery paper (grain size of 15 µm). The minimal value of R_a and of its dispersion is obtained by polishing with diamond paste (grain size of 1 µm). Surface preparations not only decrease the substrate roughness but also decrease the dispersion of these values, contributing to the reproducibility of the electrochemical measurements.

[†] R_a – Average surface roughness: Arithmetic average deviation from the mean line within the assessment length.
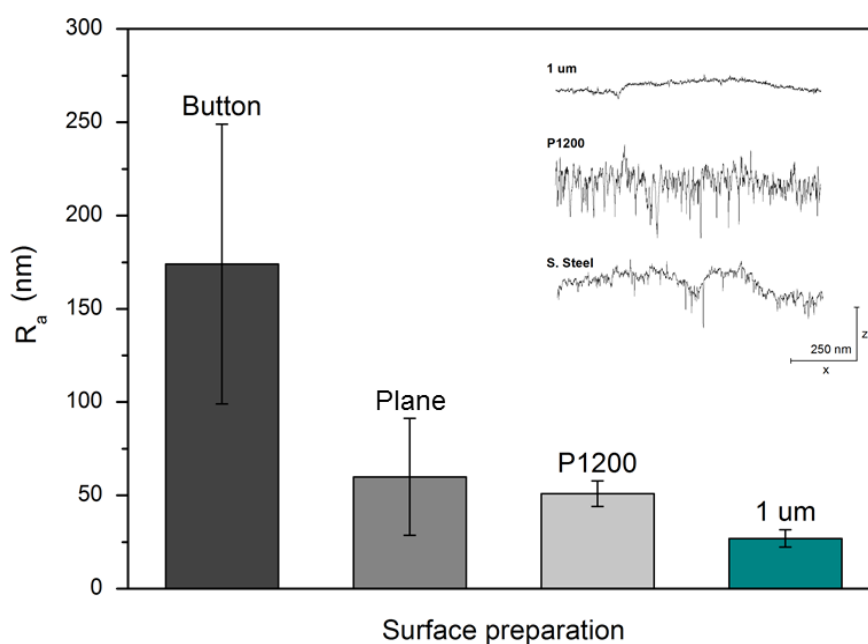
Fig. 10 – Control of substrate roughness by different surface preparations.

Information related to the influence of cell design and substrate preparation on the electrochemical performance were taken into account to set the experimental conditions of the following work. Standard electrochemical cells with compartments containing about 1 ml and electrode apertures of 0.72 cm^2 were used for the electrochemical characterization of most of the materials analyzed in this work. Galvanostatic cycling with potential limitation (GCPL) was performed in standard electrochemical cells, assembled in an Argon filled glove-box, using 1M LiClO$_4$ in propylene carbonate as electrolyte and lithium foil counter electrodes, as previously described. Silicon based electrodes were prepared by depositing a-Si:H of different thicknesses on polished stainless steel substrates. GCPL measurements were performed inside a glove-box, current densities were calculated for cycling rates of C/10 with potential limits between 0.1 V and 2 V vs. Li/Li$^+$.

Fig. 11 shows the first lithiation/delithiation cycles of thin film electrodes of a-Si:H with various thickness from 10 nm to 200 nm. For all the electrodes a lithiation plateau is reached at about 0.24 V vs. Li/Li$^+$, which is related to the movement of the phase boundary between a-Si:H and a-SiLi$_x$:H during lithiation. It is in agreement with the lithiation potential observed for silicon nanoparticles.[26] In the case of crystalline silicon the lithiation potential is expected to be lower, between 0.07 and 0.115 V vs. Li/Li$^+$.[25]

The lithiation capacity is found to increase almost linearly with deposit thickness as expected. Irreversible capacity value is found to be weakly dependent on the deposit thickness, as it is expected if it corresponds only to the SEI formation. However, some

dispersion is observed. A close look at the beginning of the cycle (see insert in Fig. 11) reveals that some additional contribution is recorded before reaching the lithiation plateau for the thinnest deposits.
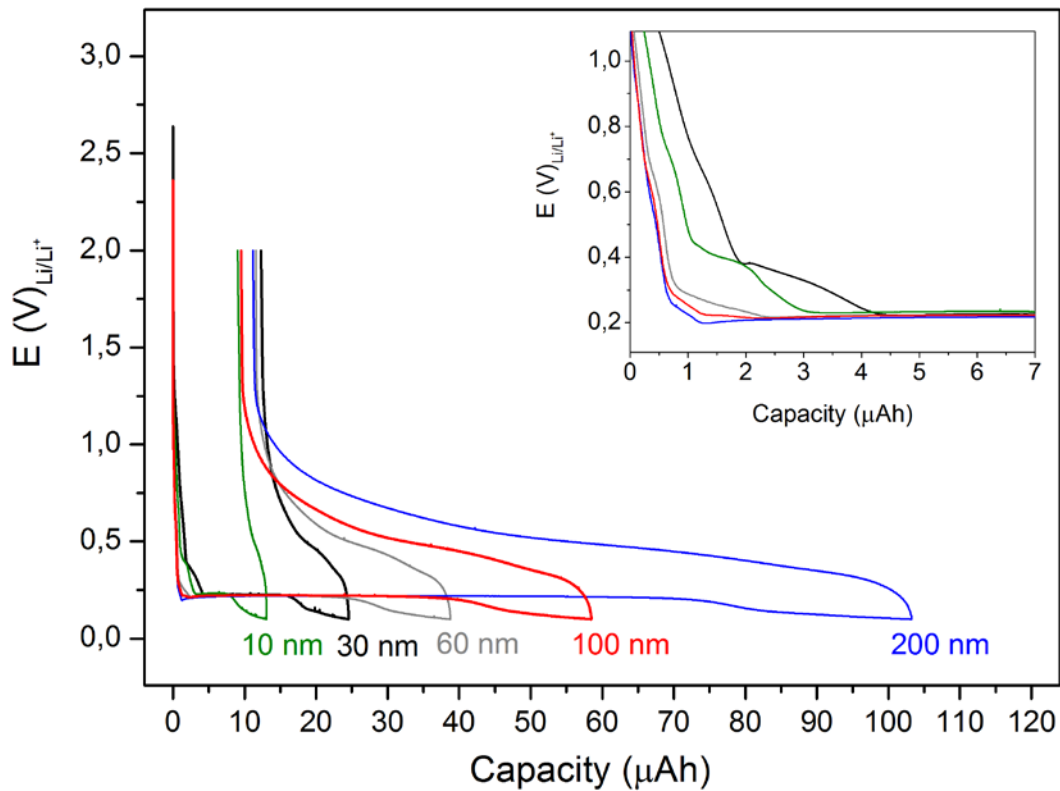
Fig. 11 – Electrochemical cycling of a-Si:H thin film electrodes. Labels indicate the thickness of the thin film deposit and the irreversible capacity as a percentage of the reversible one.

In order to identify the origin of these additional electrochemical reactions present on the thinnest electrodes during their first lithiation, cyclic voltammetry was used. It was performed on a-Si:H films deposited on bare stainless steel, with a thickness varying between 10 nm to 100 nm. The potential was scanned at 0.5 mV s^{-1} starting from open circuit potential until 0.1 V vs. Li/Li$^+$. Cell assembling and characteristics follow the same parameters as those used for GCPL measurements.
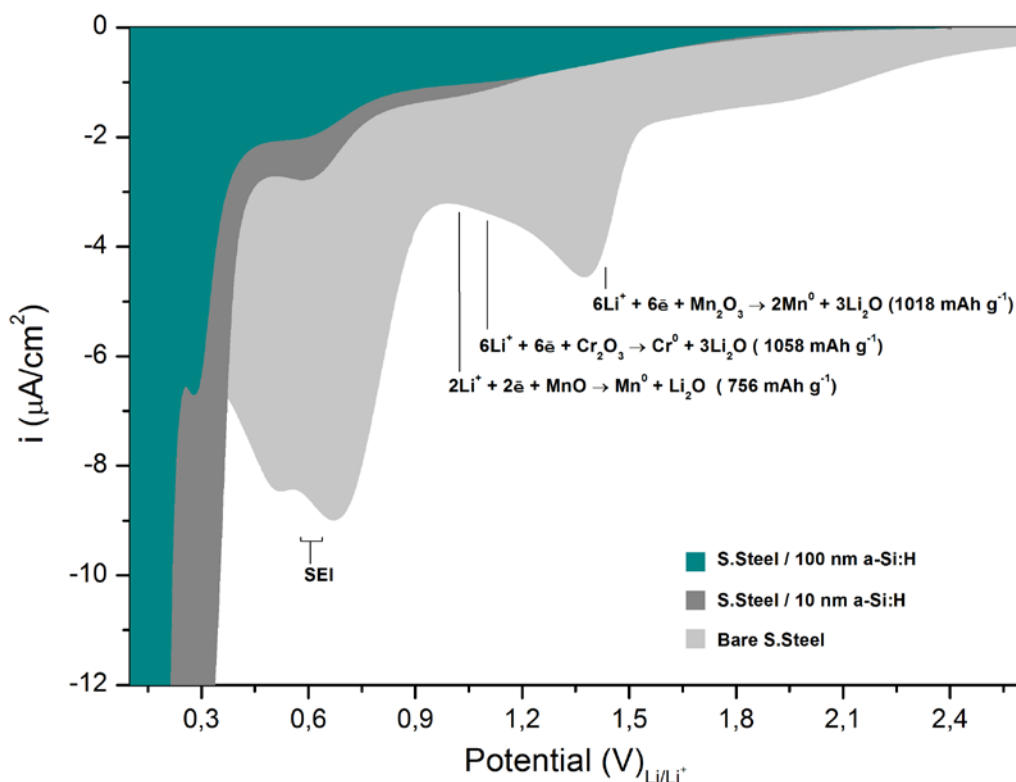
Fig. 12 – Cyclic voltammetry of a-Si:H thin film electrodes and bare stainless steel electrode.

As shown in Fig. 12, a bare stainless steel electrode exhibits intense cathodic reactions. For potentials higher than 0.9 V vs. Li/Li$^+$ the signal corresponds to lithium reactions with alloy elements present in stainless steel. Theoretically, lithium reaction with Chromium and Manganese oxides is responsible for charge consumptions from 758 to 1058 mAh per gram of oxide.[27] However, the oxide conversion reaction undergoes a large irreversibility on the first cycle due to Li$_2$O formation.[28] Cathodic signals from 0.8 to 0.3 V vs. Li/Li$^+$ correspond to the electrolyte reduction and SEI formation[29], signals at lower potentials typically correspond to a-Si:H lithiation[25,26] at the same time as SEI formation continues to take place. [30] Electrochemical lithiation of oxide species present in the substrate does not seem to play an important role on the electrochemistry of a-Si:H thin film electrodes. However, the intense electrochemical reactions detected for stainless steel at potentials around 0.6 V vs. Li/Li$^+$, corresponding to SEI formation, is shown to be also present on the 10 nm-thick electrode and to become very weak for the 100 nm thick one. It demonstrates that stainless steel influence the absolute value of the irreversible charge on very thin electrodes, suggesting the presence of pinholes in the deposits.

1.4 – Conclusion

Along this first chapter it has been explained how electrochemical experiments on thin-film materials differ from conventional powder based electrodes in several aspects. At first, the modest quantity of active material decreases the ratio between lithium electrochemical reactions with silicon and parasite reactions. It makes the charge consumed on electrochemical reactions between substrate and electrolyte, often negligible in usual systems, become an important source of irreversibility. In this case, cell geometry can play an important role on the precision and relevance of the electrochemical results. It was demonstrated that Swagelok-like cells are not suited to perform electrochemical measurements on thin film electrodes and that a standard O-ring sealed cell is appropriate for such experiments. Besides, in thin-film geometry, the mass of active material is also dependent on the surface preparation of the substrate. Controlling the substrate roughness insures the precise control of the amount of active material and increases experimental reproducibility.

It was finally shown that silicon thin films deliver a great specific reversible capacity under electrochemical cycling. In average, about 2800 mAh g^{-1} was reversibly obtained during the first cycle, operating with a relatively high limit of lithiation (0.1 V vs. Li/Li$^+$) and at room temperature. A high irreversible charge during the first cycle was also observed, which has been found to be weakly dependent on the electrode thickness. For the thinnest samples the contribution of the substrate to the irreversible capacity of the electrode may have to be considered, due to the presence of pinholes in the deposit.

Chapter 2 | Surface treatments

In this chapter we explore the possibilities of surface modification of silicon by the grafting of different chemical species in order to limit some detrimental effects of the SEI layer. Grafting characteristics and electrochemical performances of amorphous silicon electrodes are investigated for determining the passivation properties of such molecular layers.

2 – SURFACE TREATMENTS

2.1 – Introduction to surface treatments on electrode materials

As a boundary between active electrode material and electrolyte medium, the electrode interface plays an important role in the performance of the entire electrochemical system. This interface is not only the starting point for lithium permeation into silicon, but also where most of the side reactions responsible for the SEI formation take place. The characteristics of this frontier can impact the kinetics of lithium permeation and the physicochemical properties of the SEI layer.

Naturally formed SEI layer may present an inhomogeneous nature, suffer from partial detachment during cycling and make use of a certain amount of charge during its formation, for which charge is irreversibly consumed for electrolyte reduction during the first cycles.[31] The development of a designed molecular layer, which might be viewed as an artificial inner part of the SEI, can offer an alternative to limit the main disadvantages of a natural SEI. Engineered solid electrolyte interphases may minimize the detrimental reactions associated with the electrode-electrolyte interface, which is the critical part of any electrochemical system.[3]

However, surface modifications on electrode materials must take into account structural and volumetric changes of the electrode during lithiation. Ideally, a stable passivating SEI layer that tolerates or recovers rapidly when damaged by the changes in the electrode volume would improve its lifetime and reduce irreversible charge possess. At the same time, this idealistic SEI must allow for a fast lithium ion transfer between the electrode-electrolyte interface. Simple treatments, such as non-covalent coatings or depositions, have a weak bonding with the active electrode material, limiting their stability. Covalent attachment of organic molecules offers a robust coating for electrode materials. Moreover, if the layer formed by covalent grafting to the surface does not exhibit lateral reticulation between grafted moieties, it is expected to be stable through cycling.

Covalently linked molecular monolayers are a current way of surface modification of silicon substrates, complementing and/or extending the applications of relevant technological materials toward, for example, the development of molecular devices and well-defined sensing interfaces.[32] There exists numerous methods of surface modification by molecular grafting, however, when it comes to the field of energy storage, diazonium chemistry is one of the most usual.[33,34] The electrochemical reduction of diazonium salt generates an organic radical which can attach to the electrodes surface via a covalent bond,

providing an artificial SEI layer composed of at least one molecular monolayer. This method of surface grafting was essentially employed on carbon surfaces where electrochemical performance of graphite based electrodes can be improved by the grafting of polysiloxane[35], nitrophenyl[36] or lithium benzoate[37] multilayer films. Additionally, molecular grafting represents an alternative for improving electronic conductivity of Li-ion electrodes by directly bonding the active material into a conductive matrix[38] or by making use of the grafted layer as a precursor for a conductive carbon coating[39].

Surface chemistry can deeply affect the electrochemical processes in lithium-ion batteries by modifying the mechanisms of SEI formation, leading to layers with different chemical compositions and passivation properties. However, it may happen that a modified surface induces the formation of SEI layers with properties for blocking not only the continuous electrolyte reduction, but also the transfer of lithium ions through the electrode surface, resulting in harming the performance of the entire electrochemical system. In the case of silicon nanowires, the surface coating by methyl or siloxane species leads to highly passivating SEI layers, hindering the bulk lithiation and resulting in weak capacity values.[40]

2.2 – Molecular grafting

Grafting of organic species can be reached by various possible routes and using several chemical schemes different from diazonium chemistry. Silicon offers significant possibilities for a direct covalent Si-C bond, allowing for surface functionalization by innumerous functional groups. Surface modification, or the so claimed *artificial SEI*, can be tailored on different aspects according to the grafted component. Such a wide range of possibilities makes necessary the adoption of an experimental strategy. In this work, linear organic molecules were electrochemically or photochemically grafted on amorphous silicon electrodes in order to establish an artificial SEI layer. Grafted species were varied in order to explore the effects of surface covering density, chain length and functional group termination.

In an important number of molecular grafting cases, surface covering density and molecular chain length are correlated. This correlation is based on the fact that once one molecule is grafted into a surface atomic site it can decrease the probability of a second molecule being grafted in the surrounding atomic sites by steric hindrance effect. This exclusion effect is more effective when the grafted chain is longer and the chain density increases. On the other hand, there are cases where the grafted molecule actually helps grafting the subsequent molecules by creating a new active site for grafting in its close vicinity. When steric hindrance is exceeded or avoided, the dense attachment of molecules leads to the formation of a polymeric brush, with a maximized steric barrier effect. [41,42]

FTIR applied to grafting characterization

Fourier transform infrared spectroscopy (FTIR) is an important tool for studying materials at the molecular level. Infrared radiation can be partially absorbed at specific frequencies corresponding to their vibrational resonances, which allows for identifying functional groups by the vibrational signature of their chemical bonds.

Infrared spectra are obtained by detecting the changes in the transmitted intensity across a probed sample, as a function of the wavenumber. When computed as an absorbance, the intensity of the analyzed signal is linearly correlated to the amount of the probed species present in the sample.[43] In order to enhance the detection sensitivity, the attenuated total reflection (ATR) technique is often used. Such a method makes use of a waveguide crystal allowing numerous reflections to take place between the infrared beam and the sample surface. For each reflection, the infrared beam probes the medium adjacent to the prism along a penetration depth, which corresponds to the spatial extent of the evanescent wave associated with the infrared electric field. This geometry is frequently used for the characterization of molecular grafting, where organic species can be directly grafted onto the ATR crystal. This principle was used here for analyzing the characteristics of molecular layers directly grafted on a thin amorphous silicon layer deposited on the surface of the ATR crystal, as schematically sketched in Fig. 13. Considering the small thickness of the amorphous silicon layer (few nanometers) and its optical similarity with the Si (111) ATR crystal, the presence of the amorphous layer does not introduce sizeable losses for FTIR analyses, hence it does not restricts the applicability of the method. On the opposite, it provides us with a surface environment similar to that used for the electrodes in our experiments. The principles of FTIR and ATR techniques are explained in detail in appendix B and C.
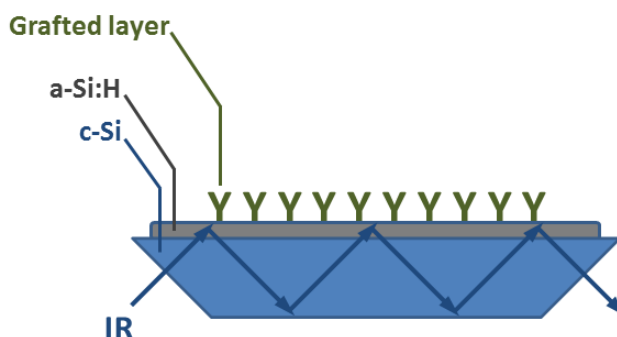
Fig. 13 – ATR-FTIR applied to grafting characterization.

The different surface chemical states associated with the grafted organic monolayers were here characterized by ATR-FTIR spectroscopy using a Bomem MB100 spectrometer, equipped with a liquid-nitrogen-cooled HgCdTe (MCT) photovoltaic detector. Such an experimental configuration provides a wide spectral range for the analysis, from ~980 cm^{-1} to 4000 cm^{-1}. The spectra recorded after surface modifications were compared to that taken before grafting, providing the absorbance change with respect to the hydrogenated amorphous silicon surface.

Hydrogenated surface

A native layer of silicon oxide of 1-2 nm of thickness is expected to be formed on the surface of the as-deposited amorphous silicon layer once it is exposed to air.[44] Therefore, grafting of organic monolayers on oxide-free silicon surfaces by wet chemical routes necessarily starts with the chemical etching of the silicon oxide layer and the saturation of the exposed surface bonds.

Surface hydrogenation is the usual passivating agent present at the surface after oxide removal from silicon surfaces. Alternative strategies of surface passivation can be obtained relying on halogens such as iodine or chlorine.[45,46] Hydrogen-terminated silicon surfaces can be prepared by chemical etching in fluoride-containing solutions. This type of hydrogenation became an attractive procedure for surface preparation because of its ease of preparation, relative stability in air and during brief time in water, and due to the lack of appreciable reactivity toward a range of common solvents (including acetonitrile, diethyl ether, chlorobenzene, hexane, toluene and mesitylene).[32]

The silicon etching in hydrofluoric acid was originally thought to lead to a fluoride terminated surface due to the high strength of the Si-F bond ($\approx$ 5.0 eV).[47] Schematically, the high electronegativity of fluorine is used for removing the oxygen atoms from the silicon surface by replacing Si-O bonds by Si-F. Back bonds of the fluorinated silicon atoms will then become strongly polarized due to the electronegativity of F, allowing for the silicon atom dissolution by insertion of a HF molecule in the polarized bond, which results in leaving Si-H termination at the surface, as sketched in Fig. 14. This mechanism results in a hydrogen-terminated surface.[48] A more complete picture should take into account the role of water species, especially OH$^-$ ions.[49,50]
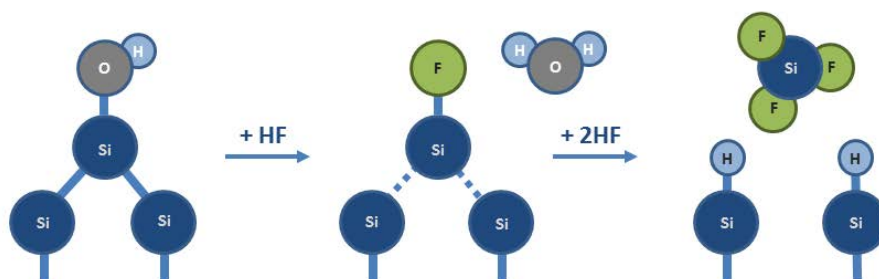

Fig. 14 – Simplified scheme of the mechanism of silicon oxide stripping and silicon hydrogenation by HF in aqueous solution. Notice that the final products of the etching are actually SiF$_6^{2-}$ ions.

In this work, all the amorphous silicon deposits were exposed to air after the deposition process. All the samples were taken out from the deposition chamber at air

contact before being cooled and stored in an Argon filled glove-box. Therefore, the surface of pristine deposited layers is covered with a thin native oxide film.

Oxidized silicon surfaces are easily identified by FTIR. SiO_2 typically exhibits three infrared absorption bands, common to all the polymorphs and located at frequencies in the range of 480 cm^{-1}, 800 cm^{-1} and 1100 cm^{-1}. These infrared signals correspond respectively to Si-O bending modes, symmetric and asymmetric stretching modes of Si-O-Si units.[51] However, the asymmetric stretching vibration mode is very sensitive to the oxygen stoichiometry of the oxide and can vary linearly with the oxide composition. SiO_x oxides (x ≤ 2) exhibit vibrational frequencies varying from 1075 cm^{-1}, for a stoichiometric oxide, decreasing until 940 cm^{-1} for oxides with low oxygen content. [52,53,54] In amorphous SiO_2 the disorder-induced mechanical coupling of the transverse optically active oxygen asymmetric stretch at 1076 cm^{-1} with the longitudinal optically inactive oxygen asymmetric stretch are responsible for generating the infrared absorption shoulder observed between the 1076-1256 cm^{-1}.[55,56]

Deoxidized surfaces were obtained by sample exposition to HF vapor for 10 s. This technique has found to be efficient for removing most of the oxidized species from the surface of amorphous silicon thin films. Fig. 15 demonstrates that even an intensively oxidized surface (oxidized in a H_2O_2:H_2SO_4 (1:3) solution) can be almost completely re-hydrogenated by HF vapor exposition. Notice that the hydrogen content of the HF-vapor treated surface is similar to that of the surface immersed in HF solution and that only a minute amount of oxide is detected at the HF-vapor treated surface.
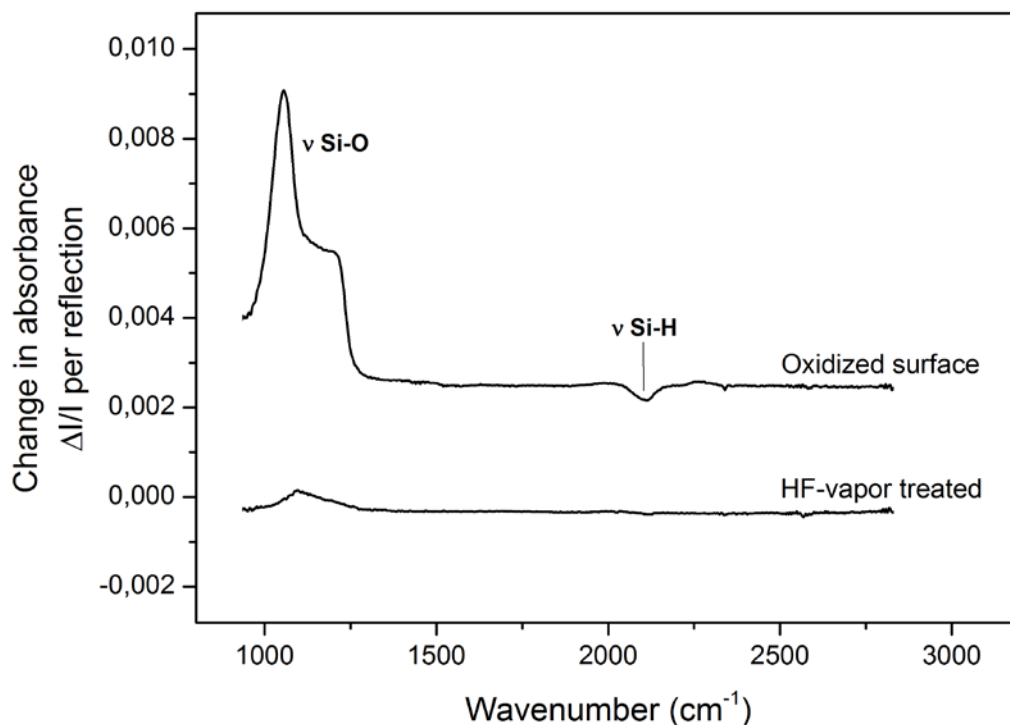
Fig. 15 – ATR-FTIR of oxidized and HF vapor treated a-Si:H surfaces.
Both spectra referred to the surface hydrogenated by immersion in HF solution.

All the spectra in Fig. 15 are referred to the spectrum of the same amorphous silicon deposit hydrogenated by immersion in a HF concentrated solution for 1 s. This wet treatment leads to a complete surface hydrogenation, but also represents a risk of excessive silicon etching, especially for amorphous silicon, and corrosion for metallic substrates. The use of etching by HF vapor avoids such a risk of chemical dissolution, but it also leads to some surface contamination with Si-F.[57]
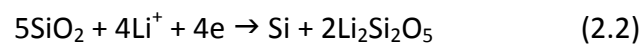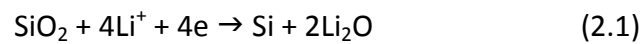
The intense signals of SiO_x stretching vibrations (1000 – 1300 cm^{-1}) present on the oxidized surface practically disappear after HF vapor hydrogenation. By comparing the integrated values of band intensities, it appears that the oxide content was decreased to about 8% after hydrogenation. Moreover, HF vapor is capable of yielding a surface covered by Si-H bands (revealed by the absorption peak at ~2100 cm^{-1}) in the same amount as those present in the reference hydrogenated spectra.

The electrochemical performance of all the surface-modified amorphous silicon layers described in this chapter were tested by recording one electrochemical cycle. For this purpose, a 30 nm thick layer of a-Si:H was deposited on mirror polished stainless steel substrates submitted to the different experimental process of surface grafting described in the appendix A. Electrochemical tests were performed in O-ring sealed electrochemical cells using 1M $LiClO_4$ in propylene carbonate as electrolyte and lithium foil mounted on a copper current collector as counter electrode. Galvanostatic cycling with potential limitation (GCPL) was performed at the rate of C/10, based on the theoretical value of capacity calculated for the 30 nm thick a-Si:H layer (17.8 µAh) and an exposed surface of 0.72 cm^2. The potential was limited from open-circuit voltage (OCV) to 0.1 vs. Li/Li$^+$ during silicon lithiation and from 0.1 vs. Li/Li$^+$ to 2.0 vs. Li/Li$^+$ during delithiation. A systematic study of different experimental parameters was performed in the first chapter, and resulted in an optimized testing setup which allows for good reproducibility of the electrochemical results presented here.

The results of electrochemical tests demonstrated the positive effects of surface hydrogenation on the performance of amorphous silicon based electrodes. As shown in Fig. 16, the removal of surface oxides decreases the charge irreversibly lost during the first electrochemical cycle. This can be experimentally evidenced by comparing the values of lithiation and delithiation capacities measured for hydrogenated samples (black line) and for pristine layers (gray line). The hydrogenation decreases the lithiation capacity by 100 mAh g^{-1}, the irreversible capacity by 520 mAh g^{-1}, increases the coulombic efficiency by 10% and decreases the irreversible capacity (calculated as a percentage of the reversible capacity) by about 32%. In both cases the electrochemical cycling presented similar aspects, such as electrolyte decomposition starting from about 1.3 V vs. Li/Li$^+$ with an intensive SEI formation from 0.4 V vs. Li/Li$^+$, and a lithiation plateau at 0.230 V vs. Li/Li$^+$. The high values of lithiation capacities, exceeding the theoretical value of 4200 mAh g^{-1}, demonstrate that the charge is being used not only for silicon lithiation but also for side electrochemical reactions, such as the electrolyte decomposition.

It therefore appears that surface hydrogenation not only is necessary for the directly covalent grafting of organic molecules into silicon but also can play an important role on the lithiation and delithiation processes. Even though the pathway and final products resulting from the conversion of the native oxide layer by reacting with lithium are still uncertain, the presence of the oxide layer has consequences on the electrochemical performance of silicon based electrodes, as shown in Fig. 16. The SiO_2 reduction expected from Eq. 2.1 is assumed to be kinetically impossible.[58] However, SiO_2 can be converted to silicate forms according to Eq. 2.2 and Eq. 2.3.[59]

$$SiO_2 + 4Li^+ + 4e \rightarrow Si + 2Li_2O \qquad (2.1)$$

$$5SiO_2 + 4Li^+ + 4e \rightarrow Si + 2Li_2Si_2O_5 \qquad (2.2)$$

$$2SiO_2 + 4Li^+ + 4e \rightarrow Si + Li_4SiO_4 \qquad (2.3)$$

The presence of the native oxide layers on the surface of electrode materials could therefore contribute to the initial irreversible capacity through its electrochemical reduction. It could also represent a barrier for bulk lithiation, since SiO_2 is a Li-ion insulating material. This might avoid the complete lithiation of the silicon electrode, decreasing the specific capacity and increasing the interfacial charge transfer impedance.[59]
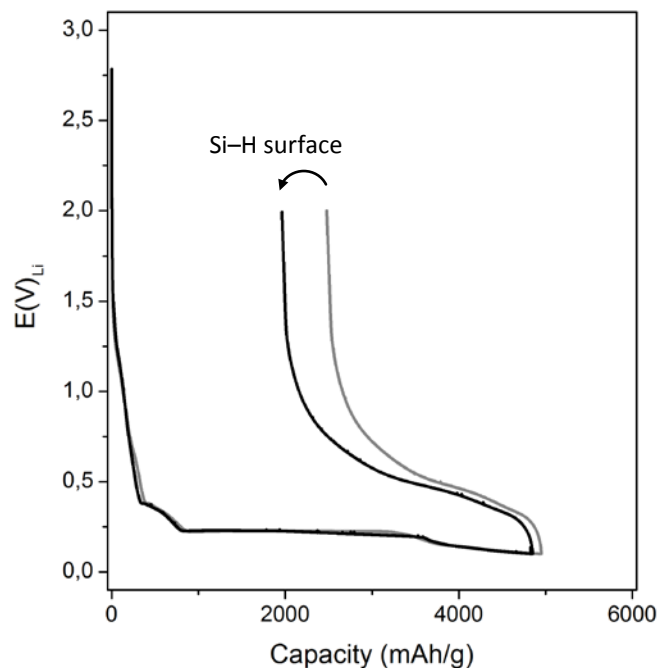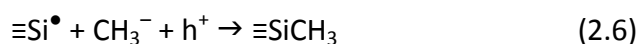

Fig. 16 – Electrochemical cycle of a-Si:H deposits on steel substrates.
Hydrogenated surface (black line) and pristine surface (gray line).

Surface methylation

A perfect passivation of all the silicon atomic sites present on the surface of a silicon crystal is only possible by hydrogen termination. However, hydrogenated surfaces exhibit limited chemical stability, being oxidized under normal conditions of pressure and temperature. Stable grafted layers are often obtained by molecular grafting of long molecules, however the Van der Walls radius of molecular chains prevents the complete surface passivation due to steric hindrance between adjacent grafted units, regardless the chemical strategy used for the grafting. As a noticeable exception, the methyl group is one of the few species with a size compatible with a complete saturation of all the surface silicon dangling bonds.[60] The distance between silicon surface sites on Si(111) surfaces is 3.8 Å, while the van der Waals radius of a methyl group is ca. 2 Å. The later value seems slightly too large for making a complete substitution of all surface Si-H bonds possible. However, a proper orientation of the neighboring methyl groups makes such a substitution possible and complete methylation of the silicon surface has been demonstrated.[60]

In the present work, silicon surface methylation was obtained by anodic treatment in organic anhydrous electrolyte composed of 3M CH_3MgI in diethyl ether. Detailed experimental procedures are presented in the appendix A. The surface methylation starts from the hydrogenated silicon surface and first requires the breaking of Si-H bonds, which is obtained either by anodization at positive enough potentials or through anodic generation of organic radicals and further reaction of these radicals with the surface. The resulting silicon dangling bonds can then be grafted in the presence of a second radical according to different reaction paths, as summarized by the following reactions, where h^+ stands for silicon hole: [61]

$$\equiv Si^\bullet + CH_3^\bullet \rightarrow \equiv SiCH_3 \qquad\qquad (2.4)$$

$$\equiv Si^\bullet + CH_3MgI + h^+ \rightarrow \equiv SiCH_3 + MgI^+ \qquad (2.5)$$

$$\equiv Si^\bullet + CH_3^- + h^+ \rightarrow \equiv SiCH_3 \qquad\qquad (2.6)$$

The reactions described in 2.4-6 allow for achieving a complete surface methylation in flat atomic surfaces of crystalline silicon.[61] However, when the surface morphology is modified, for example in porous silicon, the efficiency of molecular substitution of hydrogenated silicon by methyl groups decreases to about 80%.[62] It is therefore expected that surface methylation applied to amorphous silicon surfaces results in a large but incomplete Si-H substitution.

Fig. 17 presents the ATR-FTIR spectrum of a methylated amorphous silicon layer. The grafted layer can be identified by the deformation modes of the methyl group at 1255 cm^{-1} for symmetric deformation and 1410 cm^{-1} for asymmetric deformation, and the stretching modes at 2900 cm^{-1} for symmetric stretching and 2960 cm^{-1} for asymmetric stretching.[60] Besides the surface methylation, residual contamination from the grafting reactants and oxides can be identified by the extra peaks in the ATR-FTIR spectrum. It is likely due to the fact that some cleaning steps had to be avoided due to possible corrosive effects for samples based on stainless steel substrates, such as rinsing in HCl for Mg(OH)$_2$ removal as suggested in previous works.[60]
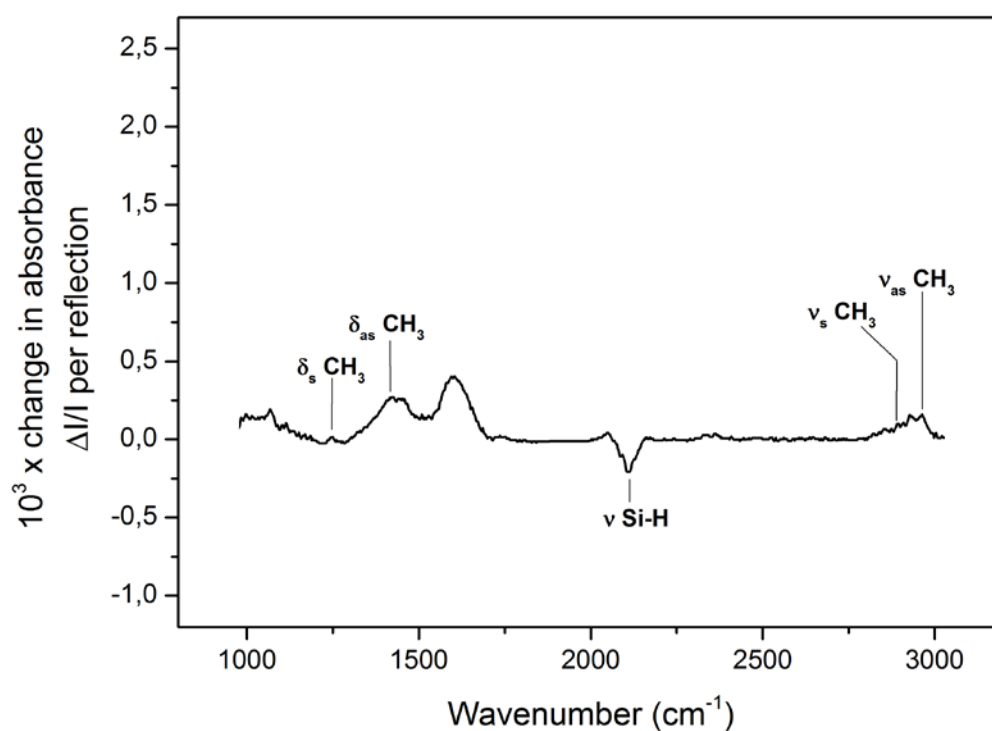
Fig. 17 – ATR-FTIR of methylated a-Si:H surface, referred to the hydrogenated surface in HF vapor.

Direct quantitative evidence of methylation was obtained by comparing the integrated values of the band intensities of the Si-H vibration modes centered at 2100 cm^{-1} before and after the grafting procedure. It was possible to determine that the surface methylation was responsible for a consumption of 55% of the hydrogenated sites. However, part of the Si-H consumption is maybe due to surface oxidation during the anodic process of grafting under trace impurities. Small trace of such oxidation, sometimes observed, is totally absent from the spectra plotted in Fig. 17, which does not exhibit any oxide-related feature in the 1000-1200 cm^{-1} range. All in all, it might be considered that the methylation efficiency is limited to a value of ~ 50%, larger than the grafting efficiency of longer molecule chains (see here after) but specifically lower than the figure reached on crystalline or porous silicon.

Electrochemical tests show that surface methylation has a negative impact on the electrochemical performance of the amorphous silicon layers deposited on stainless steel substrates. Fig. 18 shows that the grafting treatment increases the charge irreversibly consumed during the first electrochemical cycle. The comparison between capacity values obtained for the methylated a-Si:H electrode (black line) and for the pristine layers (gray line) shows that the lithiation capacity increases by 255 mAh g^{-1} and the irreversible capacity increases by 340 mAh g^{-1} for the grafted samples. The electrode methylation decreases the coulombic efficiency by about 5% and increases the irreversible charge by 18% as scaled to the reversible charge. Furthermore, the shape of the electrochemical cycling curve is modified for the methylated electrodes. As for a pristine layer, the electrolyte decomposition starts from about 1.3 V vs. Li/Li$^+$, however, for methylated surfaces an intensive reaction is observed from about 0.8 V vs. Li/Li$^+$; this extra reaction is no more discernible when the lithiation potential is reached.
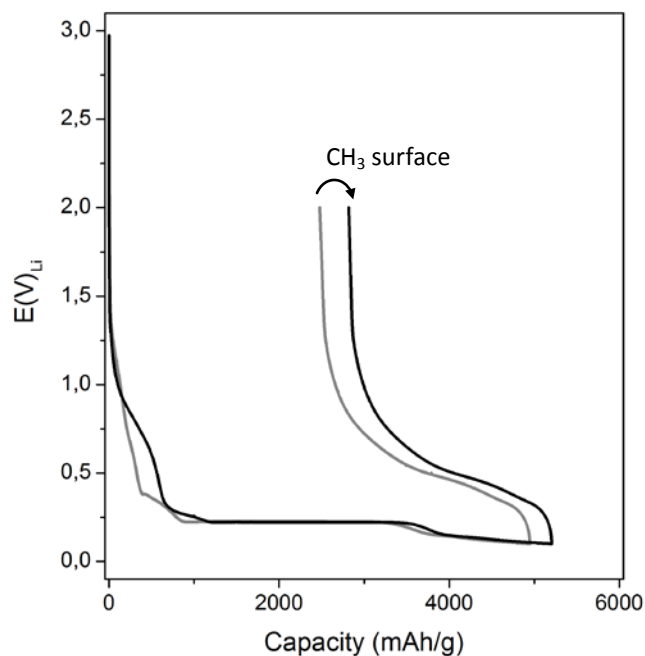
Fig. 18 – Electrochemical cycle of a-Si:H deposits on steel substrates. Methylated surface (black line) and pristine surface (gray line).

Even though surface methylation leads to a decreased electrochemical performance, when compared to the pristine case, the results indicate that the capacity values here obtained were close to the theoretical value expected for silicon. The effect of surface methylation was clearly related to the introduction of new chemical species into the electrode processes resulting in additional sources of side reactions and consequently increasing the amount of irreversible capacity. Our results are substantially different from the results observed elsewhere for silicon nanowires,[40] where the surface methylation was responsible for passivating the electrode, with undesirable consequences for the capacities values. In the case of silicon nanowires, the surface modification results in a reversible capacity of 538 mAh g^{-1} in the first electrochemical cycle. Taking into account that the surface area of electrodes based on nanowires increases the role played by the surface phenomena during cell operation, we can assume that part of the difference in the electrode performances is related to the reduced degree of surface methylation and the presence of contaminants observed in our experiments.

The superficial aspect of all the grafted electrodes studied in this work has been investigated by scanning electron microscopy (SEM). After completing one electrochemical cycle the samples were removed from the cell in an Argon filled glove-box, rinsed in fresh

anhydrous propylene carbonate, rinsed in anhydrous dimethyl carbonate, vacuum dried and stored in the glove-box. The SEM images were taken from samples directly brought from the glove-box in a protected atmosphere, being exposed to air only when installed in the microscope chamber. The SEM analysis does not show any important modification of the surface with the grafting procedure or with the electrochemical cycling. As shown in Fig. 19, methylated a-Si:H electrodes present a very smooth surface with the presence of some few structures. Some of them identified as probable traces of electrolyte rising, white spots of about 500 nm in the Fig. 19. Additionally, the presence of zones of higher contrast having 4 µm of diameter is observed. At the center of these zones an emerging structure (circular mark on the figure) possibly results from an inhomogeneous lithiated spot or concentrated SEI formation due the presence of surface contaminant.

Fig. 19 – SEM image of a methyled a-Si:H electrode after the first electrochemical cycle.

Decene grafted surface

Longer chains can be obtained by alternative (non electrochemical) techniques, which offers a better limitation of unwanted surface contamination, and the possibility of designing a thicker artificial SEI layer. Decene can be covalently bonded to silicon atoms with a high grafting density of about 6 molecules per nm^2, offering an important blocking property.[63] The application of such a molecular coating in lithium-ion batteries can allow for producing an artificial passivation layer that could reduce the need of electrolyte decomposition for the formation of a natural SEI. This strategy can increase the chemical stability of anode materials in contact with electrolytes, reducing the irreversible charge losses and resulting in more efficient electrochemical systems.

The grafting of decene is performed on oxide-free hydrogenated silicon surfaces by hydrosilylation, a radical-induced reaction which can be initiated either by free radical initiators, visible or ultraviolet light, or thermal activation.[32,64,65] The cleavage of the Si-H bond can be effectively photoinduced by 350 nm photons, a fact that makes UV light an attractive reaction initiator.[66] Grafting of decene on hydrogenated silicon starts with a photoinduced surface activation which is followed by the nucleophilic attack of an alkene. The reactions 2.7-9 describe the grafting mechanism, where the first reaction is the UV initiation followed by the propagation of the radical induced by the grafted molecule.

$$\equiv Si\text{-}H + h\nu \rightarrow \equiv Si^{\bullet} + H^{+} \tag{2.7}$$

$$\equiv Si^{\bullet} + CH_2{=}CH(CH_2)_7CH_3 \rightarrow \equiv Si{-}CH_2CH_2(CH_2)_7CH_3^{\bullet} \tag{2.8}$$

$$\equiv Si\text{-}H + \equiv Si{-}CH_2CH_2(CH_2)_7CH_3^{\bullet} \rightarrow \equiv Si{-}CH_2CH_2(CH_2)_7CH_3 + \equiv Si^{\bullet} + H^{+} \tag{2.9}$$
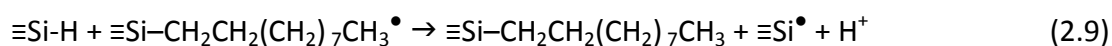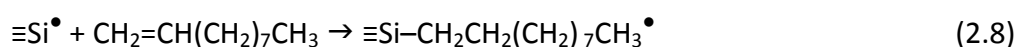
Such a reaction scheme is still debated and probably oversimplified, but the final surface product has been characterized.[32]

Qualitative and quantitative information about decene grafting on silicon surfaces can be obtained by ATR-FTIR measurements. The infrared signature of decene species grafted on silicon consists of the vibration modes of CH_2 scissoring at 1460 cm^{-1}, CH_2 symmetric stretching at 2852 cm^{-1}, CH_2 asymmetric stretching at 2925 cm^{-1}, CH_3 symmetric stretching at 2880 cm^{-1} and CH_3 asymmetric stretching at 2955 cm^{-1}. As shown in Fig. 20, all the characteristics vibration modes of decene were found in the the ATR-FTIR spectrum obtained for the grafting of decene on amorphous silicon. Moreover, a small signal of non-stoichiometric oxides is also observed at wavenumbers below 1075 cm^{-1}.
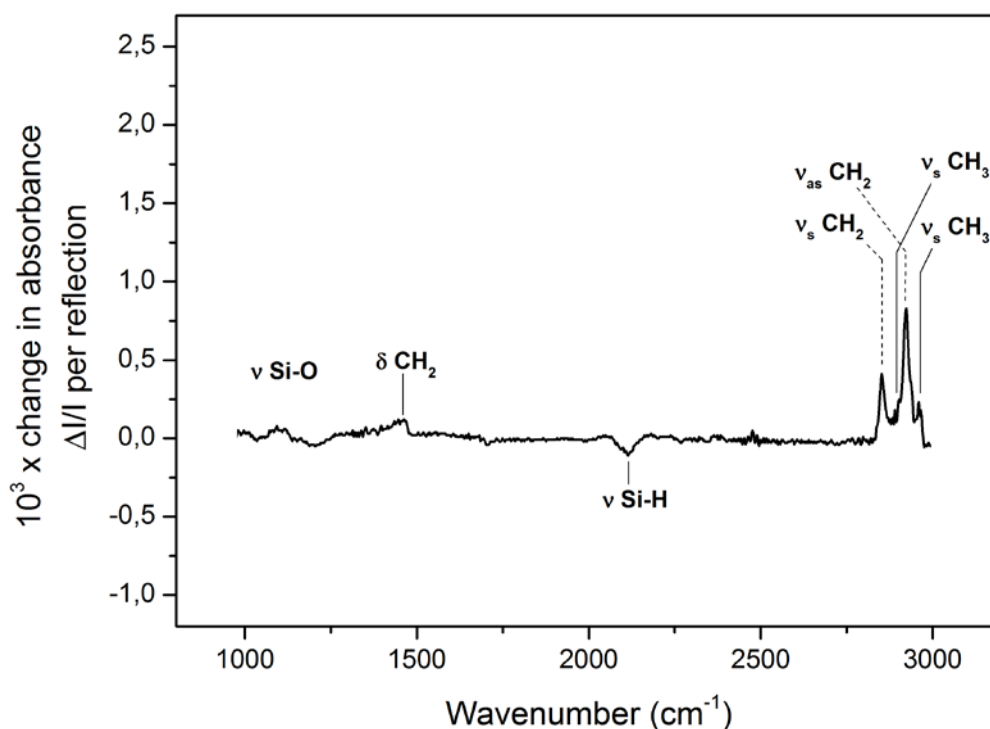
Fig. 20 – ATR-FTIR spectrum of amorphous silicon layer grafted with decene, referred to the hydrogenated surface in HF vapor.

The concentration of surface grafted species was determined from a truly quantitative study of the infrared signature of decene, where the CH vibration signals were fitted by using a model consisting of a linear baseline and Voigt functions as described in reference 70. The absorbance signal characteristic of the symmetric stretching vibration mode of CH_2, positioned at about 2850, was used to estimate the total surface density of CH_2 species present on the silicon surface. The results were compared to the calibration values obtained from the infrared cross section of the same CH_2 vibration mode in dodecane, giving origin to an equation which relates the infrared absorption signal of v_sCH_2 with its surface concentration on silicon. Assuming that each decene molecule is composed of nine CH_2 groups, one can estimate the decyl chain surface concentration. In the present work, the decene grafting on a-Si:H surfaces resulted in surface concentration of decyl chains of 2.9×10^{14} cm^{-2}, estimated from the analysis of the infrared spectrum shown on Fig. 20. This value is close to the one obtained for grafting in atomically flat Si(111) surfaces, estimated to 3.1×10^{14} cm^{-2}.[70]

Quantitative analyses, having the peak areas calculated for oxidized surfaces as a reference, leads to the conclusion that oxidation during decene grafting does not overcome 2% of the initial hydrogenated sites. Taking into account that 92% of the surface was efficiently hydrogenated by HF vapor, the total oxide content on the decene grafted surface does not exceed 10% of the surface.

Previous work estimated that the maximum coverage of Si(111) surfaces by the grafting of decene molecules is between 0.4 and 0.5 of the atomic sites (7.83×10^{14} cm^{-2}).[70,67,68] We can expect that this value is proportionally respected for the case of a-Si:H and assume that the difference verified between the values of grafting concentration in a-Si:H and in Si(111) indicates the relation between the surface treatments in these two different substrates. According to our estimation (based on the intensity of the 2850 cm^{-1} peak in the infrared spectrum)[70], the decyl surface concentration account to 3.2×10^{14} cm^{-2} on the a-Si:H grafted surface, i.e., ~40% of the atomic sites with respect to Si(111). When taking into account the small amount of oxide on the surface, this figure reveals the achievement of a dense molecular layer.

As shown in Fig. 21, the shape of the electrochemical cycling of a decene grafted electrode (black line) presents an unexpected feature when compared to a pristine electrode (gray line). The charge consumed for lithiation is much increased by parallel reactions that prevent the complete silicon lithiation. It is observed that for very high capacity values (> 5500 mAh g^{-1}) the electrochemical potential moved to a different electrochemical plateau, 30 mV lower than the lithiation plateau. The lithiation process was intentionally interrupted at 7840 mAh g^{-1} due to the abnormally large value of capacity reached by the system. The reversible charge value of 1480 mAh g^{-1} demonstrates that only a modest part of the charge was consumed for silicon lithiation. Besides the atypical performance of decene grafted electrodes, it seems to initially delay the electrolyte decomposition at about 1.3 V vs. Li/Li^{+} and decrease the capacity necessary for reaching the lithiation plateau.
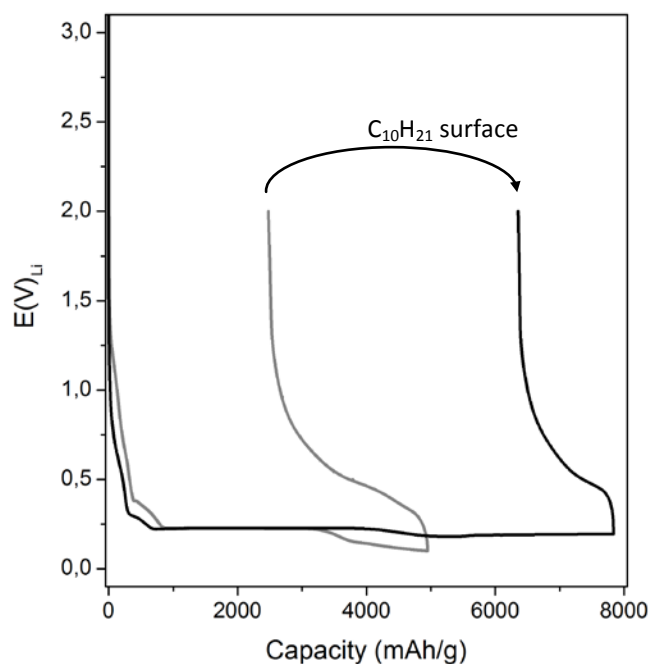
Fig. 21 – Electrochemical cycle of a-Si:H deposits on steel substrates. Decene surface (black line) and pristine surface (gray line).

The result of such odd charge capacity is revealed by the SEM images in the Fig. 22. Low magnification images (a and b) give the general aspect of the sample. It is possible to observe the presence of a ramified superficial structure of several micrometers. Traces of electrolyte from rinsing and drying procedures, which also result in beam sensitive structures, were previously observed in other samples. Electrolyte traces follow the direction of the solvent drying resulting in a peculiar geometry of marks different from the ramified structures observed for decene grafted electrodes. It dismisses the fact that the observed structures are simply traces of the electrolyte drying. Such structures cover most part of the sample and were found to be very sensitive to the electron beam of the microscope. Fig. 22 (c to e) show high magnification images at a fixed position over one of the observed structures. The sequence of images (c to e) was recorded in a short period of time and reveals the fast decomposition of the superficial structures when exposed to electron beam in the SEM. These structures are extremely similar to those formed during the grafting of high molecular weight modified PEG on crystalline silicon, as observed in reference 69. It indicates that decene grafted silicon electrodes can lead to centers of intense electrolyte reduction with subsequent polymerization giving origin for such structures. Since surface decyl layers appear very dense it can be inferred that the location at which the structures nucleate are associated to defects in the layer or oxidized spots.

Fig. 22 – SEM images of a decene grafted a-Si:H electrode after the first electrochemical cycle. Low magnification images (a, b) and high magnification images during different time intervals at a fixed position (c-e).

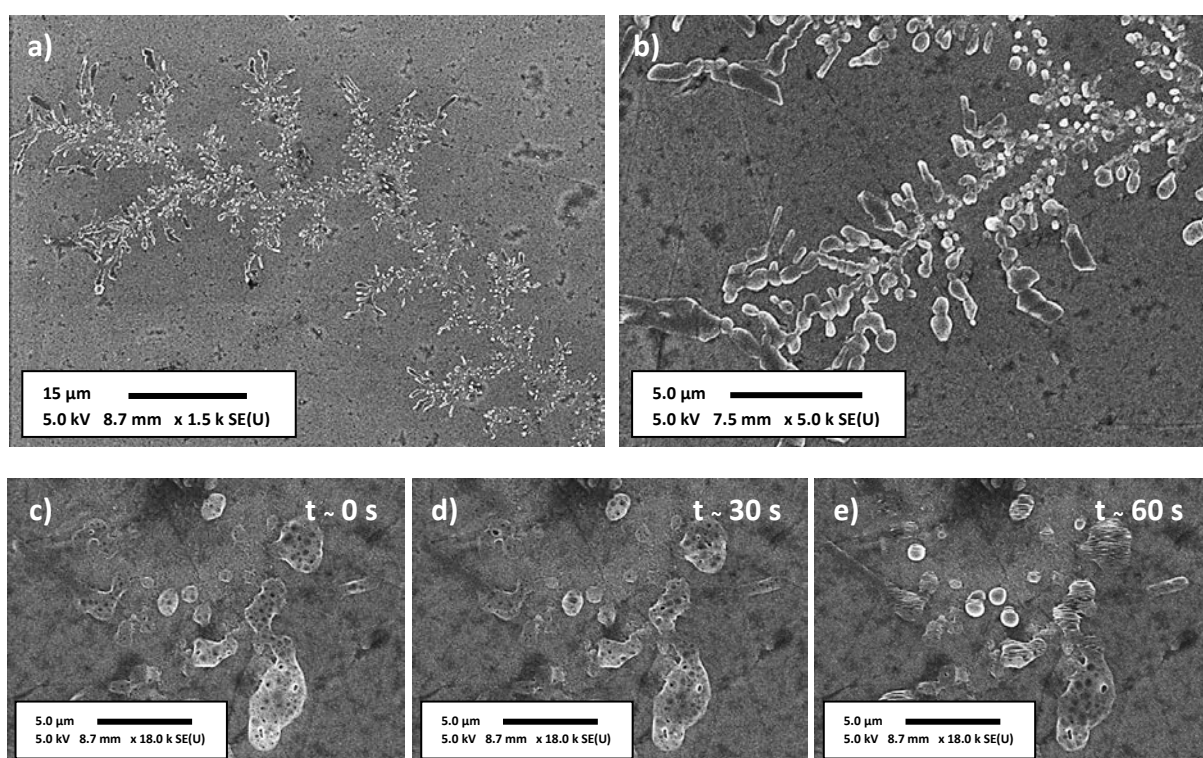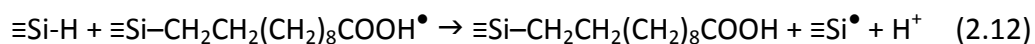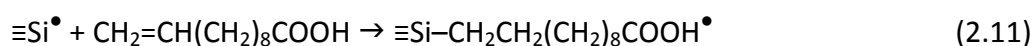Destructive effects of ex-situ analysis, such as SEM, demonstrate the importance of in situ measurements on the study of sensitive materials. The idea behind the in situ experiments of this work is not only to prevent the oxidation of lithiated materials but also to avoid changing the structure or inducing chemical evolution of less stable species. This concept will be further discussed in chapter 3.

Undecylenic acid grafted surface

Carboxyl-terminated alkyl monolayers represent an attractive surface functionalization for different application fields such as chemistry, biochemistry, sensor and microelectronics. Similarly to the previous mention for decene grafting, undecylenic acid layers are also obtained by radical-induced hydrosilylation initiated by different methods. The processes yield densely packed Si-C covalent bonded layers, offering good hydrocarbon chain surface coverage and chemically stable surfaces,[32,70] with exception for grafting under visible light which leads to low density grafted layers.[71] The improved stability of such molecular layers can be proved through the thermal stability of undecylenic acid layers grafted on Si(111) surfaces, which remain stable up to 150°C.[72]

Undecylenic acid grafting follows the same mechanism proposed for the grafting of decene. It is performed on oxide-free silicon surfaces obtained by hydrogenation followed by the hydrosilylation process, which involves first the cleavage of the Si-H bond and second the free radical addition of the grafting molecule.[32,64,65] The reactions 2.10 to 2.12 describe the UV initiation and further radical propagation leading to the grafting of undecylenic acid on silicon sites.

$$\equiv Si\text{-}H + h\nu \rightarrow \equiv Si^\bullet + H^+ \tag{2.10}$$

$$\equiv Si^\bullet + CH_2{=}CH(CH_2)_8COOH \rightarrow \equiv Si–CH_2CH_2(CH_2)_8COOH^\bullet \tag{2.11}$$

$$\equiv Si\text{-}H + \equiv Si–CH_2CH_2(CH_2)_8COOH^\bullet \rightarrow \equiv Si–CH_2CH_2(CH_2)_8COOH + \equiv Si^\bullet + H^+ \tag{2.12}$$

ATR-FTIR analyses confirm the presence of carboxydecyl chains grafted to the surface of amorphous silicon layer through reaction of the C=C double bond of the undecylenic acid. Fig. 23 shows the spectrum of an acid grafted a-Si:H layer on an ATR crystal. The grafted layer can be essentially identified by the C=O stretching mode at 1715 cm^{-1}, but also by the C-OH scissoring at 1415 cm^{-1}, CH$_2$ scissoring at 1465 cm^{-1}, CH$_2$ symmetric stretching at 2855 cm^{-1} and the CH$_2$ asymmetric stretching at 2925 cm^{-1}. The spectrum also reveals a

minor surface oxidation according to the stretching vibration of non-stoichiometric oxides at wavenumbers under 1075 cm^{-1}, estimated to amount of 2.6% of the hydrogenated sites resulting in a total oxidation of about 10% of the surface silicon atoms.

As for decyl layers, the measurement of the infrared peak intensity and the comparison to a liquid-phase calibration procedure, makes possible the evaluation of the concentration in the molecular layer.[70] The estimation of acid species concentration on the surface of silicon is based in the infrared signal correspondent to the C=O stretching vibration at 1715.6 cm^{-1}. The resulting values yield a surface concentration of acid molecules of 2.9 x 10^{14} cm^{-2} in a-Si:H, which appears larger than typical values obtained for Si(111) (2.7 x 10^{14} cm^{-2} from reference 70).

The difference between these two figures suggests that grafting probability is enhanced at the a-Si:H surface, due to the increased availability of surface Si-H bonds (associated with Si–H, Si–H$_2$ and Si–H$_3$ sites). Besides the uncertainty on the peak determination, the result here again point to the achievement of a dense acid-terminated molecular layer.
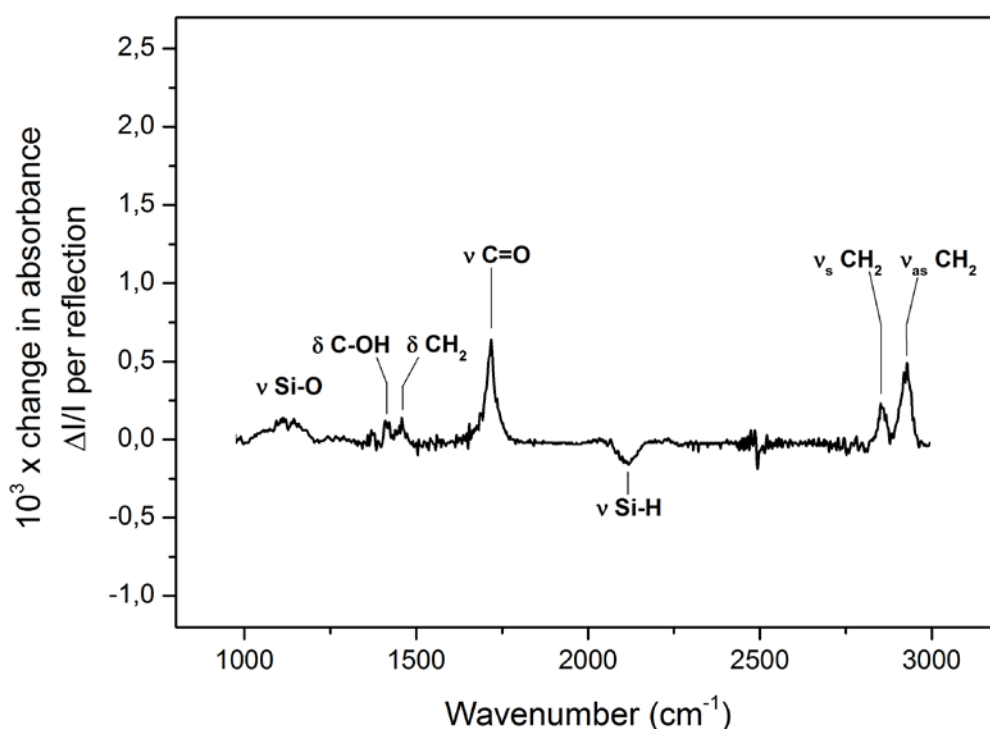
Fig. 23 – ATR-FTIR spectrum of amorphous silicon layer grafted with undecylenic acid, referred to the hydrogenated surface in HF vapor.

The effect of undecylenic acid grafting on amorphous silicon based electrodes was tested by electrochemical (GCPL) experiments in O-ring sealed cells, using 1M LiClO$_4$ in

propylene carbonate as electrolyte and lithium foil mounted in copper as counter-electrode. Fig. 24 shows the electrochemical cycle of an a-Si:H based electrode grafted with undecylenic acid (black line) and a pristine electrode (gray line). The change in the electrode performance due to the surface treatment is evident. The lithiation capacity is decreased by 960 mAh g^{-1} with a minor decrease in the delithiation capacity by 120 mAh g^{-1} and an important reduction in the irreversible capacity by about 840 mAh g^{-1}. It results in a 9% increase in the coulombic efficiency and 30% decrease of the irreversible capacity as a percentage of the reversible capacity.
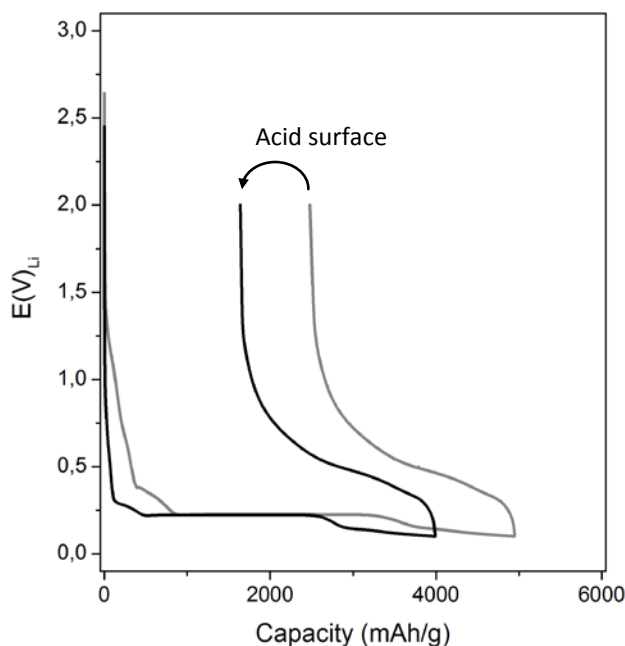
Fig. 24 – Electrochemical cycle of a-Si:H deposits on steel substrates. Undecylenic acid surface (black line) and pristine surface (gray line).

Fig. 24 additionally reveals the change in the shape of the electrochemical cycling resulting from the surface treatment. The zone related to the first electrolyte decomposition, from 1.3 V vs. Li/Li$^+$ till the lithiation potential, and the lithiation capacity are significantly decreased with the grafting. It suggests that the layer of undecylenic acid molecules effectively act as a passivating agent contributing to decrease the electrolyte decomposition on the electrode surface and the amount of charge irreversibly consumed for the formation of a spontaneous SEI.

The superficial aspect of undecylenic acid grafted electrodes has been observed by SEM. Fig. 25 shows the SEM images of the a-Si:H grafted electrode after the first electrochemical cycle. Unlike previous surface treatments, grafting with undecylenic acid results in a rich surface modification after electrochemical cycling. The main feature is the presence of a layer covering most of the surface, but intensely fractured by a network of defects with origin in the scratching marks left by the polishing procedure. A selected region

on Fig. 25 had its contrast intentionally increased for revealing the layer structure. All of these structures, with exception to the polishing marks, were not present in the surface before the electrochemical cycling. The origin of the layer is not clear, which could tentatively be associated to the SEI, may be cracked under drying. In spite of the low magnification of the SEM image, no contrast is discerned under optical microscope.
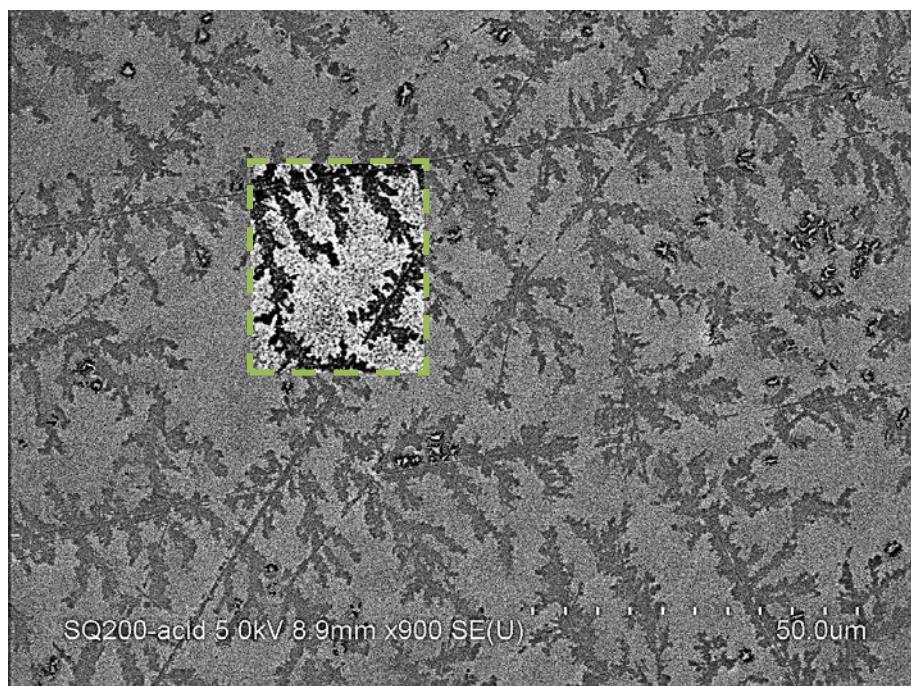
Fig. 25 – SEM image of undecylenic acid grafted a-Si:H electrode after the first electrochemical cycle. Inset region where the contrast was intentionally modified for revealing the layered structure observed.

Polyethylene glycol grafted surface

Polyethylene glycol (PEG) is a low-molecular-weight polyethylene oxide (PEO) with chain length up to about 150 repeating units. It is a crystalline, thermoplastic polymer also considered as an uncharged polyether.[73] PEG plays an important role in surface science for bioengineering applications. Ultrathin PEG coatings can be obtained by grafting of linear chains, representing an efficient barrier for blocking nonspecific protein absorption.[74] Grafting of dense PEG layers can typically reach thickness values on the range of 1.5 to 11.5 nm, grafting density up to ~2 chains per nm^2 and distance between grafting sites of 0.9 nm, for PEG of 5000 g mol^{-1} of molecular weight.[74]

Such barrier properties can be applied for lithium-ion systems, in order to establishing an artificial passivation layer for electrode materials. Therefore, PEG grafting on amorphous silicon layers was performed by UV photo-induced mechanism in a protected

atmosphere using concentrated poly(ethylene glycol) methyl ether with average mean molecular weight of 750 g mol^{-1}. UV irradiation is considered to be an excellent method for surface grafting of polymers due to its simplicity, cleanliness and efficient production of active species.[75] Grafting of PEG on silicon is based in the nucleophilic attack of Si-H surface species by the oxygen lone pair present in the $CH_3(OCH_2CH_2)_{16}OH$ alcohol end group and followed by loss of dihydrogen which results to an oxidative addition and formation of the $CH_3(OCH_2CH_2)_{16}O$-Si$\equiv$ link.[76] The reaction yielding to PEG grafting on silicon surfaces is summarized in Eq. 2.13. The complete experimental grafting procedure of PEG is detailed in the appendix A.

$$\equiv Si^{\bullet} + OH(CH_2CH_2O)_{16}CH_3 \rightarrow \equiv Si-O(CH_2CH_2O)_{16}CH_3 + H_2 \qquad (2.13)$$
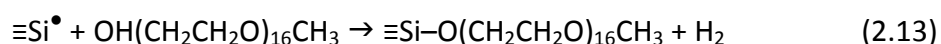
Amorphous silicon layers deposited on ATR crystals were grafted with PEG and analyzed by ATR-FTIR. Fig. 26 show the spectrum obtained for the grafted layer with the hydrogenated surface as reference. The spectrum clearly indicates the PEG grafting with some surface oxidation and consumption of Si-H surficial species. Notice that PEG absorption (C-O-C stretching mode) sizeably contributes to the large peak around 1100 cm^{-1} (overlapping Si-O-Si modes from silicon oxidation). PEG layer is identified by various CH_2 vibration modes, such as twisting modes at 1247 cm^{-1} and 1296 cm^{-1}, wagging at 1325 cm^{-1} and 1350 cm^{-1}, scissoring at 1460 cm^{-1}, and symmetric stretching at 2876 and asymmetric stretching vibrations at 2935-2940 cm^{-1}. Additionally, one can discern concentrations from the symmetric and asymmetric stretching modes of CH_3 groups at 2820 cm^{-1} and 2980 cm^{-1}, respectively. C-C and C-O vibration modes in the C-O-C structure are centered at about 1110 cm^{-1}, with shoulders extending from 1040 cm^{-1} until 1140 cm^{-1}. This wide range of vibration frequencies close to 1000 cm^{-1} makes the determination of stoichiometric SiO_2 at 1075 cm^{-1} difficult.
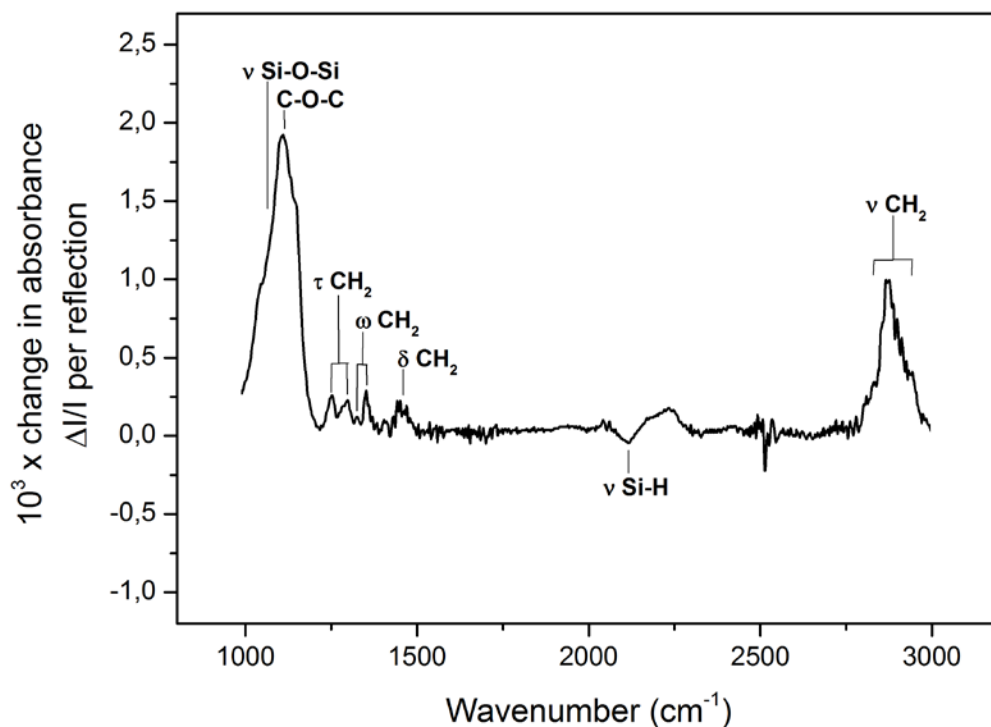
Fig. 26 – ATR-FTIR spectrum of amorphous silicon layer grafted with polyethylene glycol, referred to the hydrogenated surface in HF vapor.

For accessing the value of grafted PEG concentration on the silicon surface the intensity of the large band in the 2650-3050 cm^{-1} region is integrated. This value has been shown to be related to the amount of PEG molecules on silicon surface on the basis of a calibration procedure.[77] The intense superposition of infrared absorption bands makes the individual fitting of all the vibration modes located in this region difficult. However, it has been demonstrated that the integrated area of the whole band, with a careful baseline subtraction, results in an accurate estimation of the surface grafting concentration.[77] On this basis, the analysis of the infrared spectrum shown in Fig. 26 indicates a surface concentration of PEG chains of 1.5 x 10^{14} cm^{-2} in a-Si:H and representing a surface coverage of ~20% (referred to the Si atom density of a Si(111) surface).

Silicon based electrodes prepared from a-Si:H deposits on stainless steel substrates were electrochemically tested after the grafting. The performance of such electrodes was clearly improved by the surface treatment. Fig. 27 shows the first electrochemical cycle of a PEG grafted silicon based electrode and its comparison with a pristine electrode. The improvements reached with this treatment are the decrease of the lithiation capacity by 760 mAh g^{-1} and the increase of the delithiation capacity by 120 mAh g^{-1}. This leads to an increase of 12% in the coulombic efficiency and a decrease of 38% of the irreversible charge normalized to the reversible charge. The shape of the electrochemical cycles in Fig. 27 indicates the decrease of charge consumed during electrolyte decomposition at 1.3 V vs. Li/Li$^+$ until the lithiation plateau. Additionally, the lithiation capacity is significantly

reduced without loss in the delithiation capacity. This suggests that the part of the charge capacity irreversibly consumed in secondary reactions is decreased by the PEG layer without harming the silicon lithiation/delithiation process. Unusually, it is noticed that the delithiation capacity increased albeit modestly with the surface treatment.
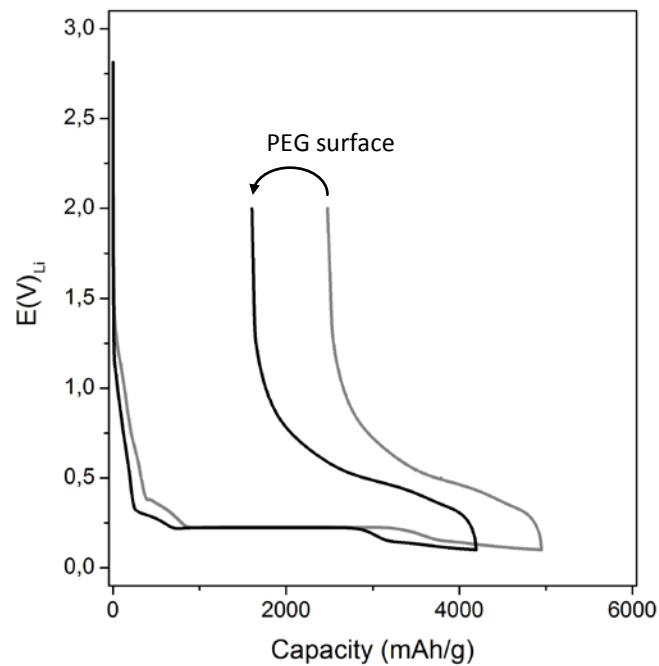
Fig. 27 – Electrochemical cycle of a-Si:H deposits on steel substrates. Polyethylene glycol surface (blackline) and pristine surface (gray line).

The superficial aspect of the grafted electrode after the first electrochemical cycle was analyzed by SEM and is presented in Fig. 28. It indicates that grafting and the electrochemical cycling do not modify the surface aspect of the electrode significantly. Therefore, the electrode exhibits a smooth surface after cycling where the presence of abrasion marks from the polishing procedure are the main identified features.
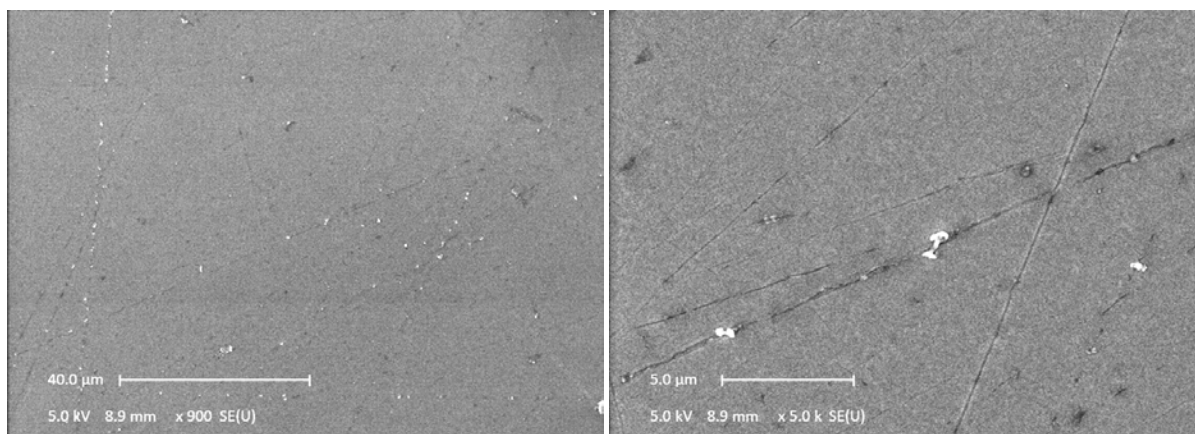
Fig. 28 – SEM images of a polyethylene glycol grafted a-Si:H electrode after the first electrochemical cycle.

Combined grafting of undecylenic acid and polyethylene glycol

The improved electrochemical performance obtained for polyethylene glycol grafted electrodes indicates a possible effect of the chain length on the electrochemical properties of amorphous silicon. Long chain length molecules can increase the effective thickness of the molecular layer, keeping a densely packed structure and enhancing the passivation properties.

This hypothesis was tested by attempting to create a grafted layer of even longer molecular chains while keeping a good coverage density. We chose the two species which improve the electrochemical performance in a single grafted layer: firstly grafting the surface with undecylenic acid and then coupling the PEG chain to the acid layer.

The chemical coupling of acid and PEG molecules is made by esterification. During the esterefication reaction the hydrogen present in the carboxylic termination of the undecylenic acid layer is replaced it by the PEG chain deprotonated at its alcohol termination. The reaction, schematically given below, is usually obtained by thermal activation in the presence of a catalyst. In this work p-toluenesulfonic acid was used as catalyst for the esterification reaction and all the experimental procedure is detailed in the appendix A.

$$\equiv Si-CH_2CH_2(CH_2)_8COOH + CH_3(OCH_2CH_2)_{16}OH$$

$$\downarrow \qquad\qquad\qquad (2.14)$$

$$\equiv Si-CH_2CH_2(CH_2)_8COO(CH_2CH_2O)_{16}CH_3 + H_2O$$
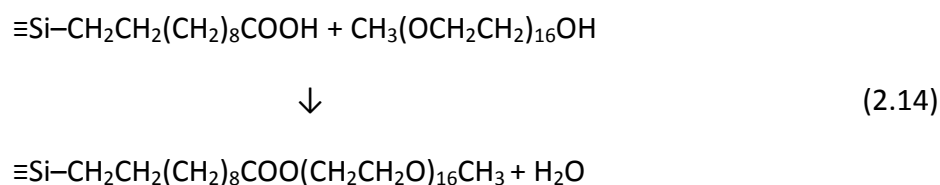
The esterification of undecylenic acid layer by PEG results in a combined FTIR signature originating from both species. Fig. 29 shows the ATR-FTIR spectra of the original surface grafted with undecylenic acid and that after esterification. Notice that the acid infrared spectrum was obtained with reference to a hydrogenated surface while the spectrum of the combined grafted surface was obtained using the acid spectrum as the reference. This latter choice allows for the identification of the incremental signals obtained by the addition of PEG molecules on the grafted acid layer. Hence, the presence of PEG is identified by the twisting vibration modes of CH_2 at 1247 cm^{-1} and 1296 cm^{-1}, wagging at 1325 cm^{-1} and 1350 cm^{-1}, scissoring at 1460 cm^{-1}, stretching vibrations from 2800 cm^{-1} to 3000 cm^{-1}, and the C-O-C structure at about 1110 cm^{-1}. The esterification reaction is evidenced by the modification of the C=O stretching mode, originally positioned at 1715 cm^{-1} for the undecylenic acid layer, shifted to 1735 cm^{-1} in the ester configuration which results in the "derivative" shape of the vCO band.

Infrared spectroscopy allows for quantifying the conversion rate of carboxylic groups to ester by comparing the spectra of undecylenic acid and esterified undecylenic acid. Employing the procedures described for the quantification of a pure PEG surface and pure acid surface already described here, one can estimate the acid surface concentration, the esterificated surface concentration and the esterification yield. The acid surface concentration after grafting is then estimated to 2.9 x 10^{14} cm^{-2} in a-Si:H and the PEG surface concentration after the combined grafting is estimated to 1.2 x 10^{14} cm^{-2}. It indicates an esterification rate of 41%. Therefore, the resulting a-Si:H surface exhibit a mixed coverage with acid chains and PEG esterified to undecylenic acid chains.
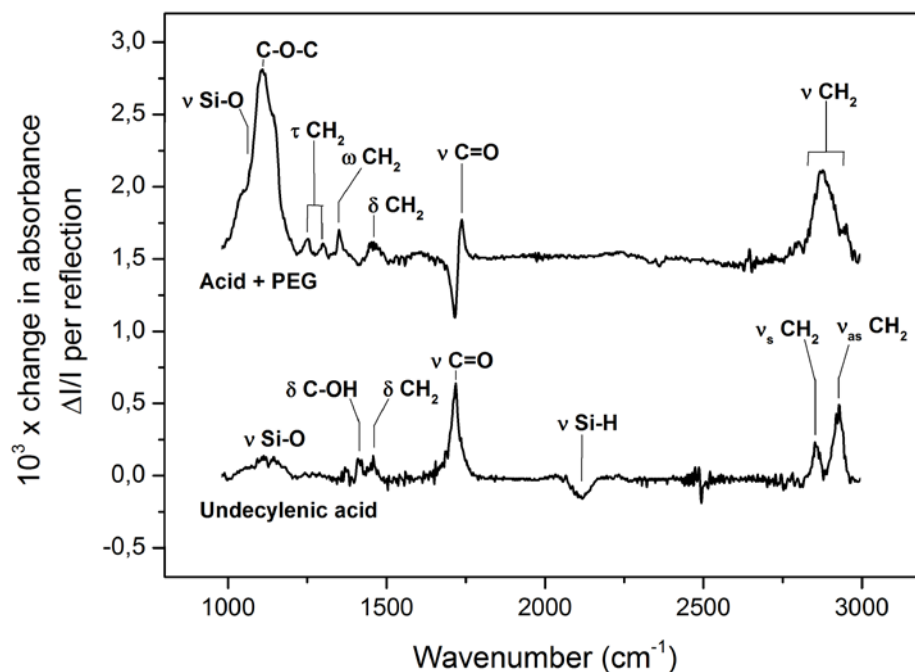
Fig. 29 – ATR-FTIR spectrum of amorphous silicon layer grafted with undecylenic acid esterified with polyethylene glycol, referred to the surface grafted with undecylenic acid.

Combined undecylenic acid and PEG grafting, obtained by undecylenic acid esterification, has been found to deteriorate the electrochemical performance of amorphous silicon electrodes when compared to the pristine case. As shown in Fig. 30, the combined grafting increases the lithiation capacity by 1180 mAh g^{-1} and decreases the delithiation capacity by 90 mAh g^{-1}, resulting in an increased irreversible capacity of 1270 mAh g^{-1}. Coulombic efficiency is also decreased by 11% and the irreversible capacity as percentage of the reversible capacity is increased by 57%. Electrochemical cycling results, exhibited on Fig. 30, indicate reduced electrolyte decomposition at elevated potentials (1.3 V vs Li/Li^{+}) similarly to what has been found for single grafted undecylenic acid or PEG electrodes. However, the increased values of lithiation capacity, exceeding the theoretical value of silicon lithiation, reveal the presence of electrochemical side reactions.

The combined grafting treatment appears disappointing in terms of electrochemical performance. Increasing the chain length of the grafted molecules does not necessarily improve this performance. In the present case, it appears that the combined effect of two molecules with different but individually favorable nature leads to an unfavorable configuration for the passivation properties of the final grafted layer in a lithium-ion system.
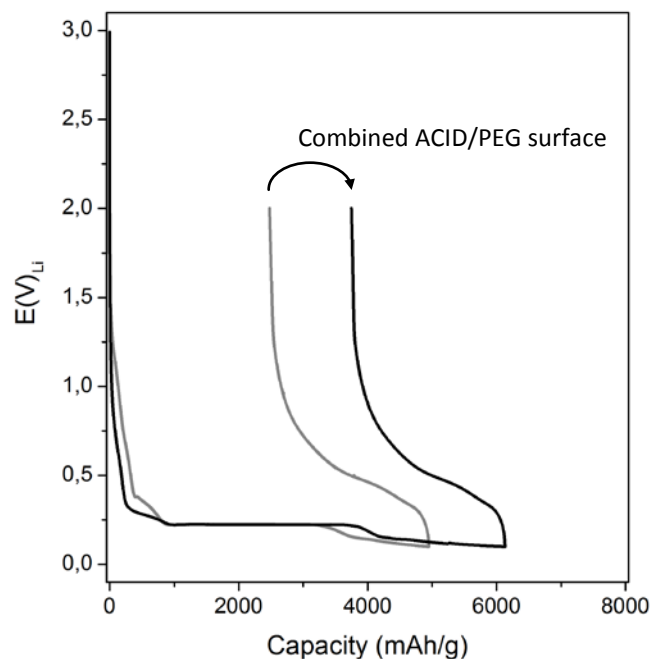
Fig. 30 – Electrochemical cycle of a-Si:H deposits on steel substrates.
Combined undecylenic acid and polyethylene glycol surface (black line) and pristine surface (gray line).

The doubly grafted electrodes were analyzed by SEM after the electrochemical cycling. The SEM images reveal smooth and homogeneous surfaces with no macroscopic defects or structures. Making use of high magnification images makes it possible to identify

large quantity of particles of about 400 nm of diameter, diffuse dark spots on the amorphous layer and traces of the polishing surface.
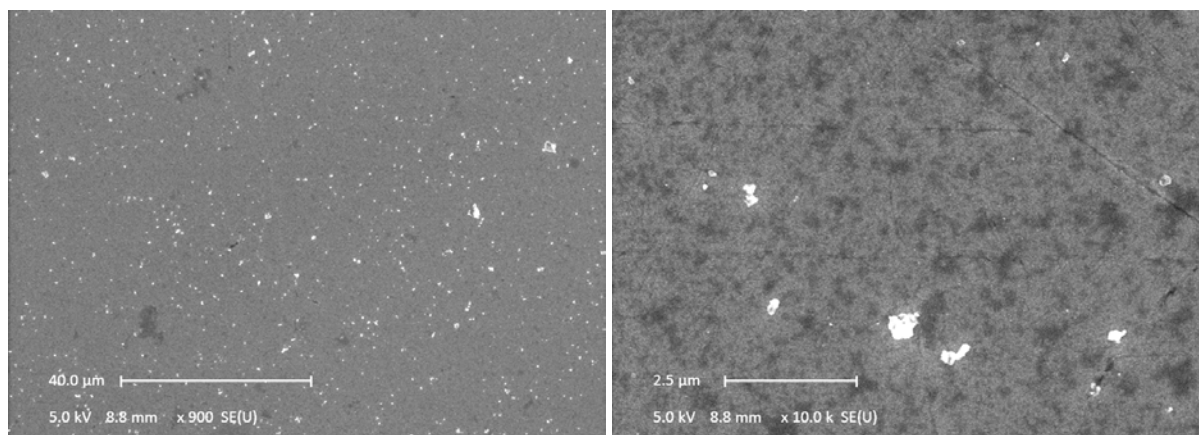
Fig. 31 – SEM images of a combined grafting of undecylenic acid and polyethylene glycol on a-Si:H electrode after the first electrochemical cycle.

2.4 – Discussion

The previous results demonstrate that depending on its chemical nature, a molecular layer grafted at the electrode surface may have a beneficial or detrimental effect on the electrode performance. Let us try to rationalize the results.

From a general view point, the grafting of molecules covalently linked on silicon surface can offer an efficient anchoring point for the species formed during electrolyte reductive decomposition. In general, the mechanisms of electrolyte reduction are based on the electrochemical decomposition of the solvent molecules with the formation of radial species during intermediary reaction steps.[114] These reaction decomposition products can react and attach to the electrode surface, or recombine and precipitate on the electrode surface, resulting in the SEI formation. In the same way the grafted molecular layer can react with the decomposition products, offering favorable or unfavorable sites for these reactions and thereby affecting the process of SEI formation. On general grounds, if the molecular layer offers favorable sites for interaction with the electrolyte decomposition products, it should contribute to the firm anchoring of the SEI layer to the electrode surface, owing to its covalent bonding to the electrode.

Analyzing the energy of dissociation of the different chemical bonds present in the grafted molecules could be a first attempt to evaluate the reactivity of the molecular layer

with the decomposition products and the possible hosting sites for products of electrolyte reduction.

In the point of view of dissociation energies and reaction kinetics there is an important difference between Si–H and Si–CH$_3$, as well as between Si–H and Si–C$_9$H$_{18}$CH$_3$, where weaker chemical bonding can offer the possibility of preferential dissociation during electrode processes, allowing a reactive surface site to be created and further reactions with electrolyte decomposition products to take place at this site. With respect to the above species, corresponding to the surface termination after hydrogenation, methyl or decyl grafting, the process of primary interest appears to be proton removal from the species present at the surface. Such a process is evident for the case of hydrogenated surface, for example, where the proton removal offers an access for in situ covalent bonding of SEI products with a modest energy barrier. It comes into play in the grafting reaction used on oxide-free silicon surface.

The role of additional species present on the hydrogenated surface can also be questioned. As a matter of fact, the HF vapor etching used for the removal of most of the surface native oxide, results in a surface rich in Si–H bonds but also with SiO$_x$ and Si–F traces. The strong bonding energy of Si–F likely makes them inefficient as promoters of surface activated sites. Then all the possible reactions between substrate and electrolyte reduction products are expected to take place at the hydrogenated sites. Si–H has a weak bond-dissociation energy and appears to be a good candidate for surface activation, as above mentioned. This can result in improved properties for the SEI layer.

The dissociation energy associated to proton removal from a surface Si-H species is about 3.5 eV, while from a surface Si–CH$_3$ group it is estimated to 4.3 eV. Similarly to Si–CH$_3$, the removal of a proton from an alkyl chain involves a dissociation energy ranging from 4.1 to 4.3 eV. Fig. 32 shows the molecular structure representation of different species present on the surface of silicon electrodes due to chemical etching (Si–H and Si–F) or obtained by grafting procedures. It also indicates the dissociation energies of the most probable affected bonds during electrode processes.
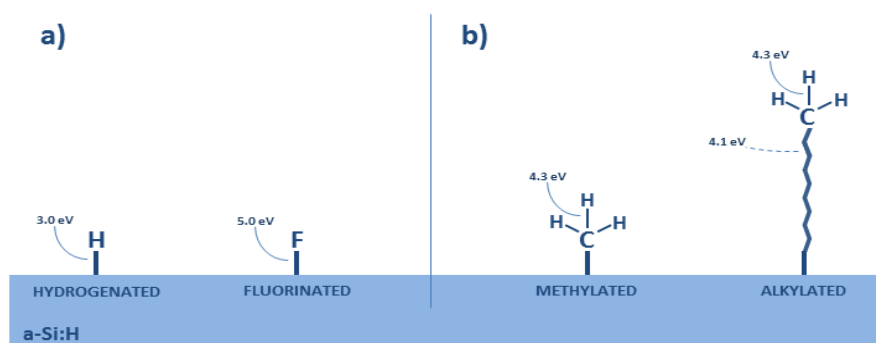

Fig. 32 – Dissociation energy of main species present on the surface of silicon electrodes due to chemical etching (a) and molecular grafting (b). Values of bond energies obtained from the references 42,78-83.

Therefore, methylated or alkylated surfaces offer for instance an increased energetic barrier for any chain activation when compared with Si-H. Consequently, SEI bonding to the silicon electrode is hardly achieved with the presence of these species grafted on the electrode surface. In these conditions, it additionally appears that using a long chain (decyl case) results in impeding lithium transfer to a-Si:H, with severe consequences to the electrode performance, as experimentally observed.

During electrochemical cycling, decene grafted electrodes exhibit a standard behavior until the end of the lithiation plateau, where the drop of potential seems to be associated to the onset of another electrochemical reaction with important amount of charge consumption: this reaction results in a blocking effect for the subsequent silicon delithiation. This suggests that the decene layer is stable until the potential values close to the lithiation potential, however once this limit is reached a kind of breakdown occurs yielding the accumulation of decomposition products.

The bond-dissociation energy approach is valid for explaining the relation between electrochemical performances and surface treatments with saturated hydrocarbons molecules. However, we believe that for molecules such as acid and PEG, the chemical reactivity also comes into play. Our results suggest that these molecules have improved affinity with decomposition products, providing a good anchoring to the SEI layer while maintaining a satisfactory ionic conduction.

Acid termination favors reactions with solvent products leading to a covalent link between SEI and electrode, where in the case of PEG such reactions take place with exoethylene units and probably not with the inert methyl termination. Both of these molecules result in improved electrochemical performances achieved by reducing the charge spent on side reactions, without affecting the reversible charge.

Undecylenic acid grafting represents an interesting surface treatment for amorphous silicon based electrodes for lithium-ion batteries. The densely packed superficial structure can offer an efficient passivation layer, apparently decreasing the need for intense SEI formation. The covalent attachment of the grafted molecules to the electrode material ensures a mechanical stability of the layer along volume changes in the electrode under electrochemical cycling. From a chemical point of view the carboxyl-terminated molecules offer a certain chemical similarity to carboxyl based typical SEI components, such as Li_2CO_3 or $ROCO_2Li$, accounting for the chemical affinity with electrolyte decomposition products. Additionally, the carboxylic acid termination on undecylenic acid molecules may represent an active site for chemical modifications during cycling, such as the bonding with SEI compounds which can covalently link the electrode material and the SEI layer.

On this basis, the disappointing performance of the combined acid/PEG grafting appears somewhat puzzling. It appears plausible that PEG coupling on the acid terminated

layer actually shields the remaining acid termination from the electrolyte decomposition products, by analogy with the antifouling behavior of the PEG layers.[77] It remains unclear why the long PEG molecules which likely adopt an entangled conformation on the top of the layer,[84] would exhibit a lower chemical affinity with the electrolyte decomposition products as compared to the case where they are directly grafted on the silicon surface.

2.5 – Conclusion

Various approaches were used to adjust the chemical composition of amorphous silicon thin films, in order to create a suitable artificial passivation layer on the silicon surface. Molecular grafting allows for the formation of densely packed structures with specific chemical properties affecting the electrode electrochemical performances. The choice of chemical species was based on the possible chemical reactivity (end group and chain skeleton), thickness of the molecular layer (chain length) and maximum achieved coverage at the silicon surface.

All the treated surfaces were controlled by FTIR measurements to verify their effectiveness and by electrochemical tests to determine the electrochemical impact brought by such modifications. It was shown that grafting can change the surface properties of the material, increasing its ability of effectively storing energy through electrochemical reactions. The origin of such behavior can straightforwardly be interpreted by the presence of an artificial passivation layer reducing the need of a natural SEI and the energetic cost of its formation, but also allowing for the covalent bonding between the electrode material and SEI components through the grafted molecular layer, thereby reducing irreversible charge losses. Fig. 33 summarizes the effect of surface modifications on the electrochemical performance of silicon electrodes based on the analyses of the irreversible capacities.

In the case of grafted surfaces, the best performances were brought by PEG and undecylenic acid. Both these species are not attached through the same kind of chemical bonding with the silicon surface. PEG is connected to silicon by a Si–O bond while undecylenic acid is linked by a Si–C bond. The similar positive results obtained for these two different species indicate that both chemistries are compatible with the development of efficient artificial passivation layers for lithium-ion electrodes. Moreover, it shows that the chain (terminal part of the chain and/or end group) bring the chemical features relevant for enhancing of the electrochemical performance.

Film effective thickness does not appear to play a key role in the beneficial effect of the grafted layer. A "long" decyl chain appears to exhibit a detrimental effect as compared

to a short methyl termination, but on the opposite a similarly long carboxydecyl chain exhibits superior performances.
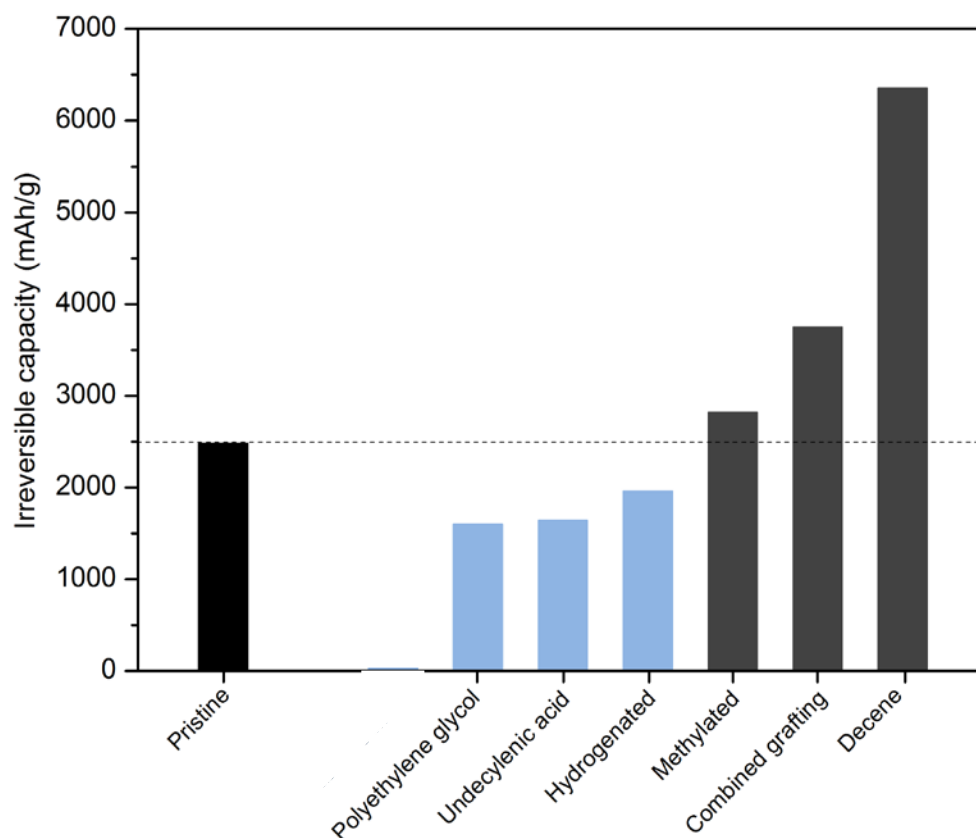
Fig. 33 – Irreversible capacities of silicon electrodes surface modified by molecular grafting.

Chemical trends among the various tested modifications can be, at least partially, rationalized in terms of chemical reactivity or affinity with the electrolyte decomposition products. It is however clear that a better level of understanding could be reached by making use of a direct chemical characterization of the chemical state of the interface and the SEI layer. Such is the purpose of the in situ infrared experiments presented in the next chapter.

Chapter 3 | In-situ FTIR

In situ FTIR allows for characterizing different electrode processes. It was used here for identifying the surface phenomena of SEI formation in amorphous silicon electrodes with different surface chemical treatments and in different electrolytes.

3 – IN SITU FTIR

3.1 – Introduction to in situ ATR-FTIR study

The mechanisms of SEI formation, lithium transport through SEI layer and bulk lithiation are rather complex phenomena and still a subject of controversial scientific discussions although they were extensively investigated by numerous techniques. In view of electrode materials, the thermodynamic instability of most of electrolytes leads to the formation of SEI layer on the electrode surface. SEI film composition and structure are sensitive to trace water, oxygen, and impurities. Such a susceptibility to ambient conditions highlights the importance of using characterization techniques that avoid the contact of electrode materials with non-protected conditions. However, even under protected or inert conditions, ex situ characterizations always require sample preparation procedures that represent an important change in the electrode environment, being partially responsible for the final results obtained, independently of the characterization technique. The most common example applied for the field of electrode materials is the rinsing and drying procedures, which can affect the final state and compositions of the sample surface significantly.

In the case of SEI layer, the chemical environment plays an important role not only for the layer formation but also on its maintenance. However, from the point of view of ex situ characterization techniques the perception of solid electrolyte interphase is usually related to a solid layer created from insoluble decomposition products of reactions between electrode and electrolyte. These measurement do not take into account the part played by the chemical environment on the structure of the SEI, especially the role of the solvent in the passive layer composition. On the other hand, in situ characterization techniques allow the analysis of the SEI formation to be performed without modifying its natural environment.

Infrared spectroscopy represents a powerful tool for the in situ study of electrochemical interfaces, in particular for the case of semiconductor-electrolyte interfaces by the help of multiple-internal-reflection geometries. FTIR has proved to be highly sensitive to electronic absorption, providing direct information on the semiconductor space-charge layer and on electronic states at the interface.[85,86,87] Polarization of the infrared light and time response analysis can give details about the orientation of interface species and kinetics, respectively. Moreover, the changes in electrolyte absorption and spectrum baseline can provide indirect information about species non-active to infrared, surface roughening, or porous formation.[88]

3.2 – FTIR as a tool for studying Li-ion electrodes

Common features of studies in the field of nanotechnology arise from problems connected with the physicochemical investigation of ultrathin films, which originate in general from their extremely small thickness. As previously mentioned infrared spectroscopy, and in particular Fourier transform spectroscopy, offers important advantages in the measurements of molecular composition and structure specially when combined with an attenuated total reflection (ATR) crystal.

ATR is based on the multiple-internal-reflection geometry, where the difference of refractive index between two media captures the incoming infrared beam in an ATR crystal with high refractive index. During its travel along the ATR crystal the infrared beam is reflected several times at the interface with the external medium. These internal reflections generate an evanescent wave that extends beyond the surface of the crystal into the external medium, collecting information about the species present within the probed depth and attenuating the final signal. More details about this principle can be obtained in appendix C.[89-91]

Semiconductors are generally used as materials for ATR crystals due to their high refractive index and sufficient transparency for most of the useful vibrational range. Additionally, moderate doping values generate sufficient electronic conductivity to make the use of semiconducting ATR crystals as electrode (or current collectors) possible for in situ electrochemical experiments, where the infrared beam may be sent toward the interface through the electrode itself.

In this work, an ATR crystal was coupled with a thin layer of the active material and employed as working electrode in an electrochemical cell, as described in Fig. 34. ATR crystals were obtained from germanium or silicon single crystals with parallel edges bevelled at 45°. The ATR crystals received on one side an electrical contact (Ohmic contact made of Au-Sb) and on the opposite side a 30 nm layer of active material a-Si:H. The infrared probe has its starting point based on the silicon surface, therefore, it is crucial that the contact between the electrode and electrolyte must be as intimate as possible. This need dismisses the use of a solid separator. Hence, a special cell was designed for the in situ FTIR study of amorphous silicon in the absence of a solid separator and using a lithium foil mounted in a copper current collector as counter-electrode. Galvanostatic cycling with potential limitation were performed using a potentiostat (AUTOLAB). The current density was kept at 24.8 μA cm^{-2}. It corresponds to a charge/discharge rate of C/1 (full theoretical charge or discharge in 1 hour). All the in situ cells were assembled and filled with the electrolyte in an Argon filled glove-box. The cells are made of an hermetic glass vessel, allowing for putting the cell at air contact. For experiments, the cell mounted in the IR chamber, was kept under constant nitrogen purge during the entire in situ experiment in order to avoid atmospheric disturbances in the infrared spectra.
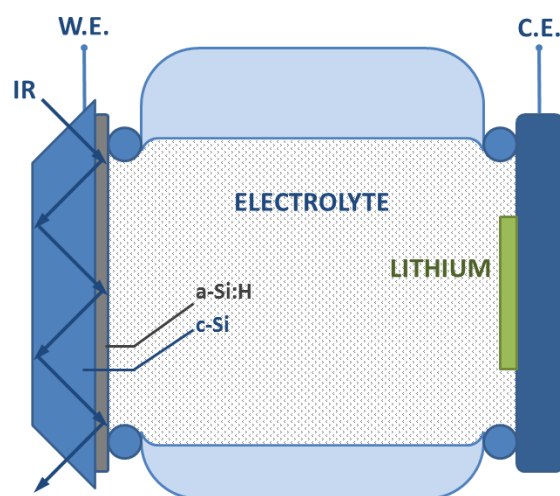
Fig. 34 – In situ ATR-FTIR cell.

In-situ FTIR experiments were performed by simultaneously cycling the electrochemical cell and acquiring FTIR spectra. The ATR-FTIR spectra were recorded using a Bomem MB100 FTIR spectrometer equipped with a liquid-nitrogen cooled HgCdTe (MCT) photovoltaic detector. Spectra were recorded with a p polarized infrared beam over the ~950-4000 cm^{-1} spectral range for silicon based ATR crystals and ~850-4000 cm^{-1} for germanium based ATR crystals (spectral range limited by the ATR crystal in the former case, and by the detector response in the latter one).

Due to the fact that all working electrodes for in situ experiments were based on ATR crystals made from materials that can also intercalate lithium ions, the limit between the active material (amorphous silicon layer) and the bulk material (crystalline silicon or germanium) was carefully investigated. ATR crystal lithiation was found to be practically limited to the a-Si:H deposit by choosing a relatively high limiting potential for lithiation. For lithiation potentials limited at 0.125 V vs. Li/Li$^+$, the prism was shown to be intact after at least 20 cycles. However, if the lithiation limit is lower than 0.125 V vs. Li/Li$^+$, the crystal can be damaged during cycling more and more severely when the potential limit is set lower and lower. Lowering the lithiation values demonstrated to increase the probability and the damages in the ATR crystals. Fig. 35 shows the final superficial aspect of an ATR crystal containing an amorphous silicon layer on the surface, electrochemically cycled for 20 cycles between 2 V vs. Li/Li$^+$ and 0.01 V vs. Li/Li$^+$. The images show the surface in contact with the electrolyte, where in a macroscopic view the identification of the cycled zone is possible (Fig. 35a) and in the SEM images (Fig. 35b) superficial cracks are easily revealed.

Fig. 35 – Macroscopic (a) SEM (b) images of an electrochemically ATR based electrode cycled 20 times under deep lithiation (E_{LIM} = 10 mV vs. Li/Li$^+$).
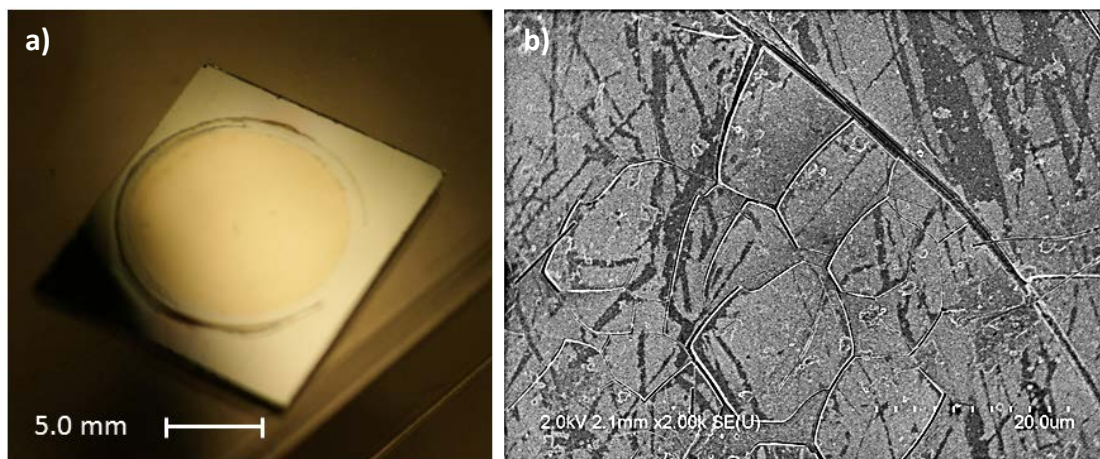
In our experiments, the electrochemical potential of cells based on silicon ATR crystals sharply decreases when the system reaches the theoretical capacity value of the amorphous silicon layer, with an increment in capacity due to charge consumed for SEI formation. This important electrochemical response demonstrates that the amorphous silicon lithiation is slightly easier than the crystalline silicon lithiation and can conveniently be time separated. Therefore, one can also prevent the crystal lithiation by stopping the electrochemical lithiation at the exact moment when the amorphous silicon is completely lithiated.

Silicon ATR crystals were shown to be suitable for electrochemical experiments but in the point of view of infrared light, the use of germanium based ATR crystal can offer better transmittance values in a wider spectral range. However, in electrochemical cells based on germanium crystals, the change in the electrochemical potential when approaching the full amorphous silicon lithiation is not noticeable as it was for crystalline silicon. The amorphous silicon lithiation plateau is prolonged till capacity values largely exceeding the theoretical value calculated for the deposited layer. The excess of lithiation capacity is due to the lithiation of the ATR crystal leading to its mechanical failure.

The absence of an electrochemical evidence for the lithiation limit of layers deposited on germanium points out the difference between the lithiation of crystalline silicon, crystalline germanium and amorphous silicon. Lithium atoms, coming from the lithiation of the amorphous silicon deposit, experience a change in the energetic landscape when diffusing into crystalline silicon, resulting in the decrease of cell electrochemical potential. However, even if a similar behavior might be expected for the case of amorphous silicon deposited on germanium, the difference between the energy states of these two materials do not lead to a perceptible change in the cell potential during lithiation.

In the point of view of the electrode processes, the experimental in situ setup allows for probing all the electrolyte modifications in the range of the evanescent infrared wave. In a first approach, the amorphous silicon based electrode can be described as a reversible or Nernstian electrode, because quasi-equilibrium thermodynamic relationships are obeyed at the electrode surface. Here, the surface concentrations of species involved in the Faradaic process are related to the electrode potential by a Nernst-type equation. Therefore, mass transfer plays an important role in the electrochemical dynamics of such a system and will be responsible for defining the formation of a Nernst diffusion layer.[92] As illustrated by Fig. 36, the formation of a diffusion layer in the vicinity of the electrode has direct effects on the in situ measured FTIR.
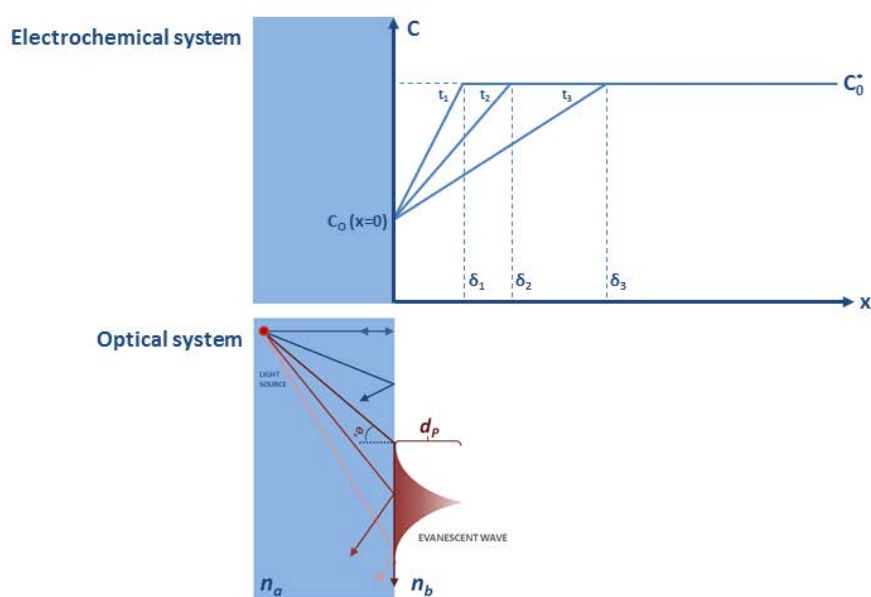
Fig. 36 – Illustration of Nernst diffusion layer formation and its relation with the in situ FTIR measurements. Notice that typical infrared probing depth (d_p) is much shorter than typical diffusion layer thickness (δ_i). So that the IR beam essentially probes an electrolyte with a concentration C_0 (x=0).

In parallel to the reversible exchanges in lithium species, the reversible bulk lithiation also contributes to the change in the concentration or nature of the solvent species present in the diffuse layer. Solvent molecules trapped in lithium solvation shells present in this layer are turned into free solvent species by the lithium consumption during bulk lithiation reaction, and regenerated by the bulk delithiation.

Most of the in situ characterizations presented in this chapter were also tentatively compared to ex situ measurements, which means that after the in situ experiments the samples were also ex situ analyzed. However, such measurements make necessary the use of rinsing and drying procedures after the electrochemical cycle, where the presence of trace electrolyte components can result in strong infrared signals inducing high incertitude in

the results. The results are not presented here, because they are considered as not conclusive. The FTIR signals were dominated by the electrolyte bands much more intense than those obtained using in situ measurements and they exhibited low reproducibility.

3.3 – In situ ATR-FTIR characterization

FTIR spectroscopy detects functional groups at distinct frequencies. The detection sensitivity, intrinsically associated to the dynamic dipole moment of the probed species, is enhanced in the ATR mode. In the case of in situ studies of Li-ion batteries, a great variety of infrared signals are expected. Most of the species in contact with the in situ working electrode in the experimental cell can give rise to an infrared signal. However, most of these signals are only part of a background absorption associated with the cell transmittance and do not give any information about the processes present in the system. This background absorption is cancelled by referring the measured signal to a spectrum recorded in a reference state. For this purpose, a FTIR spectrum was recorded prior to starting the lithiation/delithiation cycles on every freshly assembled and filled cell and it was used as the reference spectrum for the entire set of spectra obtained during the following electrochemical cycles. Using this reference spectrum, the results are displayed in terms of absorbance computed using the natural logarithm and scaled to one internal reflection. This data treatment procedure is particularly relevant since it highlights all the spectral signature of modifications occurred in the system during electrochemical cycling.

All the in situ FTIR spectra present in this chapter were acquired during continuous electrochemical cycling of the cells with a rate of C/1 and limited by the lithiation and delithiation potentials of 0.125 and 2 V vs. Li/Li$^+$, respectively. Infrared signal was recorded without interrupting the electrochemical cycling. It was verified that continuous electrochemical cycling allows optimum reproducibility of the results and avoids charge (or potential) relaxation observed when the electrochemical cycle is stopped. Each FTIR spectrum is the result of an accumulation of 100 spectra obtained during a period of 2 min, followed by a 1 min pause in the infrared acquisition. A typical recording procedure results in a new spectrum acquisition every 3 min and a capacity resolution of 3.2 mC or 180 mAh g^{-1} for a cell based on an amorphous silicon layer of 30 nm. The electrochemical signal obtained during cycling with simultaneous in situ FTIR signal acquisition is displayed in Fig. 37. This signal shows similar features to the electrochemical cycles performed using a standard electrochemical cell (presented in chapter 1 and 2), however, here the capacity values are different from those previously measured for similar surface preparations due to the higher potential limit for lithiation chosen for the in situ measurements.
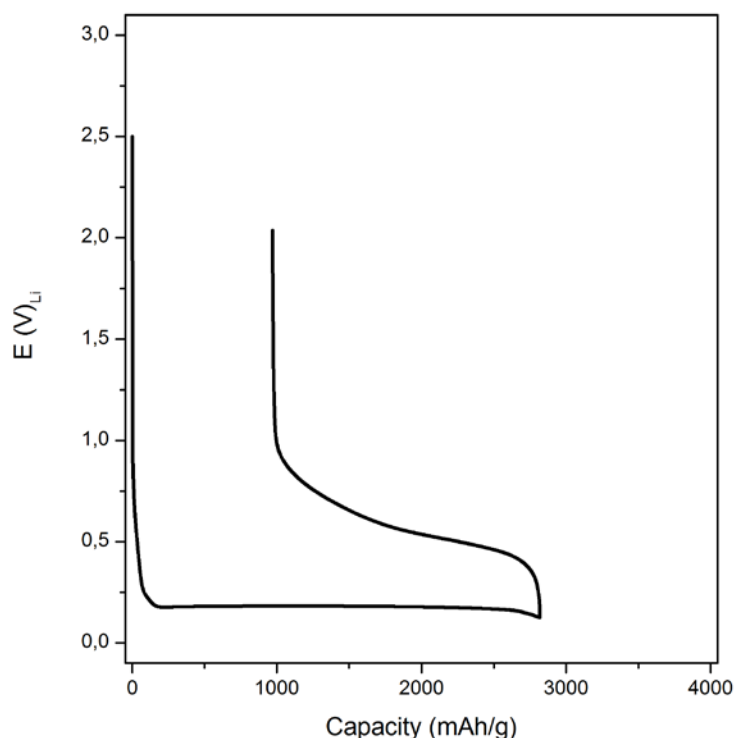
As shown in Fig. 37, the amorphous silicon lithiation exhibits a very flat plateau at about 0.180 V vs. Li/Li$^+$. The electrochemical cycling in this in situ cell presents capacity values substantially lower than the theoretical ones. This is expected due to the high potential limit for lithiation (0.125 V vs. Li/Li$^+$) used during the cycles. As previously mentioned, this high limit of lithiation helps for preventing the lithiation of the ATR crystal avoiding its subsequent cracking.

The high sensitivity of the ATR-FTIR technique enables to detect various features during electrochemical cycling. All the information collected along in situ FTIR experiments are now presented according to the different topics relevant for a practical comprehension of the system.

SEI formation

Most of the spectral information concerning the formation of the solid electrolyte interphase is identified in the so called fingerprint region in FTIR, typically from 1100 cm^{-1} to

1700 cm^{-1} in our case. It is important to take into account that all the infrared spectra are referred to the state corresponding to the amorphous silicon layer on the ATR crystal in the electrochemical cell, at open circuit potential previous to any current flow. In this way, the presence of new chemical species or the increase in concentration of the existing ones can be identified by a positive signal at a specific wavenumber value corresponding to one of its vibration modes. Similarly, the loss or reduction in concentration of any chemical species will result in a negative band in the spectrum. The intensity of the absorbance signal is proportional to the quantity of chemical species probed by the infrared beam, according to an absorption coefficient associated to the amplitude of the characteristic electric moment of the vibrator.[93]

In situ FTIR analysis of the SEI formation clearly exemplifies the effect of chemical modifications on the final spectrum. The growth of the SEI layer modifies the chemical composition in the vicinity of the electrode creating a number of new chemical species responsible for the rising of positive peaks in the FTIR spectra. However, SEI formation also causes the electrolyte displacement away from the amorphous silicon surface resulting in the loss of the infrared signal correspondent to the electrolyte spectrum. The fact that different phenomena occurring in the electrochemical cell have opposite effects on the final infrared signal make the interpretation of FTIR results a complex procedure.

Electrolyte composition plays an important role in the feature of the FTIR results. Since the electrolyte is the departure point for the SEI formation, a complete identification of its infrared signature is essential for understanding the in situ FTIR results. The FTIR spectrum of the 1M LiClO$_4$ in PC electrolyte was analyzed on the literature basis[94,95] and the main vibration modes are listed in Table 2.

Table 2 – Band assignments of 1M LiClO$_4$ in PC in the fingerprint region. Modes are labeled according to usual convention: ν stands for stretching modes, δ for deformation modes, τ for twisting modes, ω for wagging modes and ρ for rocking modes.

Functional groups in PC	Mode	Vibration (cm^{-1})
C=O	ν	1784
C-O-C	ν$_{as}$	1119, 1176
	ν$_{as}$ solvated	1134, 1209
CH$_2$	δ	1558
CH$_3$	δ	1450
	τ	1485
OCH$_2$	ω	1389
	ω solvated	1408
PC ring	ρ	1148
	ω	1338
	ν	1354
	ν solvated	1362
ClO$_4^-$	ν	1097

Some of the functional groups detailed in Table 2 are sensitive to the presence of lithium ions. These ions have impact on the vibration modes of different functional groups in propylene carbonate. PC molecules solvating Li^+ ions have vibration bands shifted from 1354 cm^{-1} to 1362 cm^{-1} for PC ring stretching and 1389 cm^{-1} to 1408 cm^{-1} for OCH_2 wagging. For C-O-C asymmetric stretching, the vibration mode at 1119 cm^{-1} shifts to 1184 cm^{-1} while the one at and 1176 cm^{-1} shifts to 1209 cm^{-1}. Additionally, the perchlorate anion is identified by its stretching vibration mode at 1097 cm^{-1}.

Fig. 38 shows the FTIR spectra obtained in situ for an amorphous silicon layer with a hydrogenated surface at the end of different electrochemical cycles at delithiated state, except for the very light gray line, which shows the first spectrum recorded during the beginning of the first lithiation. The spectrum of the electrolyte with the assignment of the most significant vibration bands is shown at the bottom of the frame for stressing the correlation with the in situ results. The electrolyte spectrum was computed accordingly to the same absorbance scale as the in situ results (this spectrum is referred to a spectrum recorded in the absence of electrolyte in the cell), but it is actually drawn using an attenuation factor of 50. The sequence of spectra demonstrates the evolution of the electrode surface state during the first ten cycles.
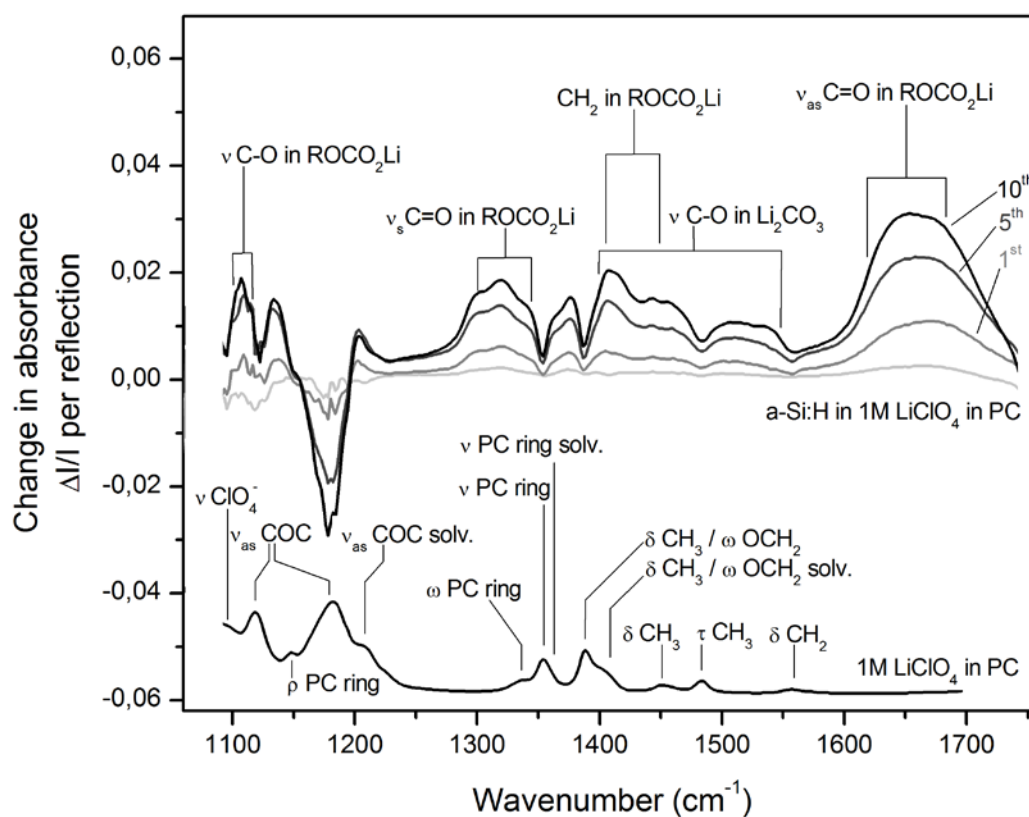

Fig. 38 – ATR-FTIR spectra obtained in situ cell after 1, 5 and 10 cycles (top) and the spectrum of the employed electrolyte.

In general, it was noticed that in situ spectra of amorphous silicon electrodes do not show very sharp absorption peaks. It illustrates the fact that the SEI is not rich of a particular component but is composed of a distribution of different species with similar chemical composition and that in situ FTIR technique is able to identify such a diversity. Positive-going bands in Fig. 38 clearly demonstrates the formation of new chemical species along electrochemical cycling. As previously mentioned in chapter one, propylene carbonate is thermodynamically unstable under electrochemical cycling conditions being decomposed mainly in $ROCO_2Li$ and Li_2CO_3, whose contributions can be identified in the in situ spectra (see labels in Fig. 38).

Large contributions in the in situ spectra can be related to electrolyte signals resulting from the change in the solvent/solvated ratio of concentrations and negative going bands. It is known that when lithium ions are solvated by nonaqueous organic solvents, the solvents affect the reduction potential and the subsequent decomposition reactions.[94] In the case of electrochemical experiments in PC based electrodes, besides the contribution due to the electrolyte displacement by the SEI layer above mentioned, a part of the negative-going bands could be related to the change in the molecular environment around PC molecules caused by the lithium ion solvation of PC. This phenomenon is revealed by the simultaneous formation of a paired signal of negative-going bands indicating the loss of free solvent molecules and positive-going bands related to the formation solvated ion molecules. Some of the latter being clearly distinct from SEI products. Fig. 38 indicates the presence of at least two well defined paired signals created by the change in the vibration modes of PC ring stretching from 1354 cm^{-1} to 1362 cm^{-1} and $O-CH_2$ wagging from 1389 cm^{-1} to 1408 cm^{-1}, both caused by the lithium ion solvation. These signals revealed to be relatively intense during all the electrochemical cycle, including at the end of the delithiation process, suggesting not only the presence of solvated ions in the SEI layer but also an increase of its concentration along the cycling life.

The concentration of propylene carbonate solvated to lithium ions is then dependent on the charge exchanged during electrochemical cycling. The fluctuations in the concentration of solvated species can be explained by diverse reactions occurring during electrochemical cycling, including the reversible reaction described in Eq. 3.1.[94]

$$Li^+(PC)_4 \leftrightarrow Li^+(PC)_3 + PC \qquad (3.1)$$

The electrode polarization attracts the lithium ions to the interface between electrolyte and electrode where different reactions affect the lithium concentration and modify the balance described in Eq. 3.1. At the same time as lithium concentration increases

due to electrode polarization, lithium ions enter the silicon electrode and some of them are trapped in the formation of the SEI layer. Therefore, polarization tends to favor solvation, while silicon lithiation and SEI formation favor the presence of free solvent molecules.

Even if at this stage the distinction between solvated PC and SEI products is not completely clear, it was verified that during lithiation the solvent signal decreases at the same time as the signal of solvated species increases. This result indicates the increase in lithium concentration in the probed region. Once the system is under delithiation, the original amount of solvent and solvated species is gradually regained and the final FTIR signal is partially reestablished. Fig. 39 shows the in situ FTIR spectra obtained during the first lithiation and delithiation processes for and a-Si:H based electrode in 1M $LiClO_4$ in PC.
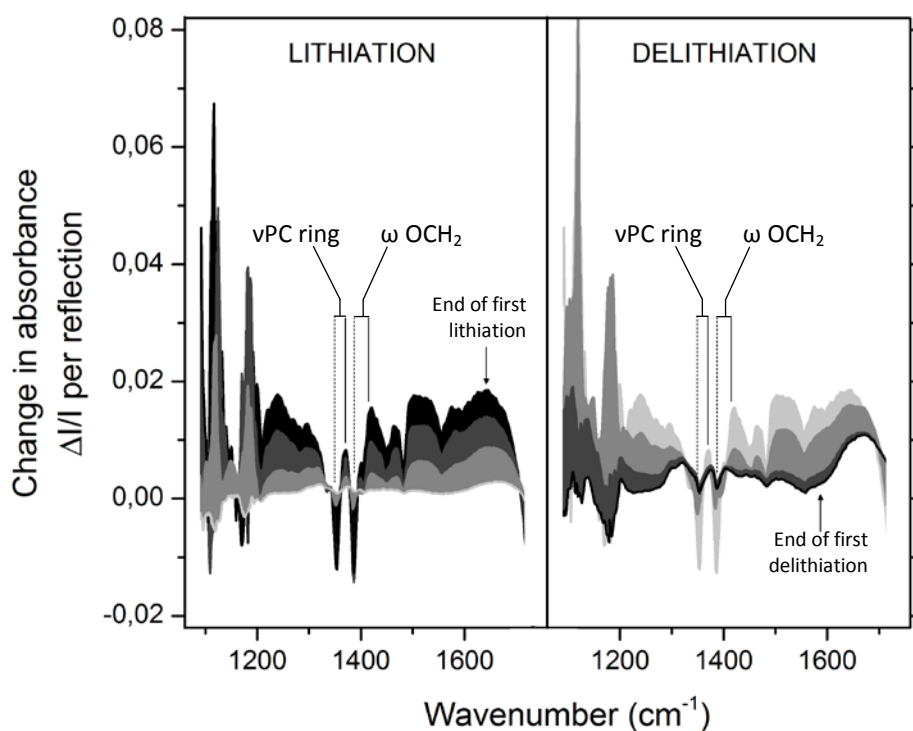
Fig. 39 – ATR-FTIR spectra of in situ cell at different stages during the first lithiation cycle of hydrogenated amorphous silicon.

The usual model of Nernst diffusion layer described for reversible electrodes assumes a mass-transfer-controlled reaction, as described in the introduction of this chapter. However, based on the in situ measurement and the described increase of lithium ions on the electrode surface during electrochemical cycling, it appears that mass transfer in the electrolyte is not the critical step in the studied system. The observed relationship between the applied electric field (electrode potential) and the amount of solvated species points to the important effect of lithium ion accumulation close to the amorphous silicon electrode.

We believe that the rate of silicon lithiation is the step controlling reaction, increasing the concentration of solvated species at the electrode surface. Therefore, the electrochemical system is under lithiation-rate (kinetic) control than under mass-transfer-control, as illustrated by Fig. 40.

Additionally, the presence of vibration bands related to solvated molecules are identified in the Fig. 39 even at the delithiated state after electrochemical cycle, demonstrating that the SEI formation include the trapping of solvated species and contribute for the high concentration of lithium species observed in the electrode vicinity.
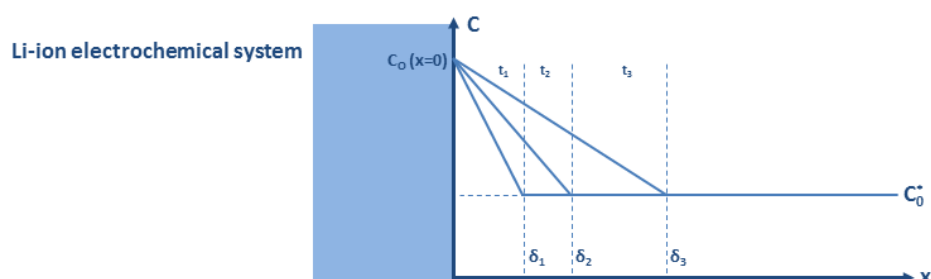
Fig. 40 – Illustration of the lithium concentration layer in amorphous silicon based electrodes.

The change in lithium ions concentration can affect the refraction index of the electrolyte. This is the principle behind holographic interferometry experiments, used for measuring the concentration profile of lithium-ion electrolytes during electrochemical cycles.[96,97] Therefore, one could wonder whether the reversible infrared signal measured by in situ experiments is actually the result of the modification of the refractive index in the electrode vicinity caused by the change in lithium concentration and its effect on the depth of penetration of the evanescent infrared wave. According to reference 96, the change in the refractive index of PC is of 3×10^{-3} M^{-1}. Based on this value we calculate that even with an overestimated increase of lithium concentration from 1M to 10M, the change in the infrared signal will be merely 3% of the measured signal. This effect therefore appears negligible.

During silicon lithiation the cathodic potential increases the cation concentration. The anion concentration is slightly affected by electrode processes, also leading to the increase in the absorbance vibration mode characteristic of perchlorate anion ClO_4^-, (1097 cm^{-1}), which cannot be clearly observed in Fig. 39 due to superposition with intensive positive-going signals. However, anionic composition of the diffuse layer is reestablished after the electrode complete delithiation and the absorbance band of ClO_4^- recover its original value. This reversible change in the anion concentration along the cycle sustains the behavior observed for cationic species during cycle.

The SEI layer has its own characteristic bands, as already mentioned. Fig. 39 shows that most parts of the observed infrared signals are evolving reversibly with electrochemical cycling, including bands correspondent to the SEI. Absorption intensities of SEI related species change with the cycling direction, increasing during lithiation and decreasing during delithiation, suggesting partial reversibility. Such a reversible aspect of the SEI is not obvious from the point of view of reaction mechanisms and is barely mentioned in the literature. However, some evidences of this phenomenon were already observed in different electrode materials, as for instance, in a-Si:H based electrodes, the reversible formation of Si-F bonds has been monitored by XPS measurements.[98] Microscopy measurements demonstrate that the formation of an organic layer surrounding Cu_2O particles, used as lithium-ion anode material, could be the responsible for a secondary reaction mechanism involving a reversible part of the SEI.[99] In the same way, the analysis of electrochemical lithiation of NiO film electrodes and carbon nanotubes demonstrated the formation of partially reversible SEI by cyclic voltammetry experiments.[100,101] Additionally, impedance studies of SEI formed on positive electrode materials indicated partial reversibility of the SEI formation.[102]

Both free and solvating solvent signals have their intensity affected by overlapping with bands belonging to SEI species. These overlaps can yield an underestimation of the negative absorbance values for solvent signals and an overestimation of the positive values of solvated signals. Independently of an exact estimation, the results suggest that the SEI is rich in solvated lithium species allowing for a good ionic conduction over this interface. It also attests the important role of the electrolyte as a precursor and active member of the SEI. Therefore, in situ FTIR experiments give particular evidence of a dynamic SEI layer, containing important amounts of electrolyte.

Negative-going bands indicate the loss of chemical species as a consequence of the chemical consumption, change on the vibration mode related to a change in the molecular environment or physical displacement caused by the growth of the SEI layer. Nevertheless, all these phenomena imply the change of the chemical landscape in the region probed by the infrared wave, which can be represented in a very simplified manner by the physical displacement of the pristine electrolyte. Then, from this point of view, the negative-going vibration modes can be considered as simply related to the loss of the global electrolyte signal due to its displacement caused by the growing SEI layer.

The most significant signal loss detected in the entire infrared range was the negative-going band at 1784 cm^{-1}, assigned to C=O stretching vibration in PC. This band presents an intense absorption signal already in the reference spectrum, with values close to the maximum limit of detection (all the infrared radiation absorbed in this spectral range). During the electrochemical lithiation C=O absorption signal is rapidly saturated, for this reason the quantitative analysis of such signal has not been taken into account. Fig. 41 illustrates the various contributions to the measured signal with emphasis to the C=O region,

exemplifying the spectrum deformation caused by the absorption saturation, and its comparison with experimental data in situ obtained in 1M LiClO$_4$ in PC.
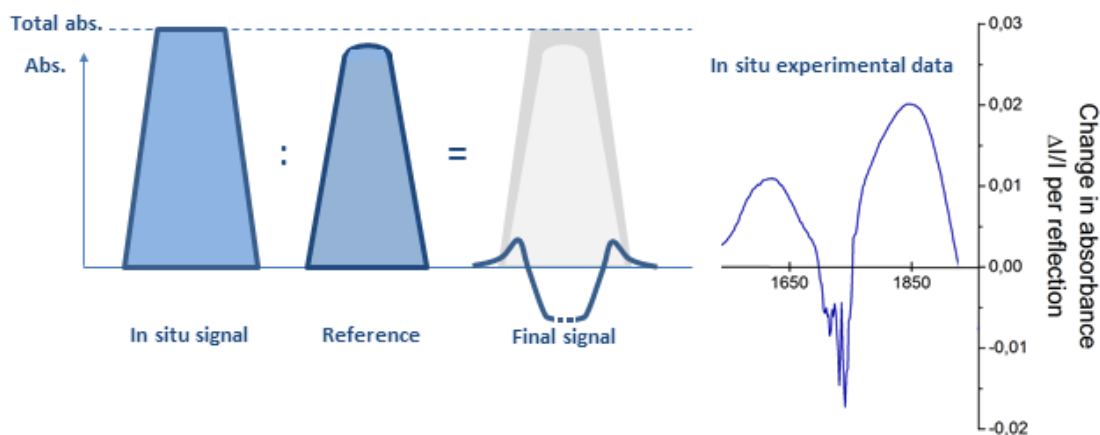

Fig. 41 – Illustration of the signal deformation caused by the strong C=O absorbance of the electrolyte.

Si-H consumption

Hydrogen is a key agent in the preparation of silicon-based devices for microelectronic or photovoltaic purposes. It is for example responsible for the semiconductive properties obtained through the passivation of dangling bonds by Si–H bond formed in amorphous hydrogenated silicon.[103] The PECVD technique allows for producing high quality a-Si:H films with (a high) hydrogen concentration in the deposited film whose value depends on the experimental conditions. Increased deposition rates result in higher concentration of bonded hydrogen and associated increase of internal strain in the a-Si:H bond network. This internal strain is therefore responsible for weakening the Si-Si bonds.[104]

The phenomenon of lithium storage into silicon electrodes is responsible for the breaking of Si-Si bonds during electrochemical lithiation, with the number of broken bonds proportional to the amount of lithium inserted into silicon.[105] Hence, we believe that bulk silicon hydrogenation plays an important role in the electrode lithiation. The weakened hydrogenated silicon network can favor the insertion of lithium atoms by decreasing the energy barrier for breaking the Si-Si bonds.[106] It can also be thought that Si-H bands, though much less numerous than Si-Si bands, are also favorable site for the incorporation of the lithium atoms, in view of the lower bond-dissociation energy of Si-H as compared to Si-Si.

Experimentally, Si-Si bonds have a IR-active vibration mode at 610 cm^{-1} which is out of the spectral infrared range of our measurements (950-4000 cm^{-1}).[107] However, it has been found that in a hydrogenated silicon network the very reactive atoms of lithium can

otherwise affect the infrared active Si-H bonds. This feature allows for in situ monitoring the electrode lithiation by infrared. The first steps of electrochemical lithiation are associated with negative-going peaks in the range of Si-H$_x$ species. As shown in Fig. 42, a negative band centered at 2115 cm^{-1} appears after charging the silicon electrode with a capacity of 60 mAh g^{-1}. This negative signal corresponds to the superimposition of different stretching vibration modes of surface species, such as Si-H$_2$ from 2101 cm^{-1} to 2129 cm^{-1}, Si-H$_3$ from 2130 cm^{-1} to 2150 cm^{-1} and SiH$_2$(SiO) at 2170 cm^{-1}.[103,109] Upon pursuing electrode lithiation the spectra demonstrate the consumption of species belonging to the bulk a-Si:H deposit, such as Si-H at 2004 cm^{-1} and Si-H$_2$ at 2086 cm^{-1}.[108] The signal is very intense and the spectrum corresponding to the end of the first electrochemical cycle in Fig. 42 was drawn divided by a factor of two to adjust it to the frame.

All the changes in the Si-H$_x$ bonds associated with the negative-going peaks in the Fig. 42 were obtained during electrode lithiation. The peak at 2004 cm^{-1} reaches its maximum amplitude at the end of the electrochemical lithiation and it is not regenerated with delithiation. This demonstrates that the loss of Si-H bonds is not reversible with cycling. The following cycles contribute to increase the loss of Si-H bonds, increasing the intensity of the negative-going peak at the end of each delithiation.
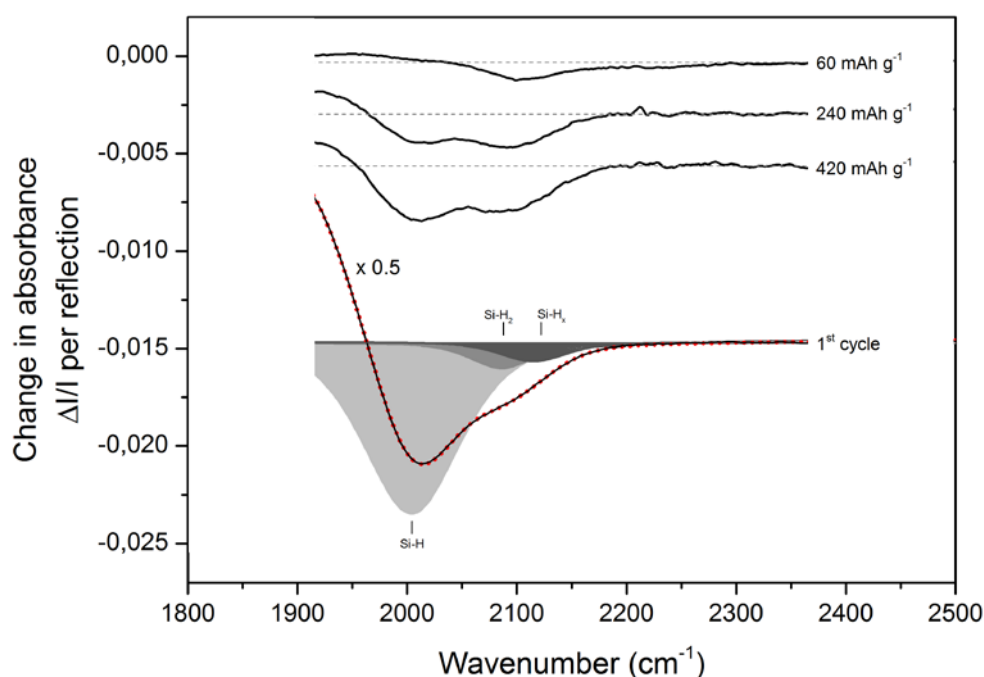
Fig. 42 – ATR-FTIR spectra obtained in situ at different steps of the electrochemical cycle (black lines). The negative envelope of the spectrum recorded after the first electrochemical cycle has been fitted (red dots) as the superposition of different Si-H species (gray scale) and an intense absorption peak on the low-wavenumber side of the spectral range of interest.

It was already mentioned that the intense absorption band of PC at 1784 cm^{-1} corresponding to the stretching of the C=O functional group, reaches values close to the

limit of detection. During electrochemical cycling this limit is reached and due to data processing results in a spectrum deformation in a spectral range from about 1640 cm^{-1} to 1980 cm^{-1}. This can be observed in Fig. 42 as the growth of a positive peak at low wavenumbers during the electrode lithiation. This distorted signal showed some partial reversibility with cycling in agreement with the reversibility of the SEI previously mentioned.

No particular evidence of surface oxide reduction was observed with silicon lithiation, however vibration mode of SiH$_2$(SiO) at 2170 cm^{-1} or SiH(Si$_2$O) at 2120 cm^{-1} could be overlapped with the previous mentioned Si-H$_x$ peaks making difficult its detection and quantification.[109]

Quantitative information about the number of Si-H bonds consumed during lithiation is hampered by the spectra deformation caused with the rising of SEI-related positive-going peaks. Even though, the loss of Si-H$_x$ signal was quantified by fitting the negative-going peak with mixed Gaussian and Lorentz functions centered at 2004 cm^{-1} for bulk Si-H, 2086 cm^{-1} for bulk Si-H$_2$ and 2115 cm^{-1} for superficial Si-H$_x$, as demonstrated by the gray peaks in Fig. 42. For the fitting procedure a baseline was chosen (dashed lines in Fig. 42) based in the very linear part of the curve between 2300 and 3000 cm^{-1} and not shown in the Fig. 42. Also, a Gaussian peak centered at ~1784 cm^{-1} was added to account for the absorption due to PC. The obtained values of fitting were compared with those measured for the hydrogenated a-Si:H layer and indicate that 93% of the Si-H bonds are consumed during the first electrochemical lithiation.

The hydrogen content of Si-H bonds in a-Si:H is estimated to be ~12 wt.%, by mass spectrometer in hydrogen effusion measurement,[104] in experiments performed on a-Si:H deposits prepared in similar conditions to those used in this work. Therefore, even if most of the hydrogen atoms in a-Si:H are not engaged in a Si-H bond, the absolute amount of hydrogen lost in the first electrochemical cycle of a-Si:H electrodes is massive and could tentatively be estimated to be ~11 wt.%. This large loss of hydrogen can have important effects on the SEI formation due to the fact that the electrode surface represents the border between the hydrogen source and the electrolyte and consequently the place where the released hydrogen will meet the SEI and electrolyte components. It is possible that the hydrogen participates on the chemical mechanism of SEI products and especially in the HF formation in LiPF$_6$ containing electrolytes, with detrimental effects for the SEI layer and even for the silicon electrode.

The role of the surface pretreatment

As previously mentioned in the second chapter, pristine a-Si:H electrodes form a native oxide layer when exposed to atmospheric conditions. It was also verified that the electrochemical performance of pristine amorphous silicon could be improved by oxide etching and especially by the introduction of a molecular monolayer of undecylenic acid. Coupled infrared and electrochemical experiments have therefore been undertaken for identifying in detail the origin of the effect of silicon surface treatment on the electrochemical performance.

Different surface treatments were tested on a-Si:H electrodes prepared by thin film deposition on the surface of ATR crystals. On the basis of the results reported in chapter 2, pristine electrodes, surface hydrogenated electrodes and acid-surface electrode have been selected for a detailed study. Electrochemical cycling was performed in 1M $LiClO_4$ in PC. Fig. 43 presents the spectra obtained at the end of first, fifth and tenth electrochemical cycles for the different surface treatments. The spectra are presented for a region between 1100 cm^{-1} and 1720 cm^{-1} characterized by the signal of SEI products (Fig. 43a) and a second region from 2500 cm^{-1} to 3700 cm^{-1} with less intense signals as indicated by the absorbance scale (Fig. 43b).
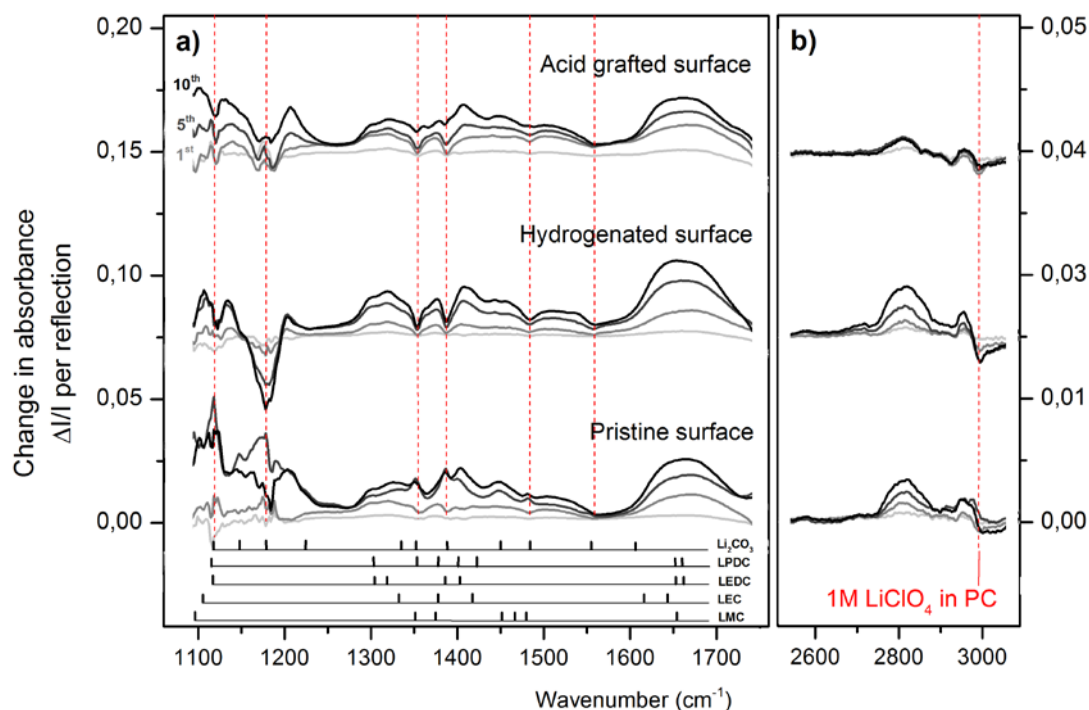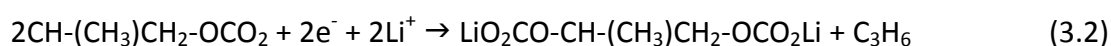

Fig. 43 – ATR-FTIR spectra in situ obtained in the delithiated state after 1, 5 and 10 cycles, for silicon electrodes with different surface conditions. Labels on the bottom of the figure indicate the location of absorption bands of possible SEI products. The red dashed lines correspond to the position of the main absorption bands of the electrolyte.
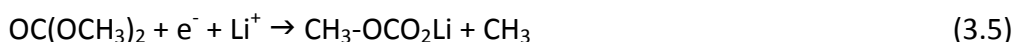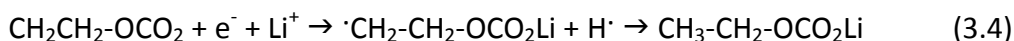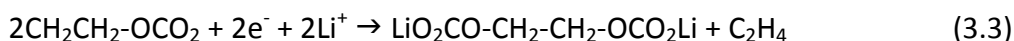
As shown in Fig. 43, different silicon surface pretreatments leads to different SEI composition and formation kinetics. Some SEI features are common to all the surfaces, indicating the strong dependence on the electrolyte composition. Even if the silicon surface had been intentionally modified by the different surface treatments the origin of the SEI layer is still the same for all the cells which leads to a roughly similar SEI chemical composition. In this case, the previous general description of electrolyte decomposition and SEI formation reactions were precisely identified.

The formation of alkyl carbonates, up to now represented by the general term $ROCO_2Li$, is expected to mostly correspond to lithium propylene dicarbonate (LPDC) in the case of the electrochemical reduction of propylene carbonate, as described below.[110,111]

$$2CH\text{-}(CH_3)CH_2\text{-}OCO_2 + 2e^- + 2Li^+ \rightarrow LiO_2CO\text{-}CH\text{-}(CH_3)CH_2\text{-}OCO_2Li + C_3H_6 \qquad (3.2)$$

The vibration modes associated to this species are located among the positive bands in situ measured for different silicon surface states. Moreover, the peaks characteristics of Li_2CO_3 are also contributing to the positive signals observed. However, combining both respective signals is not enough for addressing the entire group of infrared signals obtained. The results of in situ measurements reveal the presence of flattened peaks centered at specific position corresponding to the vibration modes of most of the identified SEI components, but having a certain distribution in chemical composition or chemical environment accounting for the absence of sharp absorbance signals. It is known, for example, that SEI components are not only related to simple $ROCO_2Li$ species but to a polymeric matrix or network of lithium ion coordinated compounds, which could result in enlarged infrared signals.[112,113] Moreover, $ROCO_2Li$ can be further reduced in the surface film or by reaction with trace water in solution to form not only Li_2CO_3 but also ROLi and CO_2, increasing the number of infrared active species in the SEI.[114]

Propylene carbonate is one of the most saturated solvent molecules used for electrolyte in Li-ion batteries. Such a molecular chain ideally produces lithium propylene dicarbonate (LPDC) as a main reduction product, however it does not necessarily corresponds to the complete range of reaction possibly obtained from the PC molecule, especially in a rich and dynamic chemical environment. Other commonly used solvents such as EC, DEC, DMC ideally generate under electrochemical reduction specific products such as lithium ethylene dicarbonate (LEDC), lithium ethyl carbonate (LEC) and lithium methyl carbonate (LMC), respectively, according to:

$$2CH_2CH_2\text{-}OCO_2 + 2e^- + 2Li^+ \rightarrow LiO_2CO\text{-}CH_2\text{-}CH_2\text{-}OCO_2Li + C_2H_4 \qquad (3.3)$$

$$CH_2CH_2\text{-}OCO_2 + e^- + Li^+ \rightarrow \,^{\cdot}CH_2\text{-}CH_2\text{-}OCO_2Li + H^{\cdot} \rightarrow CH_3\text{-}CH_2\text{-}OCO_2Li \qquad (3.4)$$

$$OC(OCH_3)_2 + e^- + Li^+ \rightarrow CH_3\text{-}OCO_2Li + CH_3 \qquad (3.5)$$

However, one can assume that during homolytic ring opening and radical anion formation of PC it can be further terminated via various reactions with solvents, contaminations and other decomposition products leading to the formation of SEI compounds not necessarily predicted to be generated according with the Eq. 3.2. We added in Fig. 43 (labels in the bottom of the figure) the position of the main vibration modes of LPDC together with LEDC, LEC and LMC in order to show the possible correspondence of representative carbonate decomposition products with the experimental results obtained.

The finger print region in the Fig. 43, specifically from 1240 cm^{-1} to 1720 cm^{-1}, demonstrates the presence of chemical species different from LPDC and Li_2CO_3. This leads us to believe that other decomposition products are possibly generated along the SEI formation and also that the in situ measurements are able to detect the presence of the byproducts with less-defined vibration modes, not yet identified elsewhere.

Another source of SEI components, and potential source of infrared signals as well, is represented by the intrinsic presence of trace contaminants which can react with the very active lithium ion species. The equations listed below indicate the products generated by the most common sources of contamination in Li-ion batteries.[114] For example, the presence of CO_2 contamination leads to Li_2CO_3 formation according to Eq. 3.6a-c.

$$CO_2 + e^- + Li^+ \rightarrow CO_2Li \qquad (3.6a)$$

$$CO_2Li + CO_2 \rightarrow O\text{=}CO\text{-}CO_2Li \qquad (3.6b)$$

$$CO_2Li + CO_2 \rightarrow O\text{=}CO\text{-}CO_2Li \;\; + e + Li^+ \rightarrow CO + Li_2CO_3 \qquad (3.6c)$$
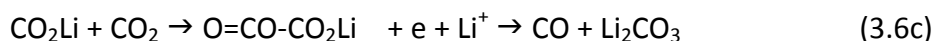
Water traces leads to the formation of LiOH, Li_2O and LiH, as shown by Eq. 3.7a-c.

$$H_2O + e^- + Li^+ \rightarrow LiOH + \tfrac{1}{2}H_2 \qquad (3.7a)$$

$$LiOH + e^- + Li^+ \rightarrow Li_2O + \tfrac{1}{2}H_2 \qquad (3.7b)$$

$$H + e^- + Li^+ \rightarrow LiH \qquad (3.7c)$$
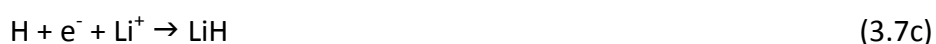
In the reaction with water traces, the lithium protonation step could be especially favorable for amorphous silicon electrodes since the material has a large hydrogen content which is affected by the electrode lithiation and probably turns for being injected in the electrolyte during the first lithiation. Unfortunately, the vibrational signature of Li-H bond located around 4050 cm^{-1} is out of the spectral range of our experiments and the possible formation of LiH as described by the Eq 3.7c cannot be directly identified.[115] The presence of nitrogen and oxygen contaminations leads to the respective production of Li_3N and LiO_2, according to Eqs. 3.8-3.9c.

$$N_2 + 6e^- + 6Li^+ \rightarrow 2Li_3N \tag{3.8}$$

$$O_2 + e^- + Li^+ \rightarrow LiO_2 \tag{3.9a}$$

$$LiO_2 + e^- + Li^+ \rightarrow Li_2O_2 \tag{3.9b}$$

$$Li_2O_2 + e^- + Li^+ \rightarrow 2LiO_2 \tag{3.9c}$$

The information collected by screening the main possible SEI compounds produced by electrochemical reduction of the electrolyte or contaminant induced reactions of $LiClO_4$ containing PC were used for identifying in detail the contribution of surface treatment state on the SEI formation, according to the results presented on Fig. 43. Therefore, different aspects were examined: the relative amount of SEI compounds, $ROCO_2Li$, Li_2CO_3 and the presence of the methoxy group (-OCH_3); SEI homogeneity and covering efficiency has been inferred by analyzing the solvent-related infrared peaks.

$ROCO_2Li$ species were identified by the vibration modes in three main regions at 1100-1140 cm^{-1}, 1300-1480 cm^{-1} and 1615-1660 cm^{-1} where LPDC, LEDC, LEC and LMC compounds, which exhibit peaks close to each other in these spectral ranges. A combination of these compounds or other related decomposition products can be responsible for the broad shape of the measured signal.

In the case of Li_2CO_3, most of its vibration modes are overlapping with $ROCO_2Li$ signals in the region of 1330-1610 cm^{-1}, making the analysis difficult on the basis of these vibrational bands. Additionally, Li_2CO_3 present four absorption peaks at 1118 cm^{-1}, 1146 cm^{-1}, 1178 cm^{-1} and 1225 cm^{-1}, where the band at 1178 cm^{-1} coincides with strong electrolyte absorption at 1176 cm^{-1} (v_{as} C-O-C in PC). However, even with this overlapping, features related to Li_2CO_3 spectrum can be identified and followed during the cycling life using the three other signals in the 1110-1225 cm^{-1} region. Also, the intensity of Li_2CO_3 vibration modes in the first region (1330-1610 cm^{-1}) is very weak as compared to the intensities in the second region (1110-1225 cm^{-1}). We can therefore consider that a significant amount of Li_2CO_3 will result in the rise of signals in the 1110-1225 cm^{-1} region.

SEI homogeneity and covering efficiency can indirectly be deduced from the main electrolyte absorption bands. The growth of the SEI layer tends to displace the electrolyte away from the silicon surface, resulting in a negative contribution for the vibration modes corresponding to electrolyte species. It is believed that an efficient covering SEI layer will displace uniformly the electrolyte from the electrode surface leading to clear and sharp negative-going peaks. This phenomenon is clearly identified on Fig. 43 by the presence of negative-going peaks that emerge in the middle of positive signals addressed to SEI compounds. These negative contributions coincide with the main electrolyte signals identified by the dashed red lines in Fig. 43.

Hydrogenated surface

The results obtained for silicon electrodes surface hydrogenated by chemical etching indicate the formation of an homogeneous SEI layer with high solvent blocking capability, which is identified by the clear formation of negative-going signals, as shown in Fig. 43a. Silicon surface hydrogenation also induces the formation of a $ROCO_2Li$ rich SEI layer identified by the presence of strong signals at 1280-1560 cm^{-1} and 1650 cm^{-1}. This SEI layer was shown to have sizeable methoxy content, as indicated by the absorption band centered at 2820 cm^{-1} in the Fig. 43b. This fact gives evidence for the possible formation of decomposition products not necessarily following the model chemical reactions predicted for PC based electrolytes.

Additionally, the SEI formed on hydrogenated electrodes exhibit a low content in Li_2CO_3, as revealed by the absence of signals in the 1110-1225 cm^{-1} region. In this spectral range, the only vibration modes are related to the electrolyte displacement (negative-going at 1176 cm^{-1}) and lithium ion solvation (1134 cm^{-1} and 1209 cm^{-1}).

In general, silicon hydrogenation leads to a continuous formation of homogeneous SEI layers from cycle to cycle, as verified by the progressive increase of the infrared signals corresponding to SEI products. The measured spectra follow an homothetic evolution along the electrochemical cycling life with constant proportion ratio among all the vibration modes, which suggests a high chemical stability and an homogeneous in-depth composition. As shown previously, surface and bulk Si-H bonds in a-Si:H are highly affected by the electrode lithiation. In particular, most part of the surface hydrogen is lost during the first electrode lithiation. Such a deprotonation takes place during the SEI formation and can have effects on SEI formation and stability.

Acid surfaces

Compared with hydrogenated silicon, electrodes treated by surface-grafting of undecylenic acid result in a modified SEI layer which is quickly formed and exhibit a mixed $ROCO_2Li/Li_2CO_3$ chemical composition. $ROCO_2Li$ compounds were identified by the strong vibrational modes in the 1100-1140 cm^{-1}, 1280-1560 cm^{-1} and 1650 cm^{-1} ranges, while Li_2CO_3 was identified by the signals in the 1110-1225 cm^{-1} region. This region is specifically modified in the case of undecylenic acid grafted surface, showing a set of well-defined positive peaks mixed with negative contribution of electrolyte displacement, as shown in Fig. 43a. It gives evidences not only for the presence of Li_2CO_3 but also for the formation of an homogeneous and passivating SEI layer.

Surface grafting also affects the kinetics of SEI formation by allowing for a fast electrolyte reduction and passivation layer formation during the first cycle. This passivation layer is mainly composed of LMC-rich $ROCO_2Li$ species, as evidenced by the stable methoxy vibration band formed during the first electrochemical cycle. In the following electrochemical cycles the SEI growth keeps on, however with a different chemical composition. It is now composed of general $ROCO_2Li$ compounds and Li_2CO_3, as indicated by the rise of signals in all the SEI active regions, except the methoxy band.

Pristine surface

The effect of silicon electrode surface chemical state on the electrolyte reduction is evident when the results of surface modified silicon are compared with the pristine material. Without any surface modification, silicon electrodes develop a SEI layer with a mixed chemical composition of $ROCO_2Li$ and Li_2CO_3, with very unstable nature, inhomogeneous and which continuously grows. Its mixed chemical composition is revealed by the intense vibration modes obtained for all the identified SEI species in the spectral range shown in Fig. 43. Part of these signals show irregular intensity variations along the cycling life, which is probably due to the formation and further detachment of the SEI compound, demonstrating the instability of SEI layers formed on pristine silicon. The near absence of electrolyte displacement is attested by the weakness of negative-going signals, which are only observed for the first electrochemical cycle. This suggests that the SEI layer is inhomogeneous and quite porous. Most of the SEI infrared signals show a constant growth along cycling, with an exception for the bands located in the 1110-1225 cm^{-1} region attributed to Li_2CO_3. Li_2CO_3 is intensively formed after the first cycle until the fifth cycle and partially lost from there to the

tenth cycle. Once again such a fluctuation in the SEI composition highlights the low stability of the SEI formed on pristine electrodes.

Electrochemical performance and correlation with SEI characteristics

Fig. 44a shows the first electrochemical cycle of a-Si:H based electrodes with different surface preparation, where pristine electrode exhibits a lithiation capacity of 2750 mAh g^{-1}, a delithiation capacity of 1720 mAh g^{-1} and a resulting irreversible capacity of 1030 mAh g^{-1}. In the infrared cell, hydrogenated electrodes exhibit electrochemical performance (in terms of capacity) close to those of pristine electrodes (though somewhat better). On the other hand, the grafting of silicon surface with undecylenic acid decreases the lithiation capacity to 2445 mAh g^{-1}, increases the delithiation capacity to 1840 mAh g^{-1}, resulting in the decrease of irreversible capacity to 605 mAh g^{-1} and a coulombic efficiency of 0.75 in the first electrochemical cycle. The evolution of the irreversible capacity for the three electrodes during the first ten cycles is shown in Fig. 44b. Such results confirm the benefits of surface grafting for the electrochemical performance of silicon based electrodes.
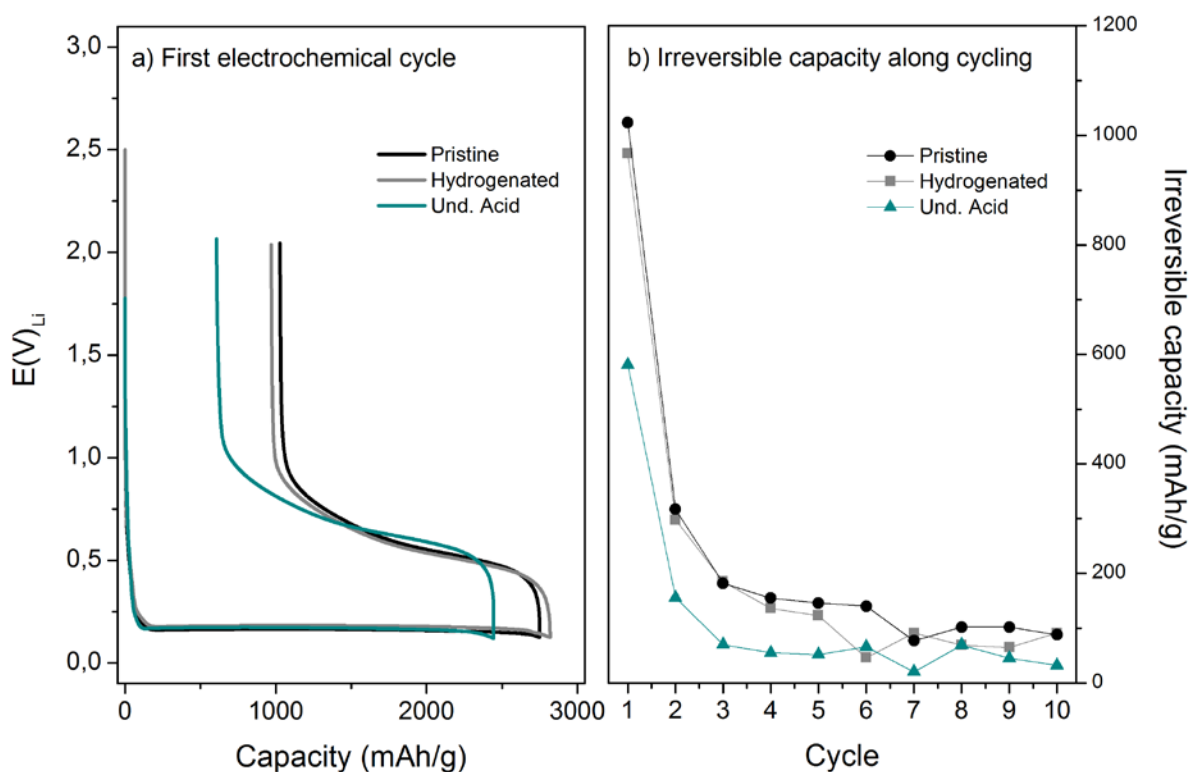
Fig. 44 – Electrochemical cycling of amorphous silicon layers with different surface treatments in 1M LiClO$_4$ in PC using the in situ FTIR cell. First electrochemical cycle (a) and the irreversible capacity along cycling (b).

Electrochemical performances of a-Si:H thin films obtained by in situ experiments are similar to those observed for the first electrochemical cycle in standard electrochemical cells and based on stainless steel substrates presented in the first chapter. Small quantitative differences are associated with the change of the potential boundaries, but general trends are preserved, validating the experimental setup developed for the coupling of infrared and electrochemical measurements.

Attempts for quantifying the amount of SEI products generated along the electrochemical cycling have to manage the difficulty of simultaneously accounting for the vibration bands of the expected decomposition products and the loss of electrolyte signals with the in situ measured FTIR spectra. When fitted to experimental data, such a simultaneous combination of signals did not converge to acceptable values, probably due to the large number of computed parameters necessary for reproducing the spectroscopic results. Therefore, in order to quantify the SEI layer, the in situ obtained FTIR signals were integrated numerically in the most significant spectral ranges for SEI compounds signals, as such labeled in Fig. 43: 1100-1720 cm^{-1} and 2660-2980 cm^{-1}.

The results obtained from the integrated FTIR signals were plotted as a function of the cycle number and correlated to the cumulated irreversible capacity, as shown in Fig. 45a-d. Fig. 45a-c indicates a relatively intense SEI layer growth upon electrolyte reduction on pristine electrodes and a more gradual reaction on surface modified silicon electrodes. However, a somewhat different picture results from the relation between integrated absorbance and cumulated irreversible capacity, Fig. 45d. Under this perspective, the amount of SEI compounds, here represented by the integrated FTIR signal, is linearly proportional to the charge consumed irreversibly in the system. It suggests a close relation between the electrochemical reduction of the electrolyte and the growth of the SEI layer. From this point of view, an enhanced efficiency for SEI formation appears obvious for grafted electrodes. Compared with hydrogenated or pristine silicon electrodes, a grafted surface appears to impede the irreversible electrochemical processes not associated with SEI formation, and therefore offers enhanced kinetics of SEI formation. It results in a more efficient use of the charge consumed for electrolyte reduction, producing a similar amount of electrolyte decomposition products with decreased charge consumption.
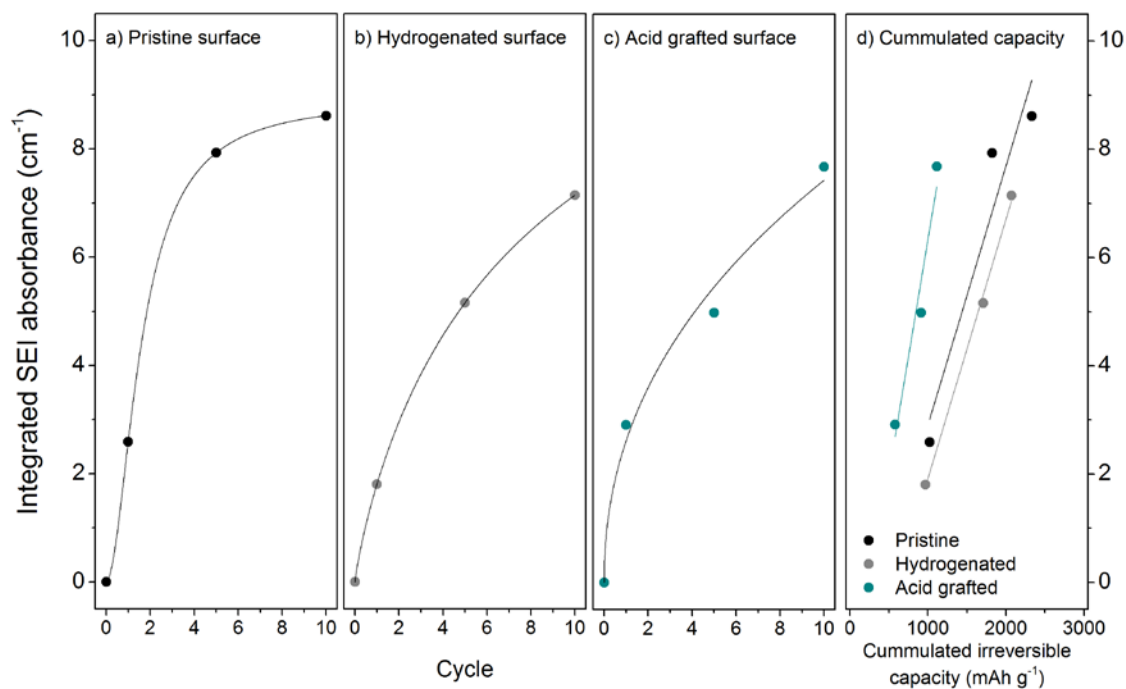
Fig. 45 – Integrated FTIR signals of SEI compounds for different silicon surface states during electrochemical cycling life (a-c) and correlated to the cumulative irreversible capacity (d). [‡]

We believe that the presence of an hydrogenated monolayer of silicon on the electrode surface can result in an improved activity for SEI formation and anchoring by offering a very reactive connection between radicals generated during the electrolyte reduction and the active material, a chemical bonding substantially stronger than the simple adsorption of the decomposition products.

The carboxyl-terminated molecular monolayer results in an efficient protection of the surface although it might be permeable to ionic species and some solvent penetration, as verified elsewhere.[70] Such properties are possibly due to a controlled solvent approach with simultaneous high ionic exchange through the molecular layer, allowing for leveling the reactivity of the electrode surface. Carboxyl-terminated molecules then participate to the electrolyte reduction by permitting selective approach of solvent molecules at specific surface sites, targeting the charge transfer and SEI compound formation. This allows for improved charge transfer efficiency for the electrolyte reduction reaction at the same time as homogeneous SEI layer formation.

[‡] The lines going through the experimental point in Fig. 45 were obtained by a fitting the experimental points by Hill function ($y = (y_{max} \cdot x^n) / (k^n + x^n)$) and are only guides for the eye.

The role of electrolyte composition

Based on the fact that the SEI layer originates from the decomposition products of the electrolyte, the electrolyte composition must play a major role in the physicochemical characteristics of the SEI. Chemical composition of frequently used electrolytes shares a common group of organic solvents. However, even having similar chemical composition, different types of carbonates exhibit distinct physicochemical properties and their combination is used for tailoring flashing and boiling point, melting temperature, viscosity and others parameters. Additionally, each electrolyte component has a distinct chemical stability under electrochemical cycling, which allows for programming the preferential decomposition of target species and tailoring the chemical composition of the SEI. This is the case of reduction-type electrolyte additives that undergo preferential decomposition for improving SEI passivation properties without affecting the global properties of the electrolyte. Besides the specific role played by solvents and additives, the lithium salt in the electrolyte composition also affects the chemical composition of the SEI layer.

Since vinylene carbonate (VC) introduction as an electrolyte additive by SAFT in 1997,[116] a large number of studies were dedicated to characterize its properties and the resulting SEI layer induced by this compound. However, there is still a large discussion about the role of VC in the electrolyte reduction and SEI formation. It is believed that the high reduction potential of VC favors its preferential reaction prior to solvent decomposition (even though the VC reduction has a reaction enthalpy comparable to that of EC or PC, it has a lower activation energy).[117] VC has a positive effect for both positive and negative electrodes, improving cyclability, especially at elevated temperatures, and reducing the irreversible capacity. It was found that VC is responsible for forming poly alkyl Li-carbonate species that suppress both solvent and salt anion reduction.[118] This polymeric product can be obtained by the radical polymerization of VC at the surface of both electrodes.[119] However, it was also suggested that the VC can participate in the reduction of organic solvents by assisting the electron transfer from the electrode to the solvent molecule coordinated with Li^+, launching the initial process of reductive decomposition of the electrolyte.[113,114]

Another important electrolyte additive is fluoroethylene carbonate (FEC). The use of FEC was initially proposed as a solution for the chemical shuttle obtained with the use of chloroethylene carbonate as electrolyte component.[120] FEC allows for the formation of more stable SEI layers with high proportion of LiF, resulting in low interfacial resistance in Li-ion electrodes.[121,122] Also, it was noticed for silicon nanowires that FEC helps in reducing the irreversible capacity losses, enhancing and stabilizing the reversible capacities over prolonged cycling, even at elevated temperatures. It is believed that FEC decomposes first into VC which will then form polymeric or oligomeric species responsible for generating a polymer-like film on the electrode surface.[123] Therefore, it can be expected that both VC and

FEC result in the formation of similar SEI layer containing polymeric species resulting from the reduction of VC.

Here we investigate the use of these two different electrolyte additives, each of them having its particular way of action. With respect to the electrolyte lithium salt, $LiPF_6$ was considered as an alternative to $LiClO_4$. Therefore, ATR-based silicon electrodes were electrochemically cycled in the previous mentioned setup, allowing for in situ FTIR measurements of the electrode/electrolyte interface. The experiments were performed in an electrolyte composed of 1M $LiPF_6$ in PC:EC:3DMC using 2 wt.% of vinylene carbonate (VC) and 10 wt.% of fluoroethylene carbonate.

The spectral signature of 1M $LiPF_6$ in PC:EC:3DMC (2% VC, 10% FEC) is mostly based on the vibration modes of EC, DMC and PC. EC is identified by its CH_3 twisting vibration mode at 1480 cm^{-1}, the vibration of the C-O skeleton at 1195 cm^{-1} and the ring stretching at 1156 cm^{-1}.[95,124] The presence of DMC is identified by the symmetric and asymmetric vibration modes of CH_3 at 1436 cm^{-1} and 1458 cm^{-1}, respectively.[125] Additionally, the asymmetric stretching vibration of C-O-C in DMC is identified at 1277 cm^{-1} and its solvated pair at 1322 cm^{-1}.[126] The PC content in the electrolyte is recognized by the CH_3 deformation and OCH_2 at 1389 cm^{-1}, C-O-C asymmetric stretching at 1170 cm^{-1} and its solvated pair at 1209 cm^{-1}.[94,95] Table 3 presents the most representative infrared signals identified for 1M $LiPF_6$ in PC:EC:3DMC (2% VC, 10% FEC) in the fingerprint region.

Table 3 – Band assignments of 1M $LiPF_6$ in EC:DMC:PC (2% VC, 10% FEC) in the fingerprint region, where ν stands for stretching modes, δ for deformation modes, τ for twisting modes, ω for wagging modes and ρ for rocking modes.

Functional groups	Component	Mode	Vibration (cm^{-1})
C=O	PC	ν	1784
	EC	ν	1760, 1790, 1825, 1860
	DMC		1775, 1810
Ring	EC	ν	1156
C-O-C	PC	ν_{as}	1170
	PC	ν_{as} solvated	1209
C-O skeleton	EC		1195
C-O-C	DMC	ν_{as}	1277
	DMC	ν_{as} solvated	1322
OCH_2	PC	ω	1389
	PC	ω solvated	1408
CH_3	PC	δ	1389
	DMC	δ_s	1436
	DMC	δ_{as}	1458
	EC	τ	1480

FTIR spectra of a-Si:H based electrodes were in situ obtained during electrochemical cycling in 1M $LiPF_6$ in PC:EC:3DMC (2% VC, 10% FEC) and compared to the spectra obtained in 1M $LiClO_4$ in PC, as shown in Fig. 46. The spectra obtained for a-Si:H in $LiPF_6$ based electrolyte appear drastically different from those obtained in $LiClO_4$. The main feature observed for in the spectra recorded upon electrochemical cycling in the $LiPF_6$ based electrolyte is the formation of intense negative-going bands along the cycling life. The spectrum of the 1M $LiPF_6$ in PC:EC:3DMC (2% VC, 10% FEC) electrolyte has been plotted at the bottom of Fig. 46 in order to highlight its similarity with the negative bands of the spectra recorded in situ during electrochemical cycling. Fig. 46b shows the high-wavenumber region with a different absorbance scale (enlarged by a factor of six). Here also, we can notice a clear difference between the two electrolytes. The negative-going bands present in all the spectra correspond to most of the vibrational modes identified for species belonging to the electrolyte, indicating an intense change at the electrode surface during electrochemical cycling.

Most of the FTIR positive signals observed in $LiClO_4$ based electrolytes and previously identified as SEI components were affected by the intense negative bands caused by the electrolyte displacement for experiments performed in $LiPF_6$ based electrolytes. With such a negative contribution these intense bands could mask the trace of positive contribution originating from SEI products. However, it is possible to identify some positive signals unambiguously belonging to SEI components at 1500-1550 cm^{-1} and 1600-1700 cm^{-1}, and bands corresponding to solvation pairs modification with cycle at 1209 cm^{-1} for asymmetric stretching of C-O-C in PC and 1408 cm^{-1} for wagging of OCH_2 in ion solvating PC. In the $LiPF_6$ based electrolyte, the positive signals near 1209 cm^{-1} and 1408 cm^{-1} can unambiguously be essentially ascribed to signal arising from ion-solvating PC molecules: in this case, the signals associated to carbonate and alkyl carbonate species in the SEI are practically absent. The rising of this positive signal means that the Li^+-solvating PC has its concentration increased during the electrochemical cycling. This indicates that the Li^+-solvating PC is preferentially trapped into the SEI layer, while all the other solvents are displaced by the growth of the SEI layer. The relative absence of SEI signals with vibration modes similar to those observed in $LiClO_4$ electrolytes is counterbalanced by the presence of positive signals between 1000 cm^{-1} and 1150 cm^{-1} related to the C-O vibration stretching in ROLi and the formation of poly(VC).[127,128]
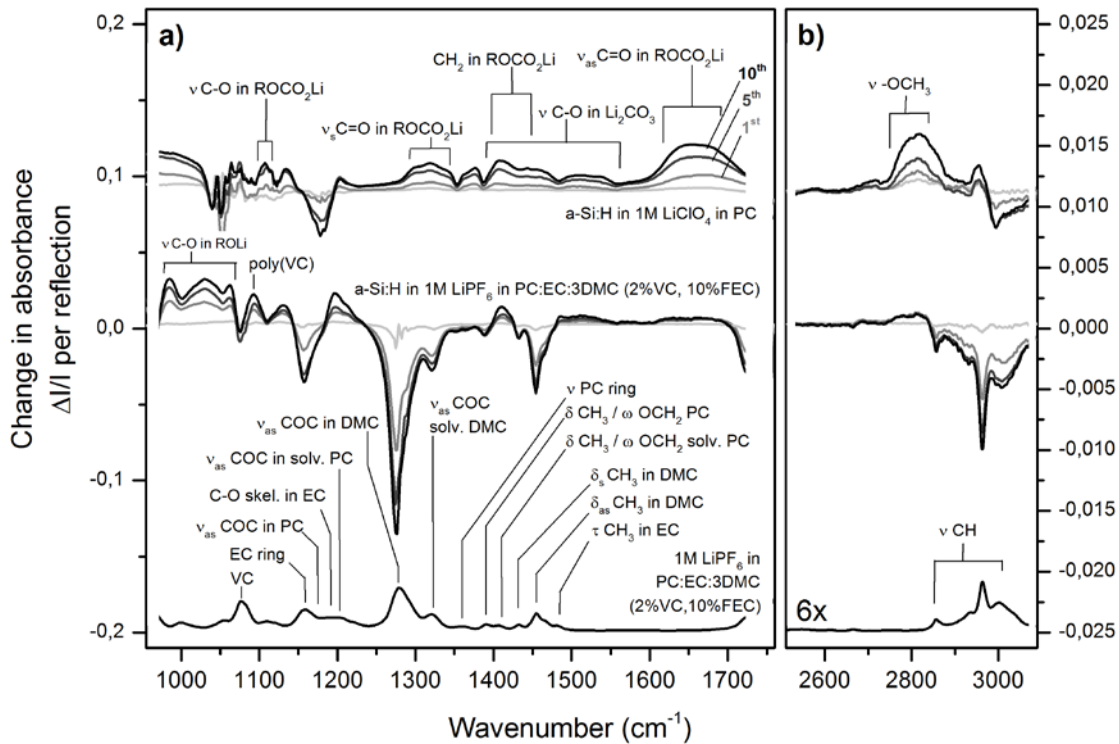
Fig. 46 – ATR-FTIR spectra of a-Si:H obtained in situ during electrochemical cycling in 1M LiClO$_4$ in PC and 1M LiPF$_6$ in PC:EC:3DMC (2% VC, 10%FEC).

The in situ FTIR measurements obtained for amorphous silicon based electrodes in 1M LiPF$_6$ in PC:EC:3DMC (2% VC, 10% FEC) reveal the formation of polymeric VC during the first electrochemical cycle. Actually, poly(VC) compound have most of its characteristic vibration bands located in the regions of strong electrolyte absorption or out of the spectral accessible range, at 1817 cm^{-1}, 1147 cm^{-1} and 758 cm^{-1}, according to reference 129. Only the broad absorption band located at 1080 cm^{-1} could be used for characterizing the formation of poly(VC) on silicon electrodes. It was observed that poly(VC) is constantly being formed and its total amount practically triplicates within ten electrochemical cycles.

It was already observed elsewhere that the surface film formed in LiPF$_6$ based electrolytes has an important variety of inorganic composition.[130,131] The production of inorganic compounds in the presence of LiPF$_6$ comes from its unavoidable decomposition but also can be increased by water contamination, as shown in Eq. 3.10a-d.[114,132]

$$LiPF_6 \rightleftarrows LiF + PF_5 \tag{3.10a}$$

$$PF_5 + H_2O \rightarrow PF_3O + 2HF \tag{3.10b}$$

$$PF_5 + 2xLi^+ + 2xe^- \rightarrow Li_xPF_{5-x} + xLiF \tag{3.10c}$$

$$PF_3O + 2xLi + 2xe^- \rightarrow Li_xPF_{3-x}O + xLiF \tag{3.10d}$$
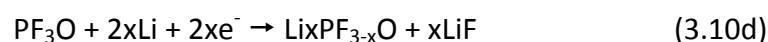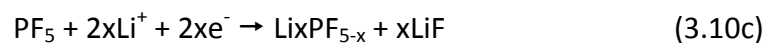
Unfortunately, most of the infrared signals from inorganic compounds possibly formed in the studied system are located out of the accessible spectral range or in regions of intense absorption of silicon. In this case, we search for evidences of inorganic compounds formed on silicon based electrodes deposited on ATR crystal made from germanium, even though this system does not allow us to finely control the state of the lithiation achieved by the silicon thin film, as previously discussed in this chapter.

In this case, FTIR was in situ measured for a silicon thin film deposited on a germanium ATR crystal and used as an electrode during silicon electrochemical lithiation. The spectrum shown in Fig. 47 has been recorded when the potential reaches the lithiation plateau (i.e., at a stage where a significant part of the SEI is thought to have been formed). The spectrum confirms the presence of different inorganic species generated from the decomposition of $LiPF_6$: Si-F, Si-F_2, Si-F_3 and P-O-C.[98]
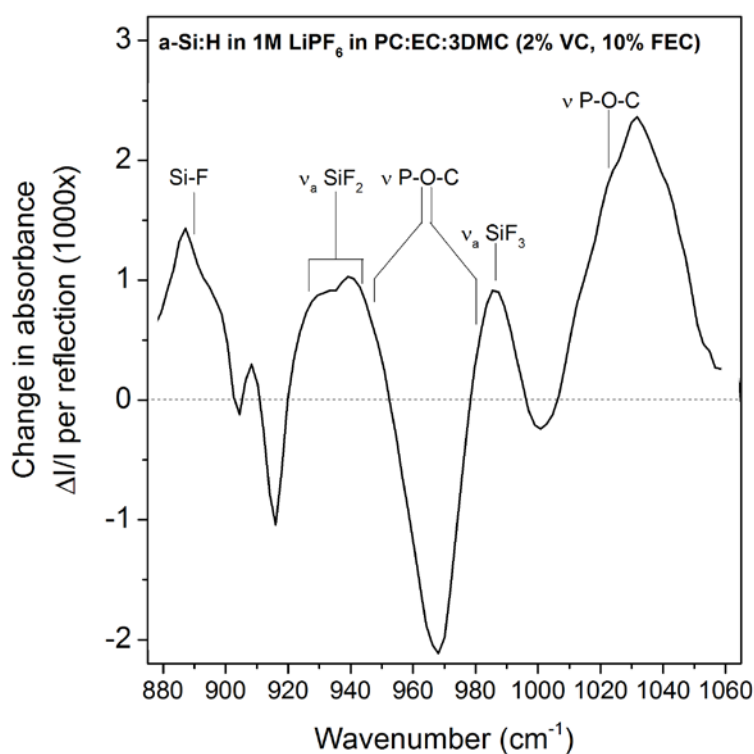
Fig. 47 – FTIR spectra of a-Si:H obtained in situ in 1M $LiPF_6$ in PC:EC:3DMC (2% VC, 10%FEC) using a germanium ATR crystal.

The differences in the SEI composition obviously result from the change in the electrolyte composition and have consequences on the electrochemical performance of the electrodes. Comparing the capacity values of a-Si:H based electrodes electrochemically cycled in 1M $LiClO_4$ in PC to those obtained in 1M $LiPF_6$ in PC:EC:3DMC (2% VC, 10% FEC), we

noticed an increase in the irreversible charge for cycling in $LiPF_6$ based electrolyte. Fig. 48 shows the electrochemical response of in situ experiments in 1M $LiClO_4$ in PC and 1M $LiPF_6$ in PC:EC:3DMC (2% VC, 10% FEC) during the first electrochemical cycle. The presence of an electrochemical peak at the very beginning of the electrode lithiation, from about 1.25 V vs. Li/Li$^+$ until the lithiation plateau, highlights the presence of intense electrochemical reactions prior to silicon lithiation, such as the preferential reduction of electrolyte additives. In general, electrochemical cycling of silicon in the $LiClO_4$ based electrolyte results in an apparent lithiation capacity decreased by 380 mAh g^{-1} as compared to the $LiPF_6$ based electrolyte. This is obtained practically without affecting the reversible capacity, which is decreased only by 50 mAh g^{-1}, resulting in a decrease of the irreversible capacity by 330 mAh g^{-1}.

Fig. 48 – Electrochemical cycling of amorphous silicon electrodes in different electrolytes using the in situ FTIR cell.
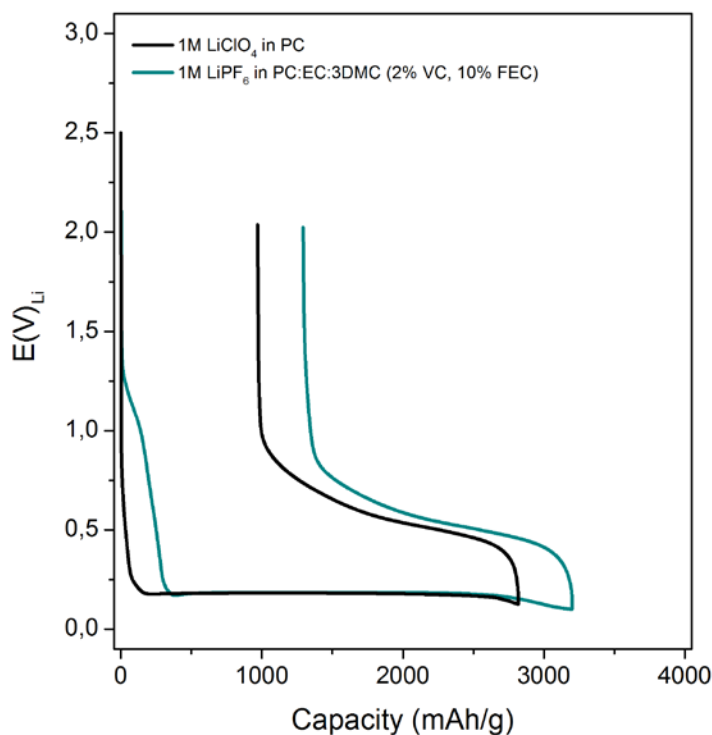
SEI thickness estimation

The presence of negative-going infrared bands, previously explored in this chapter, was accounted for in terms of the formation of the SEI layer resulting from the consumption of chemical species present in the electrolyte and yielding electrolyte displacement away from the silicon surface. The infrared signal collected in ATR geometry comes from the infrared absorption experienced by the evanescent wave within its penetration depth into the electrolyte. The SEI layer can be imagined as a moving barrier coming from the electrode/electrolyte interface and growing into the electrolyte. This layer contains not only the decomposition products due to electrolyte instability, but is in a first approximation free of electrolyte. In a more realistic picture it contains some electrolyte, especially the solvent molecules that during the lithiation/delithiation are affected by the electrode processes. The solvent molecules exhibit peculiar spectroscopic signature because they are modified by the change in the lithium concentration, resulting in different solvation configurations along the electrochemical cycle, but also by the chemical environment. For example, once trapped in the SEI layer, PC can still keep its solvent properties and allow for an effective ionic conduction in the passivation layer.

SEI therefore appears as a transition layer between the bulk electrolyte and the solid electrode, containing different chemical species from the decomposition products, solvated Li$^+$ ions, and a somewhat modified electrolyte composition. This SEI layer also presents a dynamic behavior, changing its chemical composition and effective thickness during each electrochemical cycle but also from cycle to cycle. All these characteristics turn the concept of SEI to be complex, with an important factor related to the solvation and diffusion properties of the electrolyte along electrochemical cycling. It also confirms the importance of in situ measurements for revealing the exact changes in this complex medium in the original chemical environment.

In order to estimate the thickness of the SEI, we measured the intensity of the negative-going infrared bands appearing during electrochemical cycling. As previously discussed, the negative absorbance values obtained by FTIR represent that the measured absorbance in a given wavenumber is less intense than the absorbance at the same wavenumber in the reference spectrum, revealing the decrease in the concentration of species having a given vibration mode averaged along the evanescent infrared probed region.

The infrared signals recorded in situ during electrochemical cycling exhibit negative peaks exactly coinciding with much more intense positive peaks of the electrolyte spectrum. This difference in intensity is due to the fact that in the entire probed region, only a small part was modified by the electrochemical processes in the in situ system. This modification is that corresponding to the balance between species created, excluded or modified by the formation of the SEI layer. The intensity of the electrolyte spectrum corresponds to

electrolyte absorption along a (know) probe depth, the change in intensity measured in the in situ spectrum corresponds to the electrolyte absorption across the (to be determined) SEI thickness. Therefore, by comparing the intensities of these two spectra one can deduce the SEI thickness from the quantity of electrolyte displaced/modified by the growth of the SEI layer. Of course, in view of the above discussion, this moving boundary approach which assimilates the SEI to a compact layer completely excluding the electrolyte from the interface with a-Si:H can only be considered as a rough approximation providing a schematic order of magnitude. Moreover, a closer look to the data reveals some variations from peak to peak in the relative intensity of the negative peak from the in-situ spectra to that of the positive peak of the electrolyte spectrum. Such a difference might be due to the fact that some chemical bonds are preferably modified during cycling, affecting their vibration modes (experimental incertitude could also possibly account for the discrepancy, as discussed later). This experimental observation is illustrated in Fig. 49, where the negative-going peaks obtained for hydrogenated a-Si:H after electrochemical cycle are compared with the respective peaks in the electrolyte spectrum. Labels of peaks represent the normalized values of intensity using as reference the most intense signal at 1277 cm^{-1} for 1M LiPF$_6$ in PC:EC:3DMC (2%VC, 10%FEC), and the signal at 1354 cm^{-1} for 1M LiClO$_4$ in PC. The electrolyte spectra at the top of Fig. 49 have their intensity values reduced in order to match the intensity of its reference vibration mode with the intensity of the same band in the in situ measured spectra. Such a reduction was obtained by multiplying the electrolyte spectrum by a matching factor (k_m), indicated in the figure. Additionally, the spectra of the reference electrolytes are artificially shifted to higher ordinates for allowing a clearer comparison to be performed with the a-Si:H electrode signals.
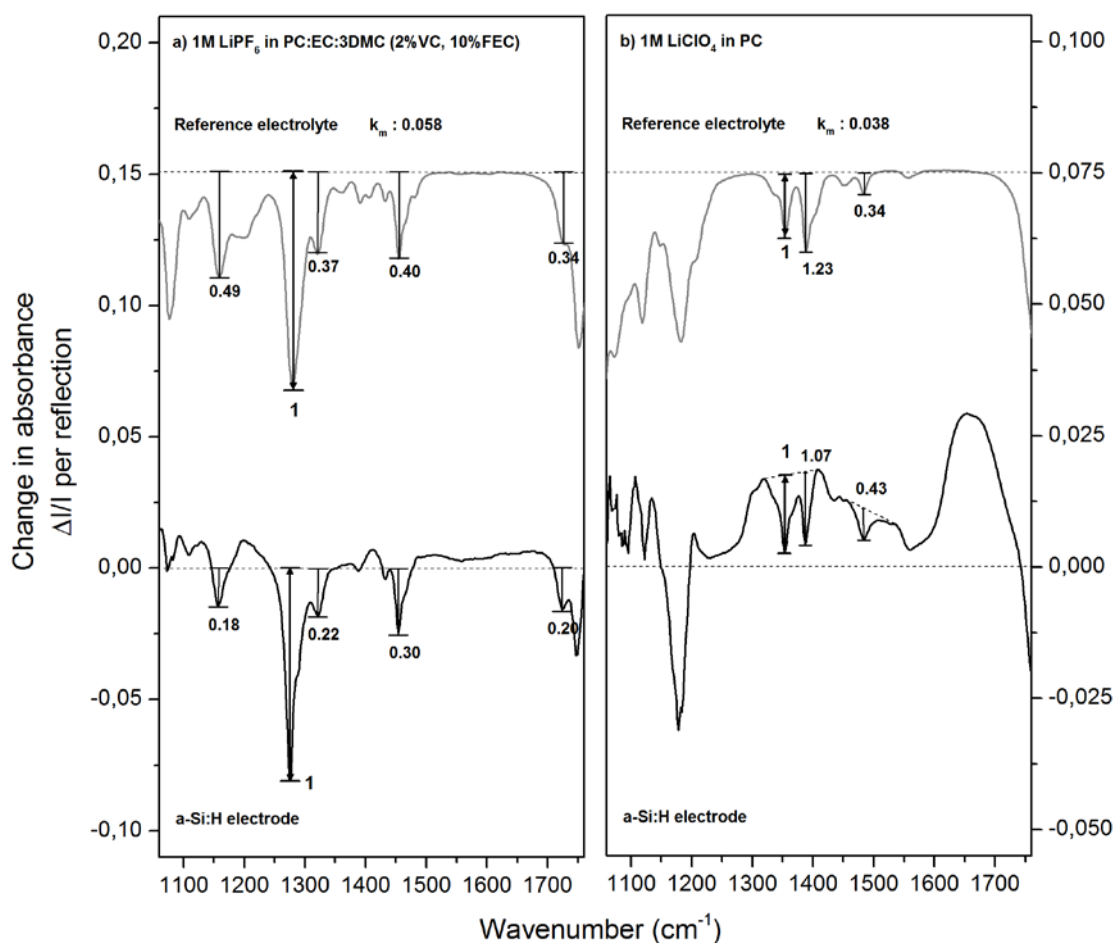
Fig. 49 – Intensity comparison of vibration modes between the reference electrolyte spectra (top) and the in situ obtained spectrum of a-Si:H electrode (bottom) after electrochemical cycle in different electrolytes.

The difference in the ratios of band intensity between cycled electrodes and the electrolyte demonstrate that the SEI thickness estimation can vary according to the vibration mode selected as reference and the reliability of the baseline correction. In order to minimize these sources of imprecision, the calculations were performed by selecting the most negative band observed in the spectrum, which also present a corresponding peak in the electrolyte spectrum. This choice is itself questionable, since the corresponding electrolyte absorption is so large that the transmitted signal is close to zero. It has been verified that selecting other peaks as the reference finally yield similar results within a 10% variation. Whatever this choice is, it is not possible to confirm whether the decrease in absorbance (resulting from the SEI growth) is also modified by overlapping with a positive-going signal, affecting the final intensity value. In this case, it is cautious to call the calculated SEI thickness as a *minimum SEI thickness estimation*, considering that the selected band can contains a positive contribution, which cannot be identified. Also, if the SEI is now regarded as a solid phase with a more or less open porosity, the thickness estimation actually relies in the volume of the solid phase per unit area, which means that the actual SEI layer will be again thicker than estimated.

Fig. 49 also illustrates the procedure used for estimating the amount of electrolyte displaced/modified by the growth of SEI layer. In the same way, all the spectra measured in this work were submitted to a similar procedure, which consists in rescaling the electrolyte spectrum in order to match the most negative band observed in the spectra obtained during electrochemical cycling. This scaling procedure directly allows for the *minimum SEI thickness* estimation. The scaling factor k_m resulting from this procedure is used as a coefficient for converting the penetration depth of the evanescent infrared wave into the thickness of the SEI.

However, for computing the penetration depth, the values of refractive index of the employed electrolytes are needed. The refractive index of fresh electrolytes was obtained by measuring the critical angle of total internal reflection in the visible. The values of refractive index in the range of near and middle infrared were obtained by the extrapolation of the measured values on the basis of Cauchy equation.[133],§ The obtained values of refractive index are presented in Table 4.

Table 4 – Refractive indexes of different electrolytes measured in the visible light range and extrapolated to infrared range.

	Wavelength (nm)	Wavenumber (cm^{-1})	Refraction index according to electrolyte composition		
			1M LiClO$_4$ in PC	1M LiPF$_6$ in PC:EC:3DMC	1M LiPF$_6$ in PC:EC:3DMC (2%VC, 10%FEC)
Measured	450	22222	1.429	1.395	1.395
	600	16666	1.422	1.388	1.389
	750	13333	1.419	1.386	1.385
Estimated	2500 - 11000	4000 - 910	1.413	1.381	1.380

The measured values of refractive indexes were found to be stable with time under atmospheric conditions. Moreover, due to the shape of Cauchy equation, the refractive index curve becomes practically flat for high wavelengths and the refractive index values estimated for the infrared range resulted in a single value in the whole region of interest.

Refractive index values can be directly used in equation 3.11 for calculating the penetration depth of the evanescent infrared wave at a given (totally reflection) interface.

$$d_P = \frac{\lambda}{2\pi(n_a{}^2 \sin^2\theta - n_b{}^2)^{1/2}} \qquad (3.11)$$

---

§ Cauchy equation: n(λ)= A+(B/ λ^2)+(C/ λ^4)+…

In this equation, d_p is the penetration depth from the silicon surface into the electrolyte, λ is the wavelength correspondent to the vibration mode of the analyzed band, θ is the angle of incidence of the infrared beam (45°), n_a and n_b are respectively the refractive index of the ATR crystal (3.418 for c-Si in the IR range)[134] and of the electrolyte, determined for the wavelength of the analyzed band.

The penetration depth was calculated for 1M LiClO$_4$ in PC using the estimated refractive index of 1.413 for the vibration mode at 1354 cm^{-1} (7385 nm), resulting in a value of 600 nm for d_p. Similar calculation was performed for 1M LiPF$_6$ in PC:EC:3DMC (2%VC, 10%FEC) according to the estimated refractive index of 1.380 for the vibration mode located at 1277 cm^{-1} (7831 nm), resulting in a value of 628 nm for d_p. SEI thickness (d_{SEI}) was estimated based on the relation between negative-going and electrolyte signals represented by k_m, and the depth of penetration of the infrared probe (d_p), according to Eq. 3.12:

$$d_{SEI} = d_p/2 \cdot k_m \qquad\qquad (3.12)$$

In this equation, the factor 2 comes from the fact that d_p is the probe depth associated with the infrared electric field, whereas infrared absorption is proportional to the square modulus of this field (the infrared intensity). Therefore, values of d_p represents twice the thickness of electrolyte probed by the infrared beam during the in situ experiment. It is important to recall that the peaks selected for determining k_m are located in regions of intense infrared absorption for both electrolytes, a source of uncertainty estimated by calculating k_m on the basis of different absorption bands, which results on uncertainty of ~10%. Fig. 50 shows the estimated values of SEI thickness along the first electrochemical cycle of a-Si:H based electrodes with different surface pretreatments in 1M LiClO$_4$ in PC and 1M LiPF$_6$ in PC:EC:3DMC (2%VC, 10%FEC). The points in the plots correspond to the values calculated from the negative-going FTIR bands in situ measured during electrochemical cycling as described by equation 3.12, and the line represents the Gaussian fit to the estimated results. Contrary to cycling curves presented up to now, capacity values are plotted continuously as exchanged capacity values. In spite of this choice, the limit between lithiation and delithiation can still be recognized and identified to the maximum of the Gaussian curve.

For both electrolytes, the estimation of the SEI thickness is found to vary according to the exchanged charge, increasing its thickness during lithiation and decreasing during delithiation. Maximum values of the SEI thickness are observed for the maximum values of lithiation in all the electrodes analyzed. However, even after such an impressive fluctuation

in size, the final thickness obtained after the first cycle demonstrate that this phenomenon is not completely reversible, as expected.
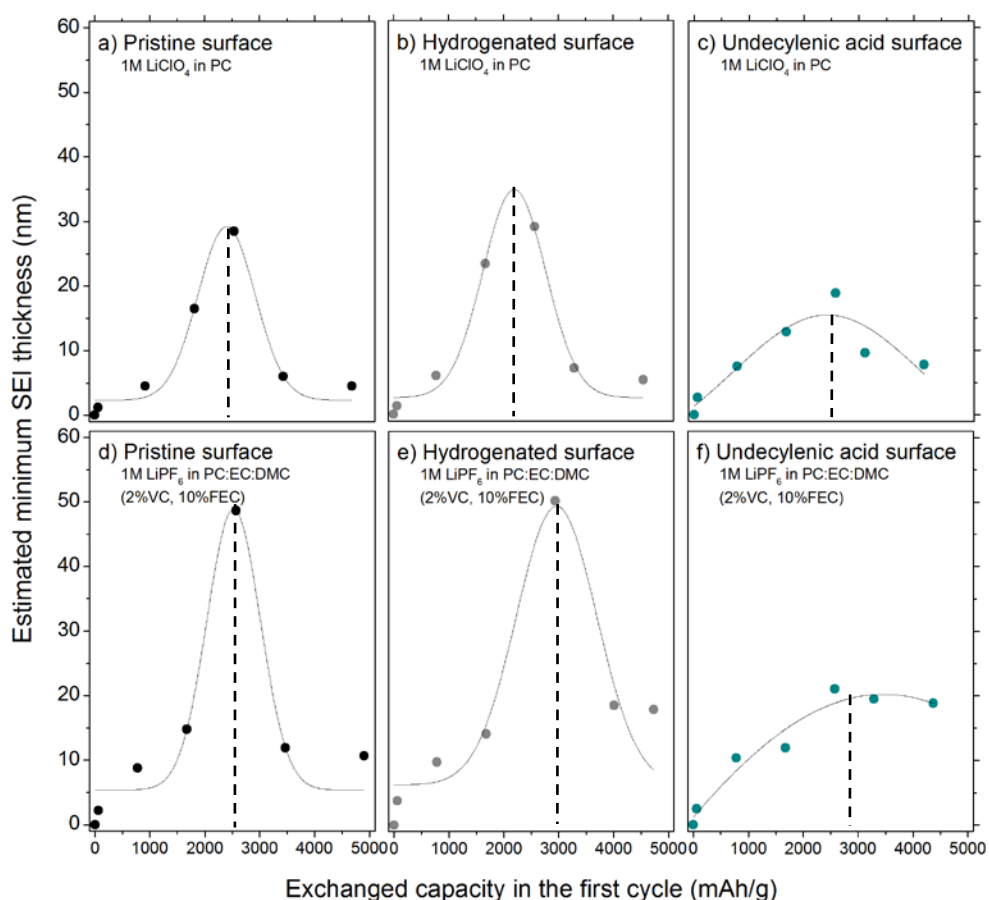
Fig. 50 – SEI thickness estimation during first electrochemical cycle in 1M LiClO$_4$ in PC (a-c) and in in 1M LiPF$_6$ in PC:EC:3DMC (2%VC, 10%FEC) (d-f). The dash line on the plots corresponds to the roughly to the limit between lithiation and delithiation

The comparison between the two different electrolytes used for in situ experiments is consistent with the effect of additives in promoting the formation of blocking SEI layers with enhanced effective thickness. At the end of the first cycle, the SEI thickness obtained in 1M LiClO$_4$ in PC was between 9 nm and 16 nm, depending on the surface pretreatment, while in 1M LiPF$_6$ in PC:EC:3DMC (2%VC, 10%FEC) the thickness was estimated between 21 nm and 38 nm.

Surface pretreatment plays an important role on the fluctuation and final values of SEI thickness, independently on the presence of electrolyte additives. It was observed that pristine surfaces result in thin SEI layers, while hydrogenated and grafted surfaces yield to enhanced thickness values. Acid functionalized surfaces have also a noticeable effect on the SEI variation by decreasing the maximum value of the fluctuation observed at high states of

lithiation. The barrier effect obtained by the grafting of undecylenic acid molecules on a-Si:H electrodes helps in stabilizing the growth of the SEI, leading to a final protection layer somewhat thicker.

Fig. 51 shows the evolution of the SEI thickness during several cycles. The points in the plot represent the estimated SEI thickness value at the delithiated state, at the end of the respective cycles. The guiding line plotted through the experimental points in the Fig. 51 was obtained by fitting the experimental points to Hill function.[**] The fast SEI growth observed during the first electrochemical cycle is quickly stabilized for grafted electrodes in both electrolytes. Electrodes cycled in 1M $LiPF_6$ in PC:EC:3DMC (2%VC, 10%FEC) developed thicker SEI layers than in 1M $LiClO_4$ in PC, as already evidenced for the first electrochemical cycle. The thickest SEI layer was estimated in 30 nm for hydrogenated a-Si:H in 1M $LiPF_6$ in PC:EC:3DMC (2%VC, 10%FEC) after ten cycles, while for grafted electrodes it was estimated to be 26 nm. For electrodes tested in 1M $LiClO_4$ in PC the thickest SEI layer was estimated to be 14 nm, while for grafted electrodes it was stabilized to 10 nm.
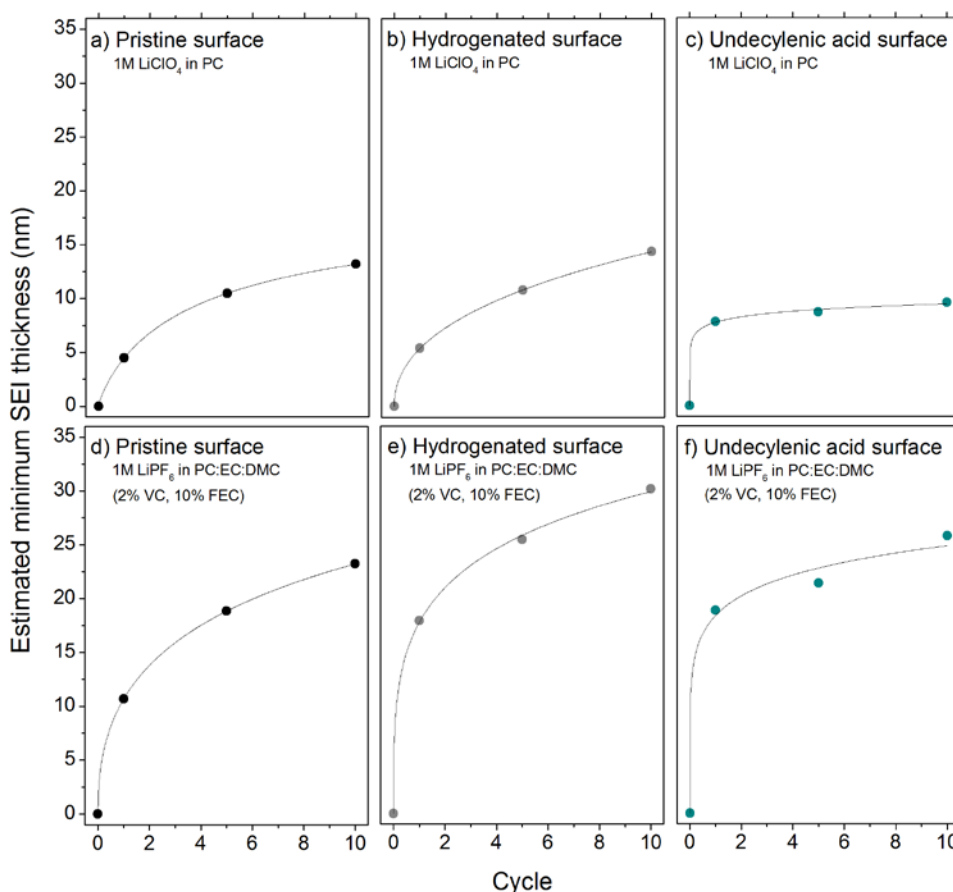

Fig. 51 – SEI thickness estimation during electrochemical cycling in 1M $LiClO_4$ in PC (a-c) and in 1M $LiPF_6$ in PC:EC:3DMC (2%VC, 10%FEC) (d-f).

[**] Hill function: $y = (y_{max} \cdot x^n) / (k^n + x^n)$

The fast SEI growth during the first cycle, and further stabilization, verified for acid-grafted electrodes in both electrolytes, can be correlated with the improved electrochemical performances of these electrodes treated with undecylenic acid. The SEI thickness formed on acid-grafted electrodes shows that the grafted molecules do not prevent the formation of the passivation layer which reaches thickness values similar to pristine electrodes after some cycles. However, the efficient formation of the SEI layer in the first cycle and the apparent stabilization with cycling suggests the production of a compact layer with enhanced passivation properties. It is believed that the undecylenic acid molecular layer participates on the SEI formation by efficiently offering anchoring points on the decomposition products of the electrolyte, helping in densely packing the SEI layer.

For the case of PC based electrolytes the analysis of the electrolyte displacement/consumption is more complex due to the overlapping of positive-going peaks related to the SEI formation, in particular for the case of pristine electrodes. Therefore, the last two points in Fig. 51a, corresponding to cycles 5 and 10, were fitted in a wider spectral window centered on the selected peak (1354 cm^{-1}), resulting in a less accurate estimation of the SEI thickness for these cases. The same procedure was used for fitting the last point in in Fig. 51c, corresponding to the tenth cycle of the grafted electrode.

Reconstructed SEI spectrum

The complex electrode processes in Li-ion batteries, in particular from the point of view of FTIR spectroscopy, led to us to look for a method for isolating SEI contribution in the in-situ infrared spectra. As shown hereafter, it yields the conclusion that the SEI layer is perceived as a layer formed by decomposition products from the electrolyte reduction, reactions with impurities, but also by the important presence of the electrolyte. The major role played by the electrolyte consists in ensuring the lithium supply, which can be particularly verified by the solvation effects observed by the in situ measurements during the electrochemical cycling. This demonstrates that the SEI layer is a dynamic evolution of the electrolyte components into decomposition products and high solvated species.

Spectroscopically, the difference between SEI formation and electrolyte displacement was until now simply discriminated by the intensity of the vibration modes, meaning negative or positive going bands. However, electrolyte modification leads to the formation of negative-going peaks with signal characteristics very similar to the pristine electrolyte signal, as previously demonstrated. The SEI layer formed on silicon surface can also contain species with similar vibration modes than the electrolyte, which results in the overlapping

between positive and negative-going signals during the SEI growth and electrolyte displacement. Fig. 52 illustrates the main contributions to the FTIR spectra in the electrochemical system here studied.
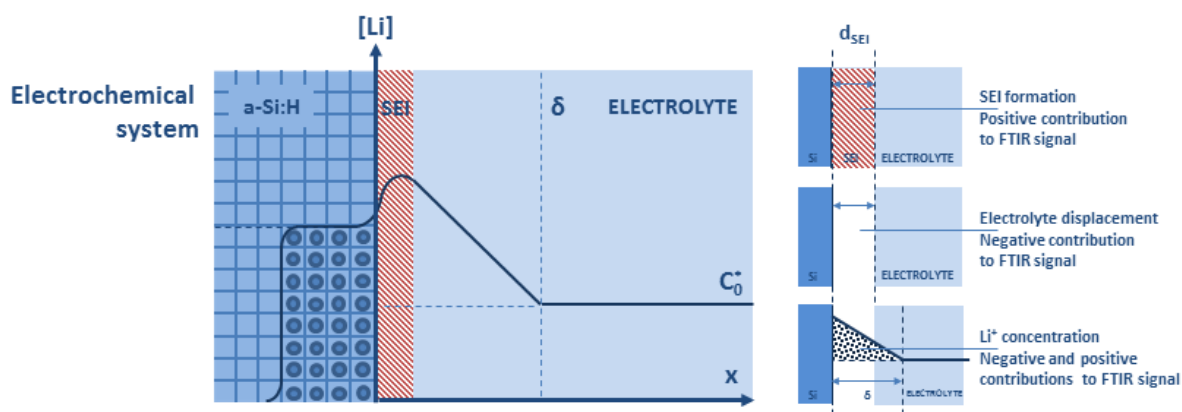

Fig. 52 – Illustration of the main phenomena affecting the FTIR signal in the in situ experiments.

The electrochemical system differs from the mass-transfer-controlled model by the increase in the lithium ion concentration in the vicinity of the electrode over the diffusion layer of thickness δ, as experimentally verified. The comparison between the pristine FTIR signal measured for a reference vibration mode in the electrolyte and the one obtained during the in situ measurements was used to define the scaling factor (k_m) and estimate the SEI layer thickness. Therefore, within this analysis multiplying the spectrum of the pristine electrolyte by k_m, yield the spectrum corresponding to the signal lost by the electrolyte displacement due to the SEI formation. Conversely, if the scaled electrolyte spectrum is added to the original experimental, in-situ spectrum, the resulting spectrum essentially represents the actual modification due to the presence of the SEI layer.

Therefore, this procedure identifies and removes from the in situ data the negative contributions due to electrolyte displacement, allowing for disclosing the SEI signal originally masked by the negative-going bands.

Fig. 53 shows the signal in situ obtained for silicon hydrogenated surface in 1M LiPF$_6$ in PC:EC:3DMC (2%VC, 10%FEC) during the first lithiation (a) and during successive cycles (b). The black lines represent the in situ spectra experimentally obtained and the green signals represent the reconstructed spectrum after applying the electrolyte correction. The reconstruction was calculated based on the compensation of the C-O-C asymmetric stretching vibration mode of DMC at 1277 cm^{-1}, gray mark in Fig. 53. This signal can be mainly affected by electrolyte displacement and ion solvation.
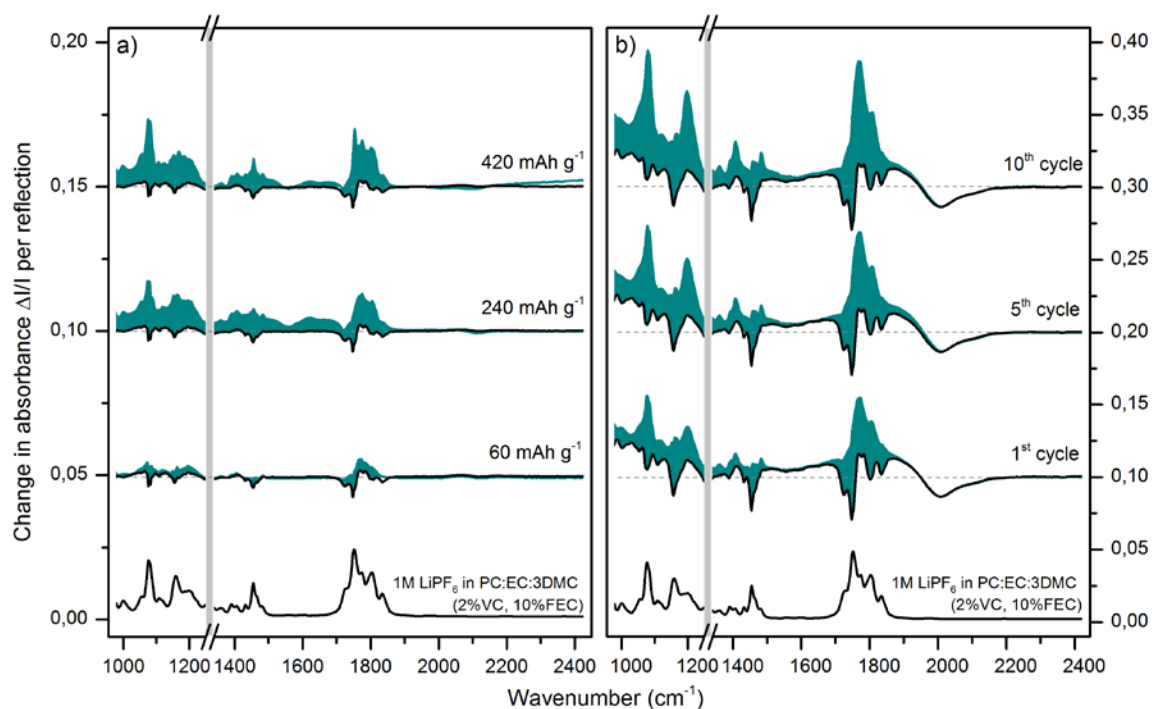
Fig. 53 – Reconstructed SEI spectra, after correcting for the electrolyte-displacement effects, calculated at several steps of the first lithiation (a) and along cycling life (b). Black lines are the measured spectra and the green areas represent the reconstructed spectra.

Comparing both reconstructed and pristine electrolyte spectra (black spectra at the bottom of Fig. 53) it comes that the SEI layer is composed of the combination of decomposition products, as previously assumed, and an important amount of the Li^+-solvating electrolyte. The SEI layer might also contain some amount of free (non solvating) electrolyte, but the correction method does not provide the possibility to distinguish it from the compensated electrolyte displacement contribution. The method also distinguish between the bulk and surface signals, as verified by the presence of a negative band at 2000 cm^{-1} related to Si-H bond consumption during electrochemical cycling in both original and reconstructed spectra.

Bulk lithiation

It was observed during the in situ experiments that the global absorbance in the entire spectral window was modified when the lithiation plateau was reached and the lithium concentration in the amorphous silicon thin layer increased. Such a modification corresponds to the increase of the absorbance signal varying almost linearly with wavenumber, resulting in a complete baseline shift. Interestingly, the phenomenon appears directly related to the amount of lithium inserted in the amorphous silicon layer since it is

completely reversible. Fig. 54 shows the baseline shift during the first electrochemical cycle of an amorphous silicon thin film based electrode, where the black spectra were obtained during lithiation and the green spectra during delithiation.
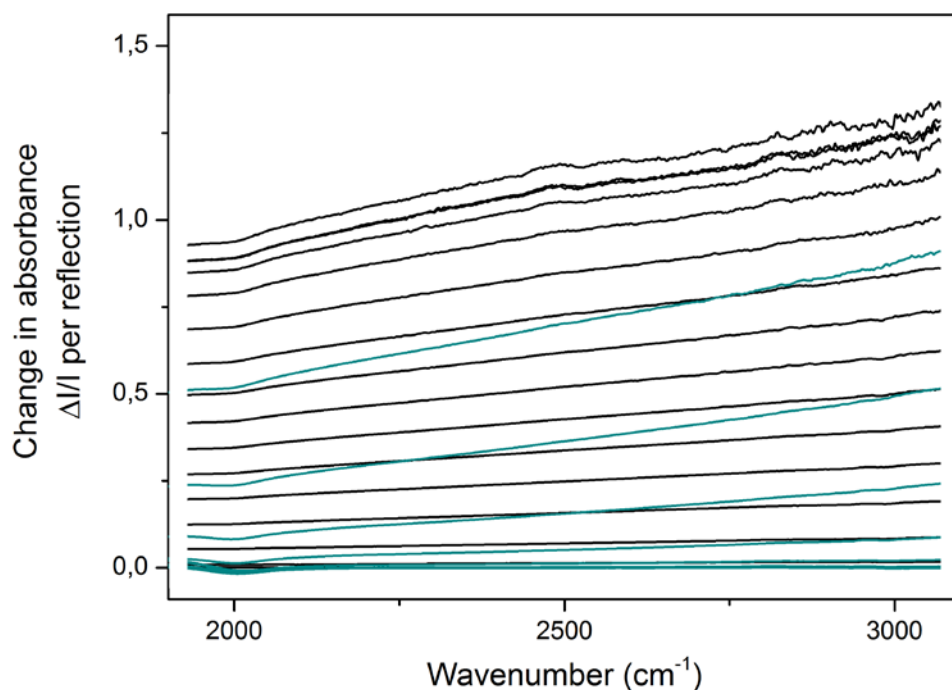
Notice that the change in the spectra reaches very intense values of absorbance and even the intense negative bands related to the loss of Si-H bonds centered at 2000 cm^{-1}, previously described in this chapter and shown in Fig. 42, becomes merely discernible at this absorbance scale. Additionally, at high level of lithiation, the lithiated layer becomes so absorbing that practically no infrared radiation is transmitted through the ATR prism, as apparent from the noisy spectral region at wavenumber above 2500 cm^{-1}.

Baseline shifts in FTIR spectra obtained during in situ experiments have rarely been observed and discussed in the literature. It appears associated with the original experimental cell design proposed in this work which allows for probing silicon lithiation at the same time as SEI formation. To our knowledge, no experimental work describes such phenomena. A certain similarity can be found with some results displayed in the reference 95 but on a different system – positive electrode – and a much lower amplitude.

The relationship between base line shift and lithiation of the silicon thin film was quantified by following the absorbance values at 2500 cm^{-1}, a very linear part of the apparent baseline. Fig. 55a illustrates the general increase in absorbance with the quantity

of lithium inserted into the amorphous silicon thin film for different electrochemical cycles in 1M LiClO$_4$ in PC. In parallel, Fig. 55b shows the lithiation and delithiation capacities obtained for this system from the electrochemical measurements, helping in verifying the relation between absorbance and state of lithiation.

We notice that the maximum absorbance value follows the cell capacity during cycling, even if the absorption value seems not to linearly scale with the capacity value. During the first cycle, the plot of the absorbance vs. capacity appears quite different during lithiation and delithiation, resulting in a curve exhibiting a large hysteresis. Such an effect is the result of two different contributions. The first one is related to the fact that during the first lithiation, the charging current is partially consumed for SEI formation and partially used for bulk lithiation. This low Faradaic efficiency for lithium alloying results in a stretching of the capacity scale, probably accounting (at least partially) for the large hysteresis. In the same way, but with opposite effect, the possible parasitic electrochemical reactions modifies the horizontal scale during delithiation. The second contribution, which is certainly the dominant one, will be discussed at the end of the present section.

Fig. 55 – FTIR absorption intensities at 2500 cm^{-1} (a) measured in situ during the electrochemical cycling of amorphous silicon thin film electrode in 1M LiClO$_4$ in PC; (b) lithiation/delithiation capacities simultaneously recorded during lithiation and delithiation, as function of the cycle number.

Fig. 56a shows the plot of absorbance vs. capacity for in situ spectra recorded for amorphous silicon electrochemical cycled in 1M LiPF$_6$ in PC:EC:3DMC (2%VC, 10%FEC). The

results demonstrate a strong loss of maximum absorbance value along the cycling life, which exactly corresponds to the electrochemical performance of the system, as shown in Fig. 56b. This confirms the fact that the increase in general absorption is related to bulk lithiation.
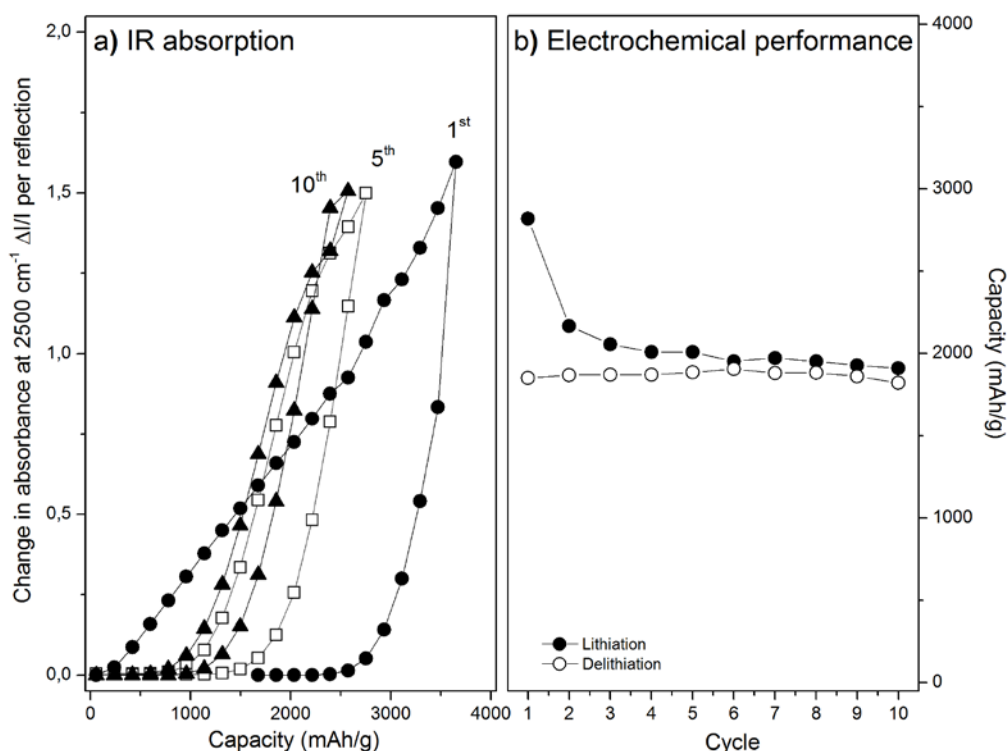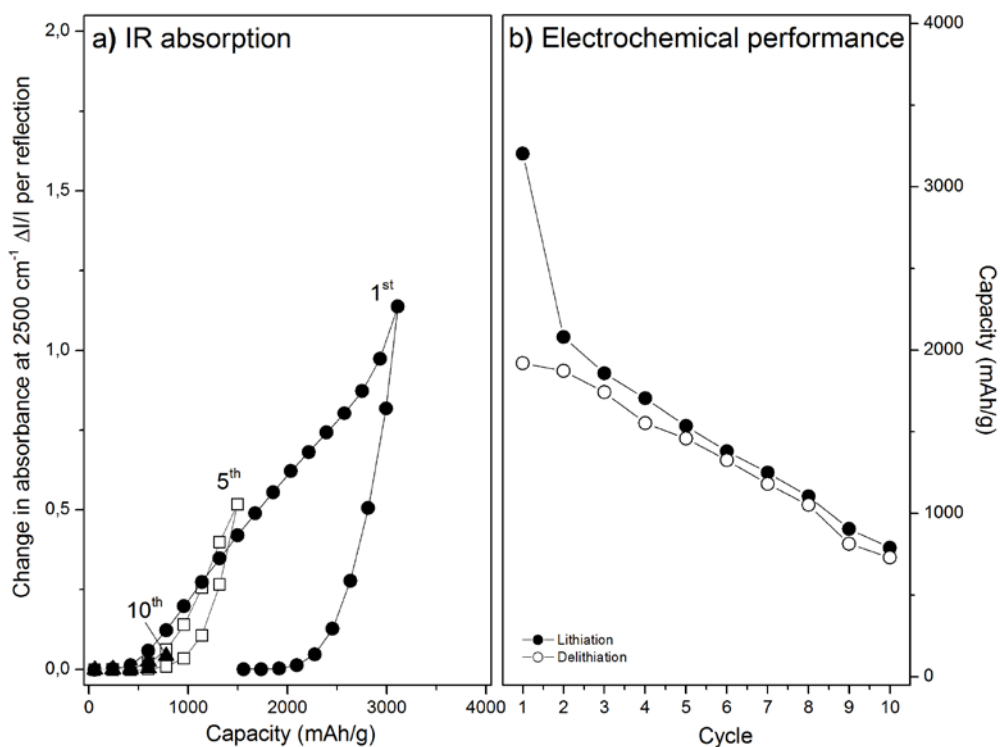

Fig. 56 – FTIR absorption intensities at 2500 cm^{-1} (a) measured in situ during the electrochemical cycling of amorphous silicon thin film electrode in 1M LiPF$_6$ in PC:EC:3DMC (2%VC, 10%FEC); (b) lithiation/delithiation capacities simultaneously recorded during lithiation and delithiation, as function of the cycle number.

The difference between the electrochemical performances of silicon in the different tested electrolytes indicates that the nature of the SEI layer plays an important role on the electrochemical processes. As compared to the layer formed in 1M LiClO$_4$ in PC, LiPF$_6$ based electrolyte is found to generate an homogeneous SEI with high blocking properties, observed by the efficient electrolyte displacement/consumption and the formation of negative-going infrared signals. Both passivation layers have similar growth rates on silicon electrodes, however according to Fig. 56b the LiPF$_6$ based electrolyte is found to deteriorate silicon lithiation capability upon cycling.

Absorbance variation during electrochemical cycling is clearly shown to be related to the lithium concentration in the amorphous silicon thin film electrode. The principle behind such a phenomenon is still not completely understood, however different possible origins can be considered. One of these possibilities would be that the geometrical changes (swelling) taking place during the electrode lithiation affect the number of total reflection in the ATR prism. This hypothesis can be excluded when considering the relative thickness of

the ATR crystal and of the active silicon layer where the truly geometrical modification takes place. For example, the predicted volume expansion of the amorphous silicon during lithiation would generate an infinitesimal increment on the total geometry without actually affecting the final FTIR measurement. Similarly, the enhancement of the optical path in silicon associated with a-Si:H swelling can be neglected as long as a-Si:H remains essentially transparent to infrared radiation.

The fact that silicon undergoes a large volume expansion under electrochemical cycling could make us believe that a series of structural defects are formed during this process generating optical losses along the pathway of the infrared beam. It is known that the fracture of silicon thin film electrodes starts during the delithiation process when the material recover its original volume and is submitted to tensile efforts.[135] The appearance of such fracture networks cannot be related to the effect under present consideration since it would lead to an effect opposite to the experimentally recorded (the general absorption increases during lithiation and decreases with delithiation). Moreover, it was verified that the electrochemical limits used for in situ experiments did not lead to crack formation.

Another possibility is the dispersion of the reflected infrared by surface or bulk defects on the electrode. Such bulk defects can origin from an inhomogeneous lithiation process of the silicon layer with the formation of zones of increased lithium concentration, resulting in the scattering of the infrared beam. Singular surface effects might be involved in the SEI. Though that this type of inhomogeneity is thermodynamically unfavorable, it could have taken place during electrode lithiation at high rate, especially knowing that lithium diffusion can be very sensitive to alloy composition and that minimal diffusion coefficients have been estimated for the case of pristine silicon.[136] However, it is believed that thin film silicon electrodes are lithiated in a very homogeneous way and in between a very narrow region (~1 nm) of phase transition between delithiated and lithiated phases.[25,137] Additionally, such phenomena will probably follow a fast increase of the general absorption, starting from the very beginning of the lithiation process, due to the generation of scattering sites on the surface of the ATR crystal, whereas (except for the first lithiation) the gradual increase in absorption recorded in our experiments takes place above a significant lithiation level of the a-SiH layer.

The changes in the electrolyte's refractive index could also lead to changes in the penetration depth of the evanescent wave, as previously mentioned. It is likely that the lithium consumption and electrolyte decomposition could affect the optical properties of the electrolyte during cycling. However, in this case, only a drastic modification in the refractive index could result in an effective change in the infrared absorbance. We estimate, for example, that the complete consumption of lithium ions from the electrolyte would result in a slight change of about 3 nm in the d_p. Moreover, in this case, a change in electrolyte absorption would be essentially observed rather a baseline shift.

In the infrared range, the refractive index of semiconductors can vary with doping level, injected carrier and impurities concentration.[138] Silicon refractive index can be modified during lithiation with consequences to its general absorption. Different electrochromic devices are designed based on the principle that lithium concentration can tune the complex refractive index of lithium intercalating materials.[139,140] In the present case, the alloying of lithium and silicon could generate extra absorption within the active layer (which is essentially transparent in the pristine state). The associated mechanism does not appear to be associated with free-carrier generation (though lithium could act as a donor impurity in silicon), which would yield a different spectral dependence. It appears more evocative of a transition involving localized state (like e.g., impurities in semiconductors), but in the absence of knowledge about the electronic structure of the lithium-silicon alloy formed in the process, it appears difficult to propose a reliable mechanism for such an extra absorption. However, the assignment of the infrared absorption to the formation of a highly lithiated phase appears the most plausible.

Whatever the actual mechanism is, it can be remarked that the two possible ones considered up to now (diffusion by inhomogeneities or lithiation-induced absorption in a-Si:H) are questioning the simple picture of an homogeneous lithiation, taking place by progression of a lithiated zone from the electrolyte side to the electrode one. If absorption is to ascribe to optical inhomogeneities, it would mean that the lithiated zone is spatially inhomogeneous. If absorption is due to the formation of a highly lithiated phase, the peculiar shape of the infrared absorption profiles as a function of the lithiation charge (Fig. 55a and Fig. 56a) have noticeable consequences in terms of lithium diffusion in the material. During the first lithiation the picture of a moving boundary between an outer heavily lithiated region and an inner, lithium-free material,[141] is consistent with the experimental profile: the heavily lithiated, infrared absorbing zone quickly formed at the surface widens upon current flowing, accounting for the essentially linear profile recorded during the first lithiation. In this picture, heavy surface lithiation starts almost as soon as the current is flowing (very small induction time before the inset of infrared absorption) and SEI formation takes place during most of the lithiation phase (profile slope about unchanged, e.g., as least from ~200 to ~2700 mAh g^{-1}), in agreement with the infrared characterization of the SEI. During subsequent lithiation/delithiation cycles, the increase in the infrared absorption upon lithiation is delayed and appears only after having passed a charge of ~1000 mAh g^{-1} (somewhat less in the LiPF$_6$ based electrolyte, see Fig. 56a). This fact suggests that the material has been modified by the first lithiation/delithiation cycle, and that now during the first stage of lithiation, the diffusion of Li ions in the active material is fast enough to prevent the formation of the heavily lithiated, infrared absorbing phase. This phase is formed only during a second phase (above ~1000 mAh g^{-1}), reaches a critical threshold. The picture of the moving boundary between lithiated and lithium free material, applicable to the first lithiation, does not appear to capture the actual physical processes for the subsequent lithiations.

3.4 – Conclusions

We have shown in this chapter the advantages of FTIR in situ measurements for characterizing the SEI layer formed on the surface of amorphous silicon based electrodes. The developed experimental setup allows for surveying different electrode processes taking place during the electrochemical cycling and probing the entire thin film active material and a ~300 nm region in the electrolyte, at the vicinity of the electrode surface.

In situ experiments based on silicon ATR crystal exhibit similar electrochemical performances to those obtained in standard electrochemical cells, validating the relevance of this in situ experimental setup. However, the use of germanium crystals did not offer satisfactory conditions for the electrochemical experiments.

It was observed that a barrier for lithium incorporation tends to be formed at the surface of amorphous silicon electrodes, showing that, at least in our experimental conditions, lithium alloying is under kinetic control. Based on in situ measurements, we could identify the increase in lithium concentration on the vicinity of the silicon electrode during lithiation and the partial reestablishment of the original concentration with delithiation. The SEI layer appears to trap part of the lithium ions in a solvated state during cycling, giving evidence for the important role played by the solvation properties of the electrolyte in the SEI layer and the singular possibility of identifying such phenomena offered by the in situ FTIR measurements. This is additionally evidenced by FTIR spectra which compensates the effects of electrolyte displacement by the SEI layer.

Some of the silicon surface modifications proposed in chapter 2 were in situ investigated in the present chapter. The results demonstrate that the silicon surface pretreatment affects the SEI formation, evolution and stabilization during cycling, as represented in Fig. 57. At hydrogenated silicon surface, a highly covering and uniform surface SEI layer is formed, which is, rich in LMC and other $ROCO_2Li$ compounds. The silicon grafting with undecylenic acid allows for impeding parasitic electrochemical reactions, resulting in a fast growth of the SEI layer. In this case, the SEI is first formed by a mixture of LMC and $ROCO_2Li$ with Li_2CO_3. However further electrochemical cycles convert the LMC species into the general form of $ROCO_2Li$. Additionally, SEI formed on grafted silicon surfaces presented decreased thickness fluctuation with cycling, in agreement with the assumed positive impact of the grafting for anchoring the SEI layer.
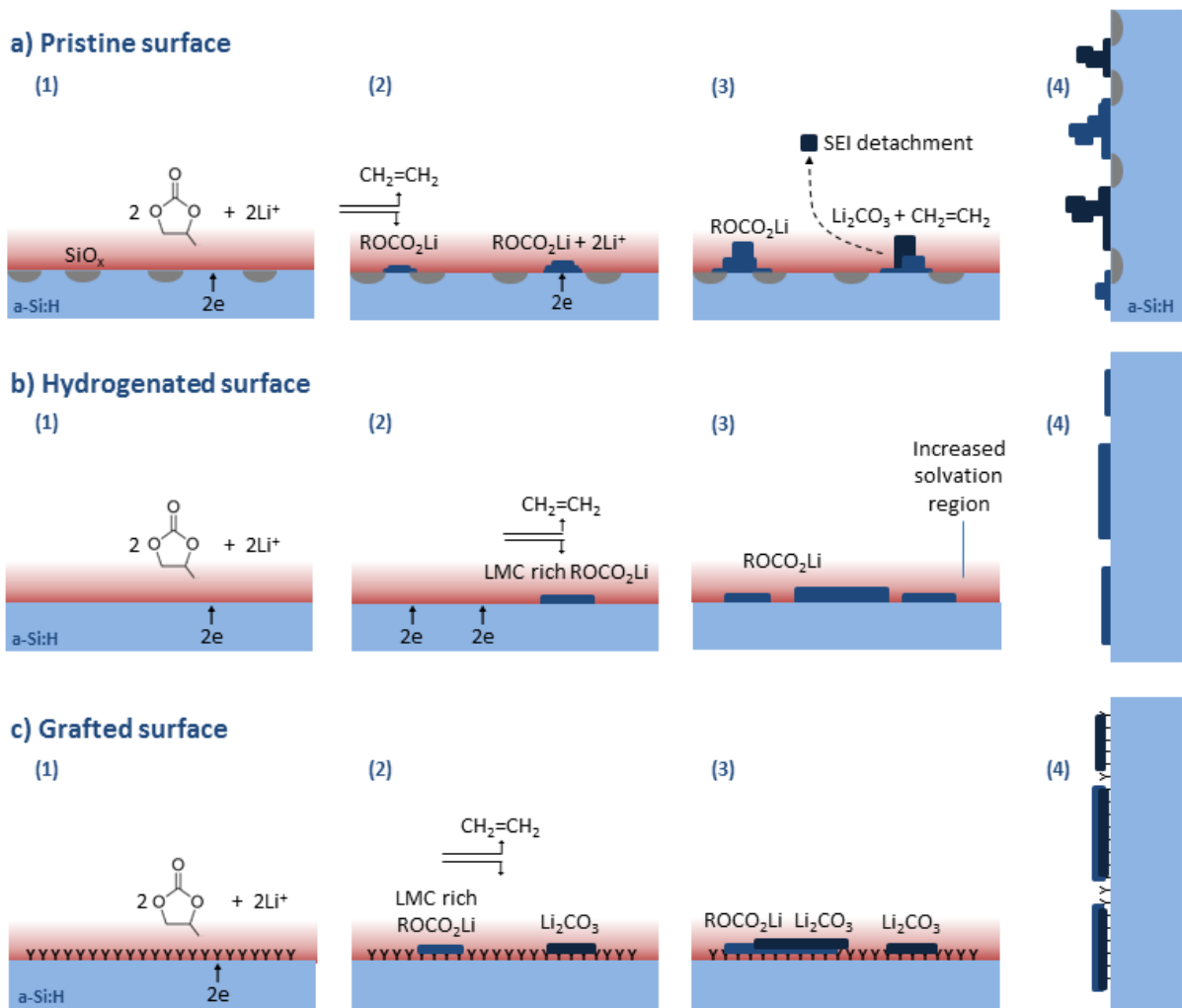
Fig. 57 – SEI evolution on amorphous silicon based electrodes according with different surface states.

The SEI layer plays an essential role on the electrochemical processes in Li-ion batteries, therefore different surface pretreatment can result in improved electrochemical performances. Fig. 58 presents the capacity values measured for amorphous silicon based electrodes with different surface chemical pretreatments measured using the in situ setup, where the improved performance of surface grafted materials appears for the two investigated electrolyte compositions, demonstrating the positive effect of undecylenic acid grafting on silicon electrodes (decrease in the irreversible capacity).

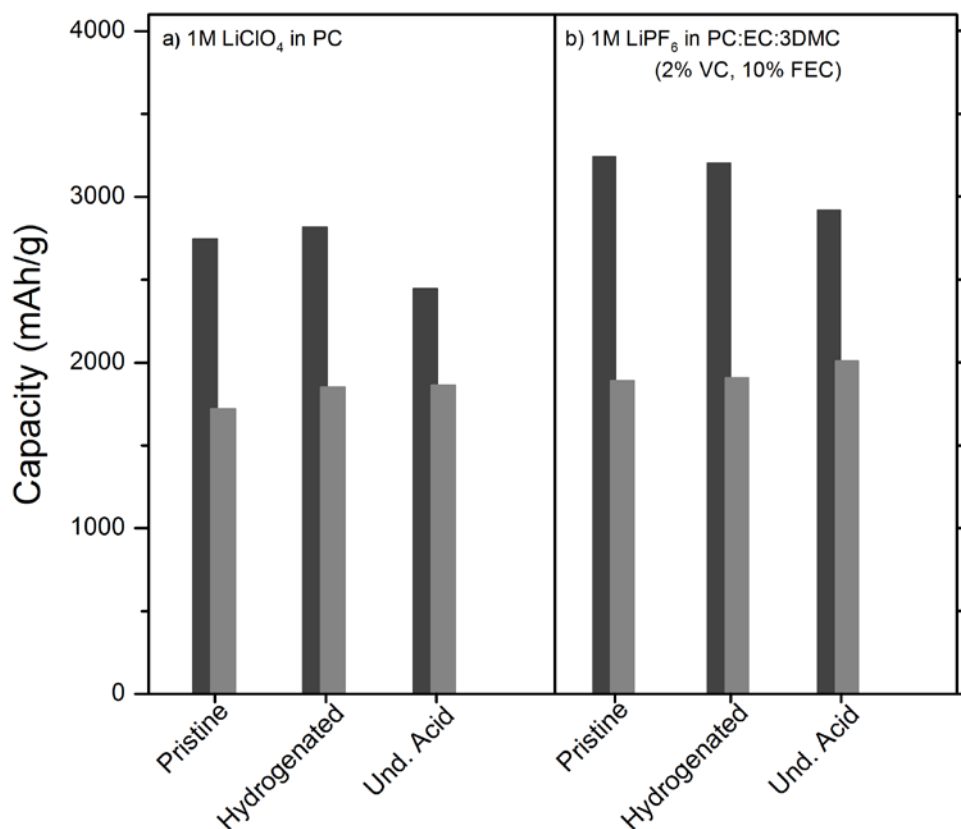In addition to all the surface phenomena revealed by the in situ FTIR experiments, two main effects of lithium insertion in amorphous silicon electrodes were observed. During the first silicon lithiation most of the silicon-hydrogen bonds present in the amorphous material are irreversibly broken. The FTIR technique is also able to distinguish between surface and bulk Si-H bonds; it reveals the consumption of surface Si-H species during the SEI formation and of bulk ones during silicon lithiation. Additionally, lithium concentration in the bulk material interestingly affects the infrared absorbance in the entire accessible special range, giving a direct evidence of the state of lithiation of the thin-film electrode and bringing experimental facts questioning the models of lithium incorporation in silicon.

Fig. 59 summarizes the general features of amorphous silicon based electrodes in situ observed during electrochemical cycling. It is shown that during electrode lithiation, the SEI formation is accompanied by the consumption of Si-H$_x$ surface species, followed by the consumption of bulk Si-H bonds upon silicon lithiation. During silicon delithiation an important part of the SEI layer is also consumed, except on acid-grafted electrodes in which the latter phenomenon is much reduced.

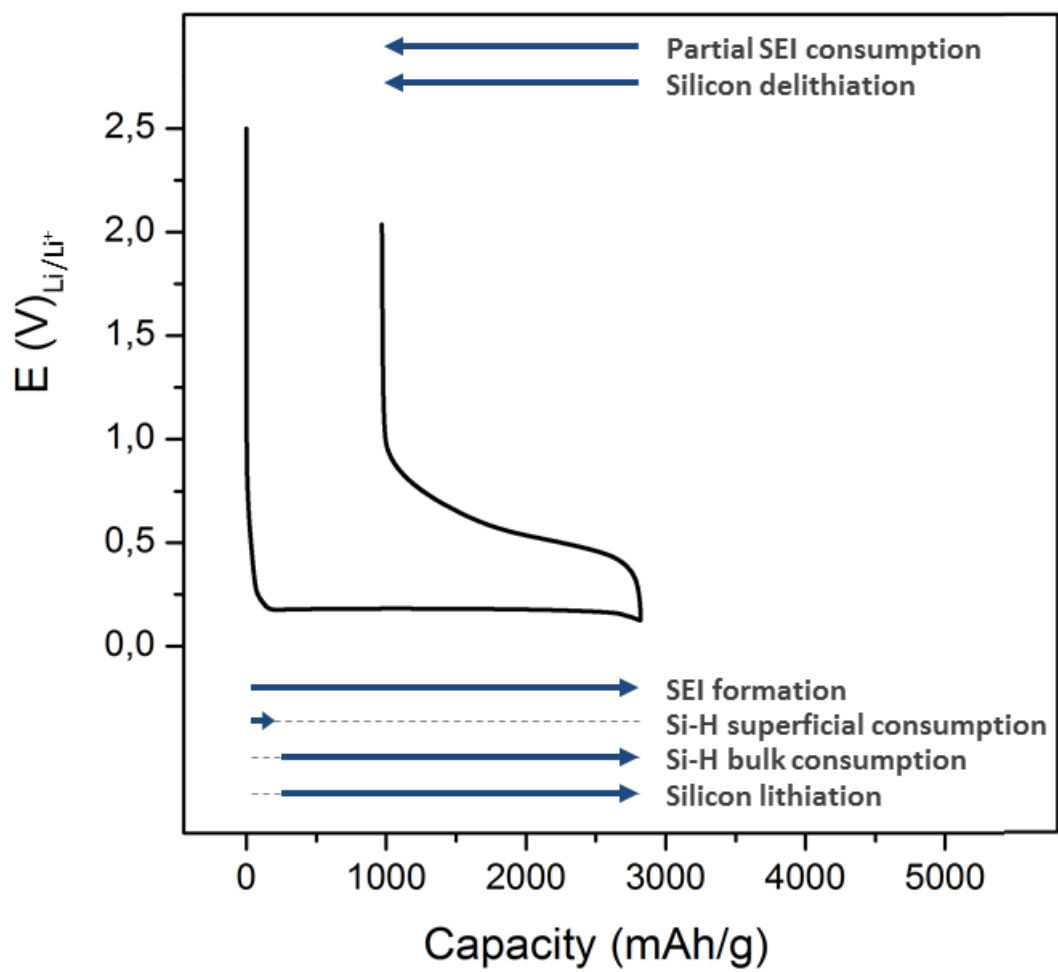**Fig. 59 – Main physicochemical processes in situ observed during electrochemical cycling.**

Chapter 4 | Amorphous silicon methylation and charge differentiation

Here we study the effects of the bulk chemical composition on the electrochemical performance of amorphous silicon electrodes. For this purpose, we suggest a method for differentiating between surface- and bulk-related irreversible charge consumption.

4 – BULK METHYLATED a-Si:H AND CHARGE DIFFERENTIATION

4.1 – Bulk methylated amorphous silicon – a:Si$_{0.9}$(CH$_3$)$_{0.1}$:H

Until now we have dedicated a great attention to surface based electrode processes, most of the time related to the formation of the solid electrolyte interphase. However, lithiation implicates a complete change in the structure of silicon electrodes, also giving place for bulk related phenomena, as noticed, for instance, at the end of the previous chapter.

The high Li/Si ratio and the intense volume expansion achieved during silicon lithiation results in a complete change of the pristine structure of silicon. This change in the active material can directly affect the electrode performance in different ways. The volume change can result in the detachment of part of the active material, losing its efficient electronic contact with the electrode and ending up isolated. Once part of the electrode material is detached, it does not only carries with it part of the reversible capacity but also expose a fresh surface which will consume some extra charge for being passivated. On the other hand, such an intensive structural change could also result in trapping of lithium into the silicon electrodes.[142,143,144]

Silicon undergoes continuous structural changes during the alloying process with lithium, which may lead to unfavorable energetic conditions for the delithiation of some atomic sites and result in the trapping of lithium atoms in the bulk material. Once trapped, these atoms do not contribute to the reversible capacity, representing a source of irreversibility of the electrode. Experimental evidence of this irreversible process can simply be obtained by changing the chemical composition of the active material, and then affecting the alloying/dealloying process, or by playing with the dimensions of the electrode active material, varying the amount of atoms trapped in the system.

In the last two chapters, we have put forward surface effects by changing the nature of the electrode surface, i.e., by using various chemical surface treatments prior to submitting the electrodes to lithiation/delithiation cycles. Similarly, we propose here to investigate possible bulk effects responsible for irreversible processes by changing the composition of the bulk active material.

For this purpose, PECVD technique allows for precisely tuning chemical composition and thickness of silicon thin film deposits. The chemical composition of the amorphous silicon electrode can be adjusted by changing the composition of the gas precursor mixture. It was previously described in chapter one that amorphous silicon thin film electrodes can be

obtained by the decomposition of silane gas under controlled conditions. Using a mixture of silane and methane, one can obtain the so called methylated amorphous silicon (a-Si$_{1-x}$(CH$_3$)$_x$:H).[21] For the deposition of a-Si$_{1-x}$(CH$_3$)$_x$:H layers, CH$_4$ is mixed to SiH$_4$ respecting a total flow of 2 L h^{-1} and pressure close to 40 mTorr. Under these conditions the deposition rate remains close to 3 nm s^{-1}, until decreasing for gas compositions over a value of [CH$_4$]/[CH$_4$]+[SiH$_4$] ~ 0.8.[21] We will first give details concerning the material characterization, then survey its properties as an electrode material in Li-ion systems.

Characterization and electrochemical performance

Incorporation of methyl groups in amorphous silicon deposits can be easily verified by FTIR analyses. As shown in Fig. 60, it is possible to incorporate methyl groups to the final deposit by keeping low the plasma power during the deposition. In this case, the carbon content in the material remains low (C/Si ratio lower than 0.4).[21] Methyl incorporation is evidenced by the presence of CH$_3$ stretching vibration modes at 2885 cm^{-1} and 2950 cm^{-1}, and deformation modes at 1235 cm^{-1} and 1400 cm^{-1} for deposits with a carbon content of 10% (spectrum on the top of Fig. 60). When the carbon content is increased, or the deposition is performed at high power regime, CH$_2$ is also incorporated to the amorphous layer. It is possible to identify in Fig. 60 the rising of CH$_2$ related vibration bands with the increase of carbon percentage or plasma power. CH$_2$ vibrational signature consists of the symmetric stretching vibration at 2860 cm^{-1} and asymmetric stretching vibration at 2920 cm^{-1}, and the scissoring vibration mode at 1450 cm^{-1}.[23]
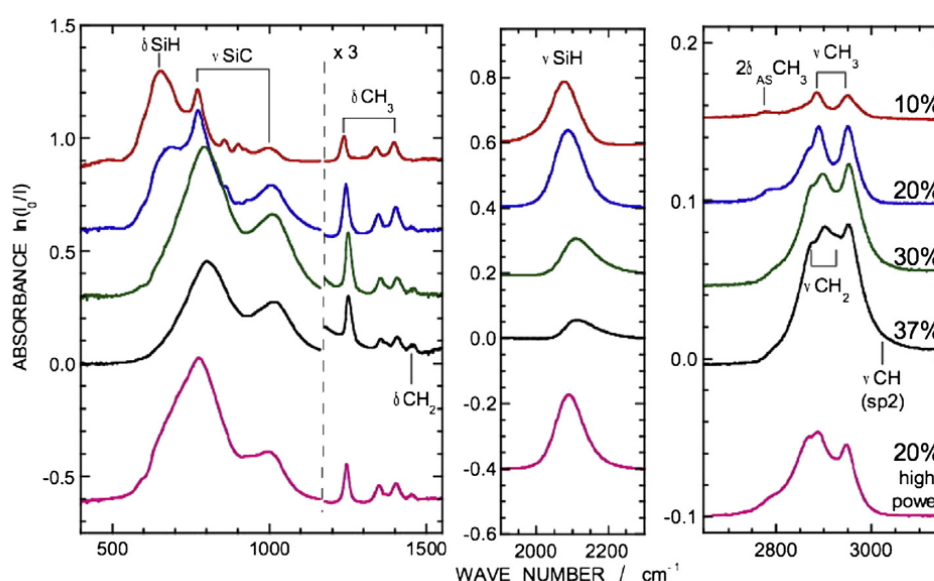

Fig. 60 –FTIR spectra of a-Si$_{1-x}$(CH$_3$)$_x$:H deposits containing different carbon loads deposited at low or high power and measured in the transmission mode.

Methylated amorphous silicon was also electrochemically tested in a standard electrochemical cell, as described for pure a-Si:H in chapter one. In this case, a-Si$_{0.9}$(CH$_3$)$_{0.1}$:H electrodes were prepared by depositing 100 nm thick films on stainless steel substrates. Cyclic voltammetry (CV) tests were performed in 1M LiClO$_4$ in PC using a lithium foil as counter-electrode. The potential was scanned at 0.5 mV s^{-1} starting from open circuit potential until 0.1 V vs. Li/Li$^+$. As shown in Fig. 61, methylated amorphous silicon reveals a differentiated electrochemical behavior when compared to pure a-Si:H electrodes. All the signals of parasite reactions and electrolyte decomposition observed in the range of 0.5-1.5 V vs. Li/Li$^+$ for a-Si:H seem to be vanished from the methylated system, resulting in a very flat electrochemical signal from OCV (~2.5 V vs. Li/Li$^+$) until the lithiation potential.
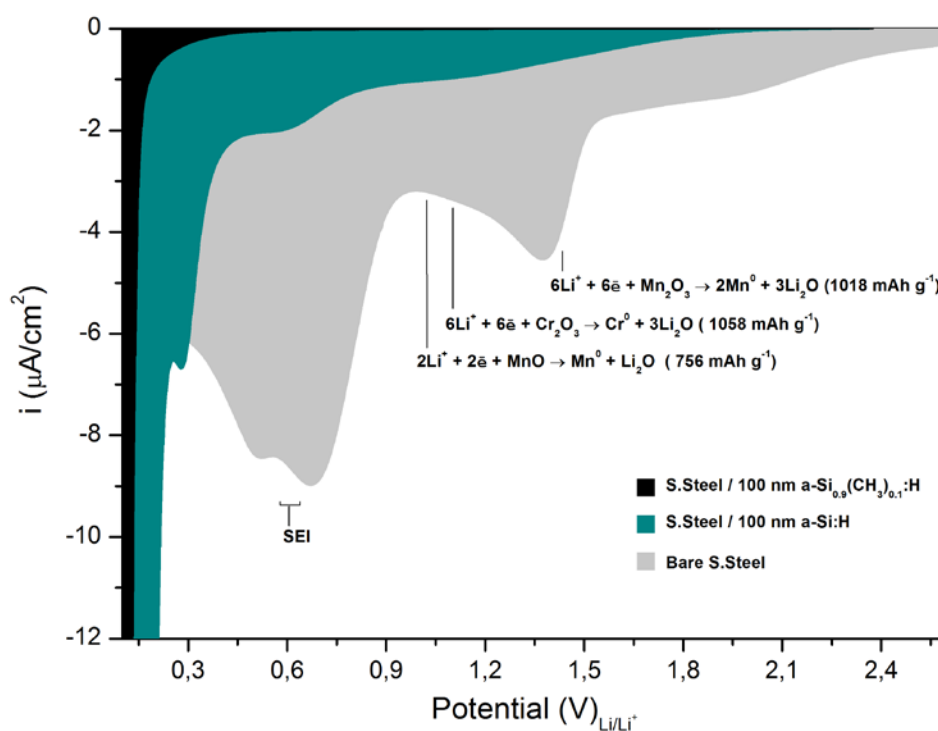
Fig. 61 – Cyclic voltammetry of a-Si$_{1-x}$(CH$_3$)$_X$:H thin film electrodes compared to a-Si:H and bare stainless steel electrodes.

Besides this voltammetric characterization, methylated amorphous silicon electrodes were also tested by the GCPL technique with charging/discharging rate of C/10 and within the potential limits of 0.1 and 2.0 V vs. Li/Li$^+$. The resulting curve is shown in Fig. 62, where it is compared with pristine and hydrogenated surface a-Si:H electrodes. Electrochemical tests indicate an improved performance of bulk methylated amorphous silicon, evidenced mainly by the large decrease in lithiation capacity, by 1280 mAh g^{-1} between pristine and methylated. However, the shape of the plot is also affected by the carbon addition, resulting

in the change of the lithiation plateau into a sloppy profile and decreasing the electrolyte decomposition at high potential values.
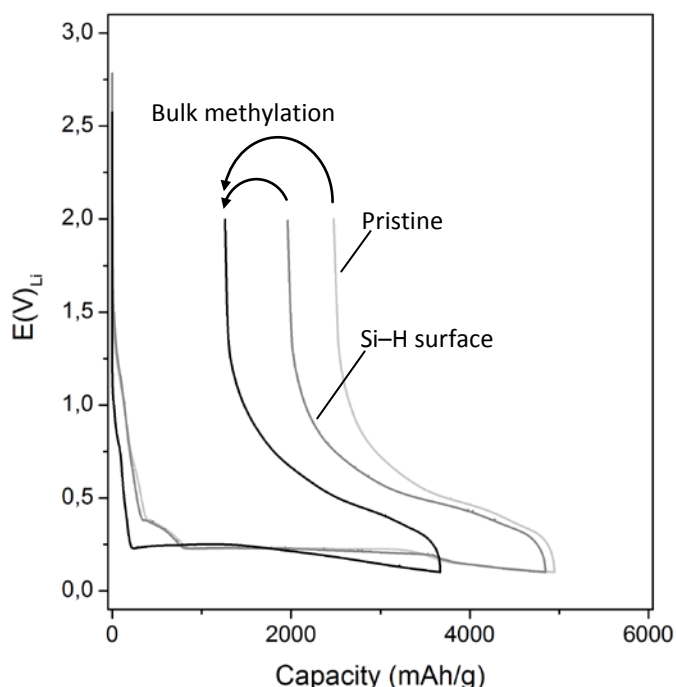
It could have been expected that the a-Si$_{0.9}$(CH$_3$)$_{0.1}$:H material presents a lithiation capacity value decreased by 10% due to the inert carbon content in the material. However, though the apparent lithiation capacity is decreased by 25% for methylated electrodes as compared to pristine ones, the value obtained for delithiation capacity remains almost the same as that of the pristine electrode (which is actually due to a slight change in the volume density of the material). Once compared with the pristine a-Si:H electrode, the bulk methylation results in an irreversible charge capacity decrease by 1220 mAh g^{-1}, coulombic efficiency increase by 16% and an irreversible capacity, given as a percentage of the reversible capacity decreased by 48%. Even when comparing to surface hydrogenated electrodes, methylated electrodes present an increase in the reversible capacity by about 480 mAh g^{-1}, a decrease in the irreversible capacity by 700 mAh g^{-1}, resulting in a coulombic efficiency of 65%.

Such results give evidence that methylated amorphous silicon have enhanced properties not only related to the cycle life, as already claimed,[23] but also to the charge losses due to secondary electrochemical reactions.

In situ FTIR of methylated amorphous silicon

As this stage, it is not quite clear whether the significantly improved electrochemical performance of methylated amorphous silicon electrodes are due to change in the bulk material composition or change in the surface properties. This question motivated in situ monitoring of the SEI formation by FTIR on a-Si$_{0.9}$(CH$_3$)$_{0.1}$:H electrodes. In this case, a-Si$_{0.9}$(CH$_3$)$_{0.1}$:H layers were deposited on the surface of ATR prisms for coupled electrochemical-FTIR experiments.

Fig. 63 shows the in situ FTIR spectra of electrochemically cycled a-Si$_{0.9}$(CH$_3$)$_{0.1}$:H based electrodes after different cycles, where most of the identified bands were also observed for experiments performed on a-Si:H. The spectra have been computed using as reference the spectrum recorded on the freshly assembled electrochemical system at OCP before the first cycle. The SEI composition of silicon electrodes does not seem to be much affected by its carbon content. These similarities also include the shifts due to free/Li$^+$-solvating solvent signals which follow the same behavior as that previously observed for pure a-Si:H electrodes. However the amount of the products of electrolyte decomposition is highly increased in the case of methylated silicon electrodes.

A close look to the intensities of the different SEI components reveals that the ratio between the two main species (ROCO$_2$Li and Li$_2$CO$_3$) is affected by the carbon presence in the electrode material. Methylated amorphous silicon exhibits a ROCO$_2$Li content higher than a-Si:H, stressing the importance of the role played by electrode material composition in the final SEI composition. Additionally, the SEI layer formed on a-Si$_{0.9}$(CH$_3$)$_{0.1}$:H based electrodes appears to be homogeneous and with good covering efficiency, as evidenced by the negative-going bands in the FTIR spectra which are caused by the electrolyte displacement.

The analysis of the chemical species present on the SEI layer along the electrochemical cycling reveals an intensive formation of ROCO$_2$Li rich layer during first cycle. This layer is particularly rich in methoxy terminated compounds, as shown in Fig. 63b. However, upon further cycling, this initial layer composition is modified and part of the methoxy terminated compounds are consumed for forming longer chains. This SEI modification is revealed by the decrease in the intensity of methoxy related band in the 2750-2881 cm^{-1} region (Fig. 63b) and the simultaneous rise of signals in the 1380-1550 cm^{-1} region (Fig. 63a), typically related to the stretching vibration modes of O-C-O compounds.[111]
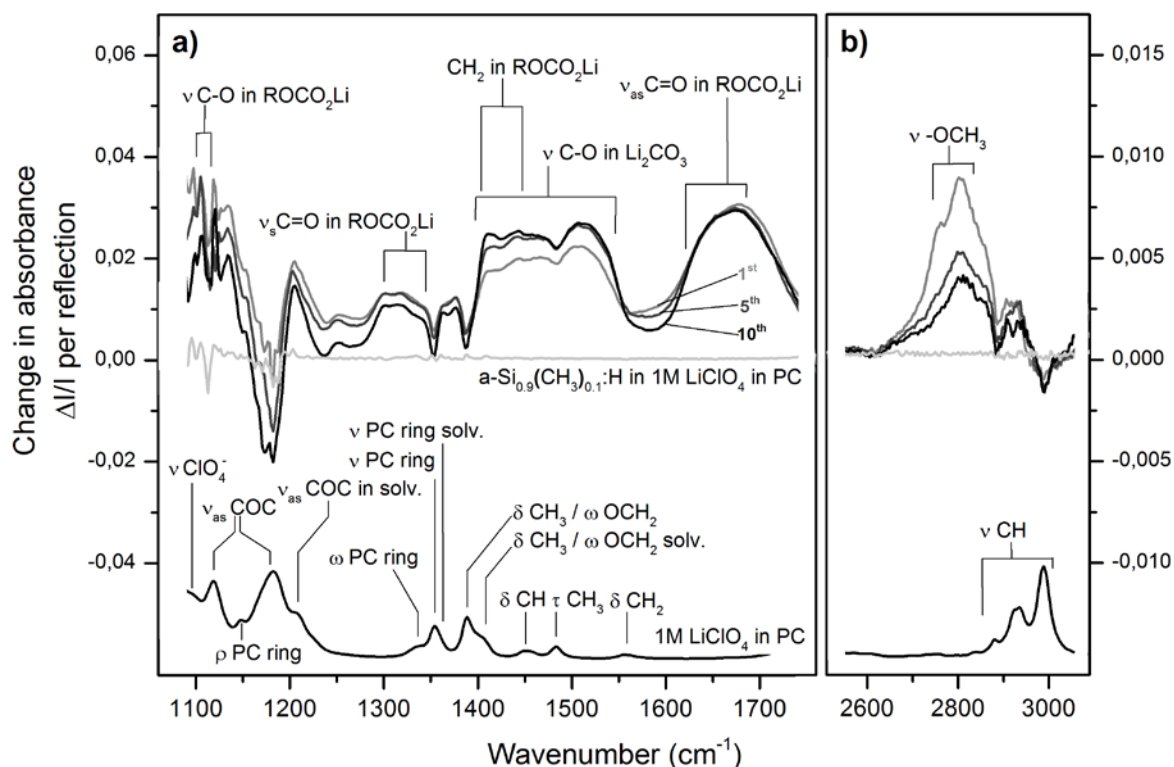
Fig. 63 – ATR-FTIR spectra of a-Si$_{0.9}$(CH$_3$)$_{0.1}$:H obtained in situ along cycling (top) and the spectrum of the electrolyte (1M LiClO$_4$ in PC).

Besides the mentioned somewhat different chemical composition as compared to a-Si:H, the thickness of the SEI layer formed on methylated silicon is found to remain practically unchanged along cycling. The amount of the SEI compounds formed in the first electrochemical cycle stay practically stable along further cycles, as shown by the C=O vibration modes in ROCO$_2$Li in Fig. 63a. Moreover, the inferred thickness of the SEI layer, estimated from the negative-going signals in the spectra, remains almost the same as that reached in the first cycle, attesting for the layer stability. This stability is also reinforced by the fact that the changes in the FTIR spectra occur in a progressive way and not irregularly as for the unstable pristine electrode. Concerning the quenching of parasitic electrochemical reactions, when plotting SEI thickness derived from electrolyte negative peaks as function of the irreversible capacity, the methylated silicon also exhibits a slightly better efficiency as compared to grafted silicon, similarly resulting in a fast SEI growth.

4.2 – Irreversible charge differentiation

The in-situ infrared experiments undoubtedly establish that the SEI layer on a-Si$_{0.9}$(CH$_3$)$_{0.1}$:H electrodes does not behave exactly as that on a-Si:H. These differences in surface properties might contribute to the differentiated electrochemical performance observed for bulk methylated amorphous silicon.

The in situ FTIR experiments in methylated silicon indicate an intense electrolyte decomposition, which seems to be achieved with superior electrochemical efficiency, improving the electrode performance. Additionally, the absence of signals in the cyclic voltammetry tests indicates that the charge consumption at typical potentials of electrolyte decomposition is minimum. This suggests that surface processes dependent on the bulk composition play an important role on the irreversible charge of methylated silicon electrodes.

Clearly, the carbon addition into the amorphous silicon (as CH$_3$ groups) has consequences in the amount of irreversible charge consumed during the first electrochemical cycle. But it remains unclear at this stage that only surface electrode modifications have an impact in the charge irreversibly consumed by electrode processes. Therefore, it is crucial to be able to distinguish whether the change in the electrode characteristics affect the charge consumed by the surface (SEI formation) or by bulk (Li trapping) related processes. Additionally, identifying the value of charge specifically consumed by surface reactions or bulk processes could allow us to estimate the limit of improvement that can be hypothetically achieved by surface treatment.

Analytical method

In order to differentiate between surface or bulk related charge consumption during electrochemical cycle an analytical method was developed, based on the easy control of film thickness provided by the PECVD technique.

The irreversible capacity of an electrochemical energy storage system is described by the difference between lithiation and delithiation capacities (Eq. 4.1). This irreversible capacity can also be expressed in terms of surface (here called Q$_{SEI}$) and bulk (Q$_{BULK}$) related contributions, as described by Eq. 4.1-3 describe.

$$Q_{IRR} = Q_{LITHIATION} - Q_{DELITHIATION} \qquad (4.1)$$

$$Q_{IRR} = Q_{SEI} + Q_{BULK} \qquad (4.2)$$

$$Q_{IRR} = Q_{SEI} + \alpha_{BULK} \cdot d \qquad (4.3)$$

Surface contribution varies with the area of the electrode while the bulk contribution varies as a function of the mass of the active material, which, at constant surface area of the electrode, scales like thickness of the amorphous silicon deposit (d). As described by Eq. 3, one can determine the Q_{BULK} contribution to the total Q_{IRR} by performing experiments at constant surface area of electrode and various electrode thicknesses. Moreover, Q_{SEI} and α_{BULK} are determined by linear extrapolation of the Q_{IRR} values as function of electrode thickness, as sketched on Fig. 64. In the limit where bulk irreversible processes are only related to Li trapping in the active material, the corresponding residual lithium bulk concentration in Atoms cm^{-3} is then derived from α_{BULK} by:

$$[Li]_{BULK} = (3600 \cdot \alpha_{BULK} \cdot N_A) / F \qquad (4.4)$$

In Eq. 4.4 α_{BULK} is given in Ah cm^{-3}, N_A is the Avogadro number ($6.022 \cdot 10^{23}$) and F is the Faraday constant (96485 C mol^{-1}).

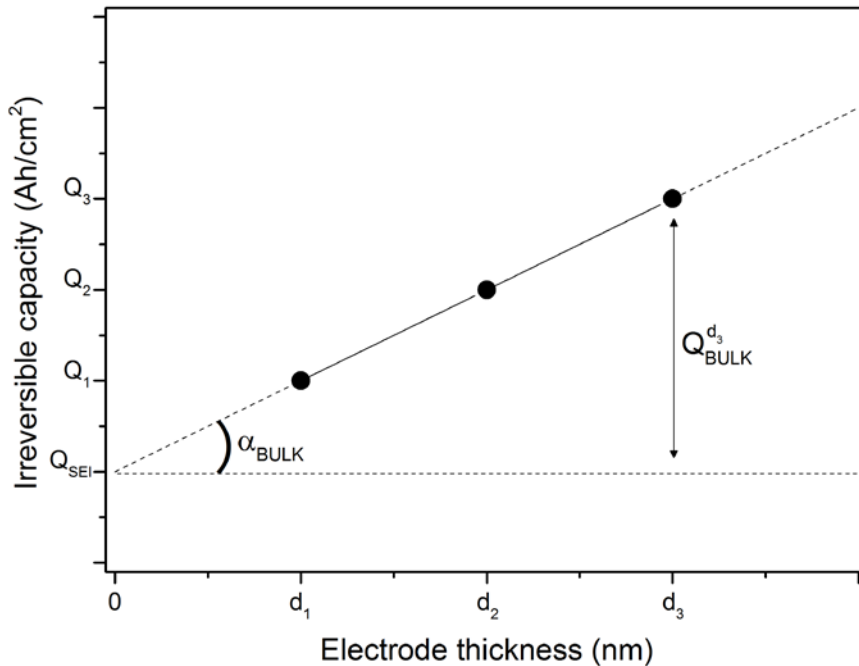Fig. 64 – Schematic example of the irreversible capacity dependence as a function of the thickness of the active-material layer.

Based on the above described method, different electrodes were tested: bulk methylated amorphous silicon, pristine, hydrogenated and acid grafted a-Si:H electrodes. The electrochemical tests were performed on electrodes with thickness varying from 30 nm to 200 nm, deposited on stainless steel substrates. The electrochemical tests (GCPL) were performed in a standard electrochemical as previously described in chapter 1. As shown in Fig. 65, the irreversible capacity increases with the thickness of the silicon deposit indicating the bulk contribution to the charge consumption during the first electrochemical cycle. The average experimental incertitude is estimated to be about ±1.5 µAh cm^{-2}.
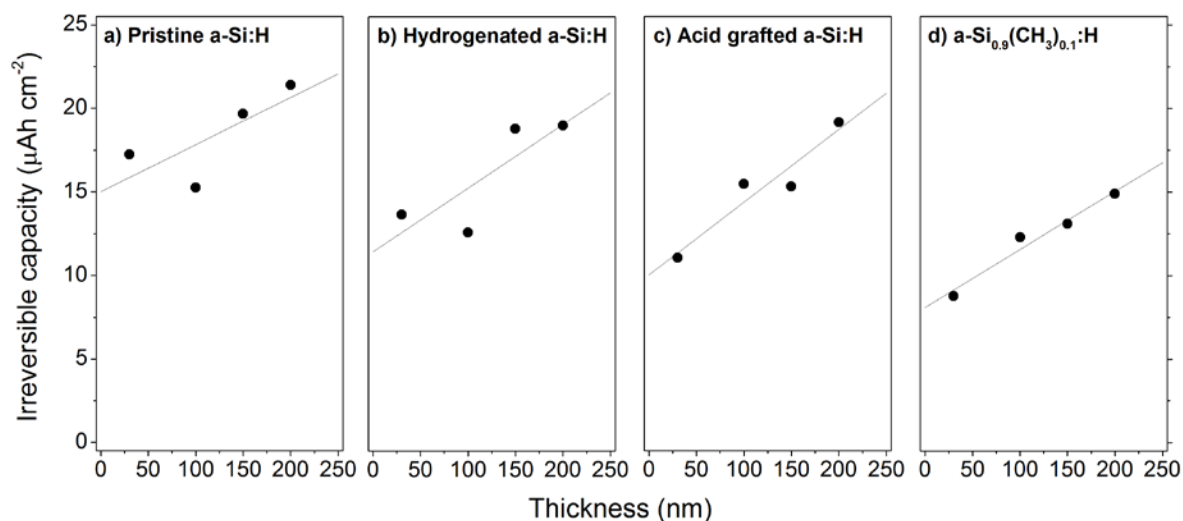
Fig. 65 – Irreversible capacity dependence as a function of a-Si:H with different surface treatments: pristine (a), hydrogenated (b), and acid grafted (c). And bulk methylated a-Si$_{0.9}$(CH$_3$)$_{0.1}$ (d).

According to Fig. 65, α_{BULK} does not depend much on the electrodes composition, whereas Q_{SEI} is much affected by surface preparation on electrode composition. Therefore, the effect on the irreversible capacity appears to be more strongly related to surface phenomena than to bulk processes. Surface hydrogenation, surface grafting or bulk methylation resulted in the displacement of the Q_{IRR} vs. d curve to lower values compared to pristine electrode. The slopes of the Q_{IRR} vs. d curves seems not to vary with the electrode modifications tested here. They provide the value of charge consumed by bulk related processes, which can be converted in terms of concentration of lithium atoms trapped in the thin film deposit using Eq. 4.4.

Table 5 shows the values of irreversible charge consumed by surface related reactions (Q_{SEI}) and by bulk processes ([Li]). The calculated values clearly demonstrate the

effect of surface hydrogenation and bulk methylation on the charge used for electrode surface reactions. Here again, the efficiency of methylated amorphous silicon in promoting the SEI formation with reduced charge loss is observed. The values of charge consumed due to surface phenomena calculated here are smaller but in agreement with values obtained elsewhere for a-Si thin films prepared by RF-magnetron sputtering.[145] However, in our case we distinguish between bulk and surface related irreversibility which gives deeper insight into the relevant physicochemical processes.

Table 5 – Charge information derived from the analytical charge differentiation.

Bulk composition	Surface condition	Q_{SEI} ($\mu Ah\ cm^{-2}$)	$[Li]_{BULK}$ (At. cm^{-3})
a-Si:H	Pristine	15.0	6.3×10^{21}
a-Si:H	Hydrogenated	11.4	8.5×10^{21}
a-Si:H	Acid grafted	10.0	9.7×10^{21}
a-Si$_{0.9}$(CH$_3$)$_{0.1}$:H	Hydrogenated	8.1	7.8×10^{21}

The values of charge consumed by bulk related process, represented by concentration of lithium trapped on the bulk material, shows that the bulk methylation has a minor effect on such phenomenon. The calculated value of lithium concentration in amorphous silicon electrodes (8×10^{21} At. cm^{-3}) corresponds to a value of ~15% of the silicon atomic density in the material. Such a value exceeds practical values used for doping in crystalline silicon and even in amorphous silicon, owing to the low electrical activity of dopants in the amorphous material. This residual lithium concentration corresponds to an irreversible charge of about 45 mAh cm^{-3}. An important amount of remaining lithium atoms was also identified elsewhere by Tof-SIMS depth profiles in a-Si:H after the first electrochemical cycle, confirming the lithium trapping on the silicon structure.[142] Tof-SIMS profile revealed lithium trapping at both interfaces (SEI|a-Si:H and a-Si:H|substrate) and in the bulk, with some correlation with silicon oxide species, essentially at interfaces. It should be stressed out that the bulk irreversible processes presently studied and identified to Li trapping cannot be associated with Li trapped at interfaces and therefore that a possible correlation of Li trapped in the bulk with oxygenated species remains uncertain.

The order of magnitude found for Li species trapped in the bulk yields a rather high amount of Li atoms, as compared to Si ones (~15%). Such a proportion is evocative of the hydrogen content in the material prior to the first lithiation. As noticed in chapter 3, this high hydrogen content is practically eliminated during the first lithiation. In a-Si:H, the density of states at Fermi level corresponds to defects and dangling bonds, which makes the material a

"classical" solid and restricts electronic transport to take place through hopping processes. In the hydrogenated, semiconducting material, transport can take place through weakly localized states in the band tails, where carriers can be emitted to extended (delocalized) states, thereby opening the possibility of long-range transport. Therefore, it can be tentatively suggested that, by playing a role somewhat similar to hydrogen in the pristine material, lithium trapped in silicon after delithiation is essential for the material to keep the capability of extended-range charge transport and behave as an electrode. Conversely, the need for the charges to be evacuated for releasing lithium alloyed to silicon prevents this residual lithium content to be released.

Contrary to naive expectation, the amount of Li irreversibly trapped in the bulk appears not to be affected by the methyl content of the $a\text{-}Si_{1-x}(CH_3)_x\text{:}H$ material, at least when x does not overcome 0.1. This result may be paralleled with the practically unchanged lithium specific capacity between a-Si:H and $a\text{-}Si_{0.9}(CH_3)_{0.1}\text{:}H$. This last result demonstrates that the Li-Si alloying capability is not significantly affected by the bonding of some Si atoms with methyl groups. A possibly important fact with respect to this capability is the existence of nanovoids around methyl groups which release steric constrain and leave enough room around methyl groups for allowing Si and Li atoms to interact more or less as in the absence of methyl groups. With respect to the irreversible trapping of Li atoms upon delithiation, it could be remarked that at low methyl content, methylated amorphous silicon exhibit semiconducting properties similar to a-Si:H. Therefore, the similar amount of Li trapped in the a-Si:H and $a\text{-}Si_{0.9}(CH_3)_{0.1}\text{:}H$ materials upon delithiation could equally be interpreted according to the tentative mechanism described above.

4.3 – Conclusion

Even though amorphous silicon methylation is a bulk modification, it interestingly appears to play a more important role in electrode surface reactions than in the bulk processes. This distinction is made possible by the thin-layer geometry of our experiments, which allows for reproducibly making experiments as a function of the layer thickness, providing an experimental means of tuning the proportion between surface and bulk phenomena. The incorporation of a modest amount of CH_3 (10 at.%) into the silicon amorphous matrix does not appreciably modify the degree of irreversible bulk processes, identified to Li atom trapping and tentatively interpreted in terms of semiconducting/transport properties of the material. More unexpectedly, bulk appears to modify the material surface properties when used as an electrode. This appears somewhat paradoxical, since the chemical surface composition before lithiation is not drastically modified. For example, the surface methylation obtained by CH_3 grafting on a-Si:H presented in the second chapter results in a much richer concentration of CH_3 species on the electrode surface than that associated with a 10 at.% bulk methylation, and this heavy surface methylation turns to have detrimental effects when using the layer as an electrode. It can be inferred that just like for the hydrogenated surface of a-Si:H, the numerous Si-H surface sites present in the hydrogenated surface of a-Si$_{0.9}$(CH$_3$)$_{0.1}$:H provide anchoring sites allowing for the formation of a stable SEI layer. Such a layer is intensively formed during the first lithiation of methylated silicon electrodes.

If the origin of a stable SEI formation on methylated amorphous silicon electrodes can plausibly be understood, the origin of the efficient quenching of other surface irreversible processes remains unexplained. It could be observed that methylated amorphous silicon is a more electronic resistive material than pure a-Si:H, which might hamper the efficient electron transfer on the electrode interface necessary for the electrolyte reduction, efficiently limiting parasite reactions at the beginning of the lithiation cycle. Once the lithiation starts to take place, it might be assumed that lithium affects the electronic structure of the silicon electrode, and that the level of electron transfer necessary for the electrolyte decomposition is reached and a well passivating SEI layer is intensively formed.

5 – GENERAL CONCLUSIONS AND PERSPECTIVES

Electrode interface is a zone of intense electrochemical reactions and plays an important role on reversible cycling and long-term stability of Li-ion systems. Part of this stability is obtained by the electrode passivation resulting from the electrolyte decomposition, which takes place at this interface and appears extremely dependent on the electrode surface chemical state. Therefore, in this work we studied the physicochemical effects of amorphous silicon lithiation, mostly focused on the surface processes and the SEI formation. Great part of the information was obtained by in situ FTIR spectroscopy in an ATR geometry which allowed us for probing electrode processes in the entire negative electrode until ~300 nm inside of the electrolyte. Since a significant part of the present work has been devoted to the technical or experimental aspects associated to the development of this in-situ infrared technique, it cannot benefit from the added value associated to the combination of many techniques for studying a given system. It is rather focused on what an in-situ analytical technique can bring in such a case.

Amorphous silicon electrodes were here used in a thin-film geometry, representing a model system for studying its electrochemical performance without the effect of electrode additives (binder, carbon black, etc.). Additionally, thin-geometry decrease the problems associated with film cracking, which helps for precisely quantifying the charges involved in the electrode processes and being less sensitive to effects of volume changes during electrochemical cycling. On the other hand, due to the low amount of active material in the electrochemical cell, the role of the substrate and side reactions becomes more pronounced in thin film geometry. Having it in mind, special attention was paid for identifying the critical aspects of the experimental setup, guiding us for an optimized electrochemical cell and substrate conditions which allow for precise and reproducible experiments.

A first guideline for the present work has been to look for the impact of surface chemical pretreatments on the electrode performances. The idea was to appreciate in which conditions an artificially designed SEI (or inner layer of a SEI) could improve these performances. Therefore, the amorphous silicon surface was chemically modified by the chemical grafting of different species, using state-of-the-art grafting techniques on oxide-free silicon. Making use of the previously optimized experimental conditions, it appears that the surface chemical modification of silicon result in a deep change on its electrochemical performance. The obtained results indicate that a grafted molecular layer has a beneficial effect when it provides anchoring sites for the covalent linking of the electrode active material to the electrolyte decomposition products. Of course, in-situ infrared spectroscopy appears as a valuable technique for investigating these effects. By making a quantitative evaluation of the SEI formed upon cycling it was clearly evidenced by in situ FTIR that well-suited, grafted molecular species make possible the quenching of parasitic reactions and

efficiently promote the formation of a passivating SEI formation with minimal charge consumption. Even if the surface treatments led to similar effects on the electrochemical performance and SEI characteristics of electrodes tested in LiClO$_4$ or LiPF$_6$ based electrolytes, it was observed that the SEI obtained in LiPF$_6$ based electrolyte has improved passivating properties and mostly contains salt decomposition products.

Another clear-cut result provided by in-situ infrared spectroscopy is that the SEI layer grows and dissolves upon lithiation and delithiation. Noticeably, this "breathing" of the SEI, in phase with the well-known swelling/shrinking of the active material, can be largely quenched by a grafted carboxydecyl layer, which is also the molecular layer for which the irreversible processes are the most efficiently passivated. Even if the correlation of this stabilization of the SEI to the improved passivation efficiency appears to make sense, the detailed microscopic processes responsible for this behavior remain an open question. A related, primary important question is to know whether specific kinds of molecules other than carboxyalkyl chain could yield even better results. From this view point, the present study still appears preliminary. If the main issue is to provide stable anchoring points, carboxyphenyl layers (which can be grafted by the diazonium route)[146] should yield similar results. If the covering capability of the molecular layer rather determines its efficiency, as it could be the case when VC is added to the electrolyte, alternative oxygen-containing polymers could also be interesting candidates. Such could be the case, e.g., for phenyl or ethynyl based polymers which, when formed by the anodic decomposition of a Grignard precursor in an ether-based electrolyte, incorporate ether-decomposition products in the formed layer.[147,148] It would be also interesting to investigate by in situ infrared spectroscopy the behavior of amorphous silicon electrodes grafted with PEG moities. It has been noticed in this work that such a chemical grafting yields similar performances as carboxydecyl grafting in terms of quenching of the irreversible processes. It would be especially interesting from a fundamental view point to know whether on such electrodes the SEI thickness remains stable or not. This class of molecules also offers interesting alternative for studying the effect of the thickness and covering efficiency of the grafted molecular layer by using different PEG blends, easily available at low cost.

Another specific results brought by in situ experiments has been the identification of the dynamic evolution of lithium concentration in the vicinity of the silicon electrode upon electrochemical cycling. Lithium concentration at the silicon|electrolyte interface increases during lithiation and decreases for essentially recovering its initial value during delithiation. The high lithium concentration found in the vicinity of the electrode during lithiation indicates that lithium incorporation in amorphous silicon is under kinematic control. The infrared analysis also points out the role of ion solvation in the chemical structure of the SEI. Regarding lithium incorporation in silicon, in-situ infrared spectroscopy also gives two useful additional pieces of information. First, the experiments revealed that the high amount of Si-H bonds present in the a-Si:H bulk material is irreversibly lost during lithiation. The second original information brought by the in situ infrared analysis is the existence of an apparent,

reversible infrared absorption in the bulk a-Si:H, which appears above a certain level of lithiation. Though an origin in terms of diffusion by spatial inhomogeinities could not totally be ruled out, a plausible interpretation is in term of the appearance of a Li-Si phase with a high lithium content, which would be responsible for this infrared absorption. This suggests that, at least during the first stage of lithiation (expect during the first lithiation of the electrode), lithium diffusion in a-Si:H is rather fast and that the picture of a moving boundary between a lithiated phase and a lithium free inner part of the layer should be questioned. At this stage, it appears that coupling in-situ infrared spectroscopy with surface techniques which would bring a depth profile information would be quite helpful for giving a more detailed insight into lithiation processes in the active material.

In the last part of this work, we finally take profit of the thin-layer geometry of our electrodes to evaluate the respective importance of surface and bulk origin of irreversible processes taking place during electrochemical cycling. In order to affect the irreversible processes associated to bulk lithiation, we choose to modify the material bulk composition (by analogy with chemical surface treatment which selectively affects the surface). For this purpose, we compared standard amorphous silicon a-Si:H to methylated amorphous silicon a-Si$_{0.9}$(CH$_3$)$_{0.1}$:H, a material which has demonstrated interesting cycling capacities under lithiation/delithiation. Even though the modification has been performed on the bulk composition, it has a more important effect on the irreversible capacity related to surface processes. The detailed mechanism of this improvement is still to be determined. Concerning the bulk processes, the similarity in the performances between a-Si:H and a-Si$_{0.9}$(CH$_3$)$_{0.1}$:H can be paralleled with the similar specific capacity of lithiation of the two materials. A proposal is that lithium modifies the electronic structure of silicon, probably taking place of hydrogen dangling bonds and allowing for long-range electronic transport in the bulk material, in either neat or methylated silicon. In the case of methylated silicon, lithium could also help to overcome an initial electronic barrier for SEI formation preventing parasitic reactions, leading to a differentiated SEI formation, very intensive and with high Faradaic efficiency.

In this picture, the bulk contribution to irreversible reactions appears as an irreducible process, intimately linked to silicon. It is responsible for a limited capacity irreversibly lost during the first lithiation only. Obtaining a clear cut confirmation of the relevance of the suggested mechanism does not appear an easy task. It might be suggested that increasing the carbon content of the methylated material above 20%, which is known to be detrimental to the lithiation capacity,[23] could also affect the amount of lithium irreversibly trapped in the material after delithiation, since increasing the carbon content is known to degrade the semi-conducting properties of the material by enhancing the density of localized states.[149]

As mentioned above, many questions remain open and many processes need to be clarified at the end of the present work. All the present results have been obtained with

thin-film electrodes. Before going further, this aspect deserves some discussion. It could be argued that such a strategy is of limited relevance since in all realistic systems, a silicon-based electrode is under (nano)dispersed form, included in a composite with binder, carbon black and so on. We still think that even if it does not aim at an immediate optimization of an operating system, the thin-film approach remain of major interest in the present context. The electrode surface control and the processes governing silicon lithiation remain critical for the efficiency of any silicon-based Li-ion system. Gaining a deeper understanding of these processes and of the factors allowing for their control remains of direct relevance, and for that purpose, the thin-film geometry provides decisive advantages, mostly because it allows for a quantitative approach and a depth resolution.

As already mentioned, the best strategy for tackling the above issues certainly includes the combination of in situ infrared spectroscopy, not only with electrochemical measurements, as performed in this work, but also with other analytic techniques. Among them, surface techniques appear as the most obvious and valuable candidates. When performed in a thin-film geometry, they provide powerful insight into surface chemistry and associated to profile techniques, they also bring the capability for depth analysis of the electrodes. They suffer from the drawbacks of ex-situ technique, which require cautious rinsing and transfer protocols for giving relevant information, and cannot maintain the operational environment during the analysis. A complementary approach would be to benefit from an extra analytic technique which, like infrared spectroscopy, could be performed in situ. With respect to this need, Raman spectroscopy (in spite of a somewhat limited sensitivity) appears as an interesting candidate. It offers an ideal complement to infrared spectroscopy, not only because it gives access to infrared-forbidden vibrational transitions, but mostly because it can provide an easier access to low-energy vibrational modes which are not easily accessed using ATR-FTIR spectroscopy. These modes are of major relevance for investigating some salt decomposition products (e.g., fluoride species) but could also provide interesting insight in the formation of Li-Si alloyed phases.[143] In addition, Raman scattering coupling to optical microscopy could provide a useful micrometer range resolution which could help in the analysis of surface chemistry at locations where cracks or delamination appear, which is observed when the layer thickness exceeds a critical value. A needed prerequisite consist in developing a special cell with an optical access and capability of electrochemical cycling under optical microscopy observation. This requirement has been fulfilled in the laboratory, so that the perspective of developing in-situ Raman analysis of electrodes during electrochemical cycling does not appear out of reach. Undertaking such an approach, combined with ex-situ other techniques, for addressing open questions concerning a-Si:H and a-Si$_{1-x}$(CH$_3$)$_x$:H electrodes, therefore appears as an exciting project.

Appendix A – Experimental procedures of molecular grafting

Surface methylation

Surface methylated electrodes were obtained by electrochemical grafting from Grignard reagents under inert conditions. Samples were etched by exposing to HF vapor during 10 s prior to be transferred into a nitrogen filled glove-box. In the glove-box the samples were anodically polarized in 3M methylmagnesium bromide in diethylether using a PTFE parallelepipedic cell, equipped with a U-shaped Cu counter-electrode. Anodization was performed for 5 min with an anodic current density of 0.2 mA cm^{-2}. After the electrochemical treatment, the samples were rinsed twice in diethylether and once in bromobutane. Once removed from the glove-box they were rinsed twice in ethanol, once in distilled water and dried under a dry nitrogen flow.

Grafting of decene

Silicon surface alkylation was performed by photochemical hydrosilylation of decene. A mixture of decene and undecanoic acid (3:1) was outgassed in a Schlenk tube under constant argon bubbling at 100°C for 30 min and cooled to room temperature prior to receive the silicon electrode. Silicon samples were etched by 10 s exposition to HF vapor prior to their introduction in the Schlenk tube containing the outgassed decene mixture. Once the electrodes were introduced the Schlenk tube, the reaction mixture was further outgassed for 5 min at room temperature, sealed under argon atmosphere and irradiated for 3 h in a UV reactor (6 mW cm^{-2}, 312 nm). The functionalized surface was finally rinsed with tetrahydrofuran and dichloromethane, and dried under a dry nitrogen flow.

Grafting of undecylenic acid

Silicon electrodes with a carboxyl surface termination were prepared by photochemical hydrosilylation of undecylenic acid. Concentrated undecylenic acid was outgassed under continuous argon bubbling in a Schlenk tube at 90°C for 30 min. Silicon electrodes were etched by exposition to HF vapor during 10 s prior to immersion into the outgassed undecylenic acid. After sample introduction into the Schlenk tube, outgassing was further performed at 90°C for 15 min. Then, the tube containing the samples immersed in

undecylenic acid was sealed under argon atmosphere and UV irradiated (6 mW cm^{-2}, 312 nm) in a reactor for 3 h. After this photochemical process, the samples were rinsed in acetic acid at 75°C for 15 min under argon bubbling, then rinsed in acetic acid at room temperature and dried under a dry nitrogen flow.

Grating of polyethylene glycol

Silicon surfaces were photochemically grafted with polyethylene glycol under UV irradiation. A polyethylene glycol blend with average mean molecular weight of 750 g mol^{-1} (Aldrich) was outgassed by continuous argon bubbling in a Schlenk tube at 80°C during 30 min. The polyethylene glycol blend was cooled to room temperature for receiving the etched (HF vapor for 10 s) silicon electrode and further outgassed for 15 min. The photo-induced grafting was obtained after 3 h of irradiation in a UV reactor (6 mW cm^{-2}, 312 nm). After the grafting, the samples was rinsed in ethanol and dichloromethane and dried under a dry nitrogen flow.

Combined undecylenic acid and polyethylene glycol grafting

Electrodes grafted with a combined acid/polyethylene glycol surface termination were obtained by first grafting the silicon surface with undecylenic acid, as previously described. Then, acid terminated surface was esterified with polyethylene glycol. Esterification was thermally activated. A mixture of 100 mM of polyethylene glycol and 10 mM of toluenesulfonic monohydrate acid (TsOH) in mesitylene was previously outgassed in a Schlenk tube under constant argon bubbling at 80°C for 30 min. The silicon acid-grafted electrode was then introduced in the outgassed mixture. The esterification reaction was obtained by heating the sealed Schlenk tube at 120°C for 2 h. After reaction, the electrodes were rinsed in acetonitrile at 60°C during 15 min, at room temperature in acetonitrile for 15 min, and finally dried under a dry nitrogen flow.

Appendix B – Principles of Fourier transform infrared spectroscopy

Fourier transform infrared spectroscopy is based on the use of a Michelson interferometer composed of a beam splitter, a fixed and a moving mirror. As described in Fig. 66, the light emitted from the radiation source is separated in two beams by the beam splitter. One beam is reflected by the fixed mirror and the other one by the moving mirror. The two beams are recombined by the beamsplitter in the exit arm of the interferometer where the emerging radiation probes the sample and reaches the detector. The path difference between the two light beams creates an interference pattern when the beams are recombined. An interferogram can then be generated by varying the optical path difference between the two arms of the interferometers, which is achieved by moving the mirror. The detector signal is then recorded as a function of the optical path difference created in the interferometer. Fourier transform of the signal provides the infrared spectrum of the source, affected by the response of the optical system (including the sample).
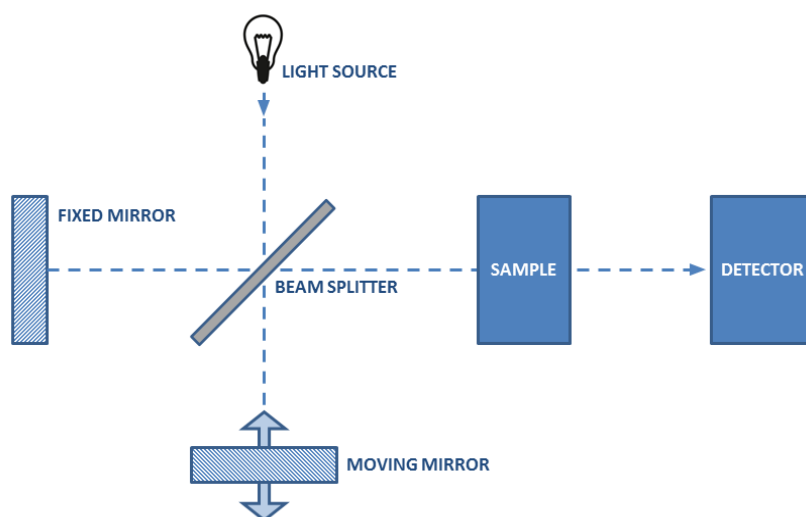

Fig. 66 – FTIR schematic diagram.

The infrared energy is generally expressed as a wavenumber ν (cm^{-1}), which can be related to the radiation wavelength λ (µm), frequency f (s^{-1}), or angular frequency ω (s^{-1}) as given by equation 1.

$$\nu = \frac{1}{\lambda} = \frac{f}{c} = \frac{\omega}{2\pi c} \qquad (1)$$

In this equation, c is the light velocity in vacuum. Infrared radiation encompasses the range of 10 to 13000 cm^{-1}; however, most of the vibrational information is generally collected in the mid infrared (400 – 4000 cm^{-1}).

Infrared radiation can be resonantly absorbed by the vibrational excitation of a molecular system, which may be described in terms of oscillators with resonant frequencies. Photons with frequencies matching the resonance energy of the oscillators present in the sample will be absorbed, creating characteristic absorption peaks in the obtained spectrum. In many cases, molecular vibrational resonances can be described in terms of localized vibration (ball and spring picture). In this picture, the major types of molecular vibrations are stretching and bending modes. They are illustrated in Fig. 67, which gives an atomic picture of the excitation.
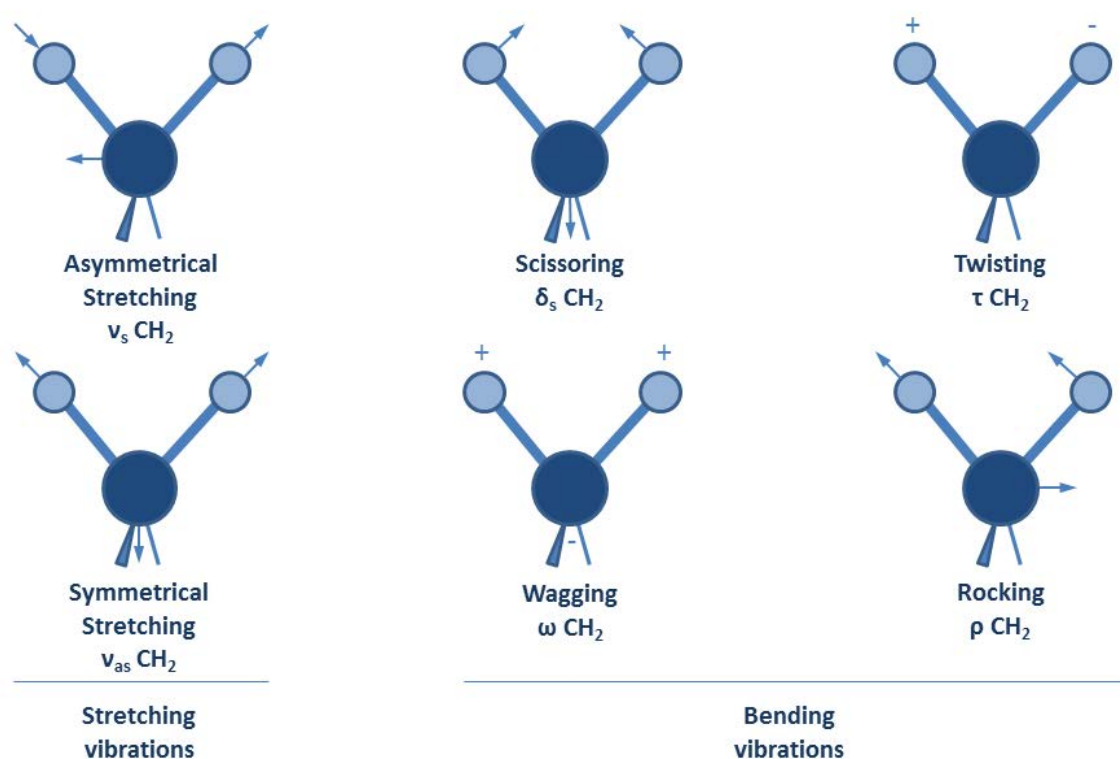

Fig. 67 – Main vibration modes for CH$_2$ molecules.

The ratio (T) between the intensity of a beam incident on a sample to that transmitted after crossing the sample is determined by the Beer-Lambert law (Eq. 2). (T) exponentially depends on the sample absorption coefficient (α) and the optical path probed by the infrared light across the sample (d).

$$T = I_T/I_0 = e^{-\alpha d} \qquad (2)$$

It is then useful to consider the absorbance (*A*) defined as the natural logarithm of the reciprocal of the transmittance (*T*) (Eq. 3).

$$A = - \ln T \qquad (3)$$

The absorbance is proportional to the absorption coefficient, i.e., to the concentration of the absorbing centers in the sample, allowing for quantitative studies.

Appendix C – Attenuated total reflection geometry

Under sufficiently oblique incidence, infrared radiation travelling in a medium of high refractive index will be totally reflected at the interface with a media of lower refractive index. Snell's law (Eq. 1) can be used to predict the critical incident angle Θ_C (Eq. 2).

$$n_a \sin(\theta_a) = n_b \sin(\theta_b) \qquad (1)$$

$$\theta_c = \sin^{-1}\left(\frac{n_b}{n_a}\right) \qquad (2)$$

In these equations, n is the refractive index of a media (a or b) and Θ is the incident angle. For any incident angle of incidence less than the critical angle (Θ_C), part of the light will be transmitted and part will be reflected as sketched in Fig. 68.
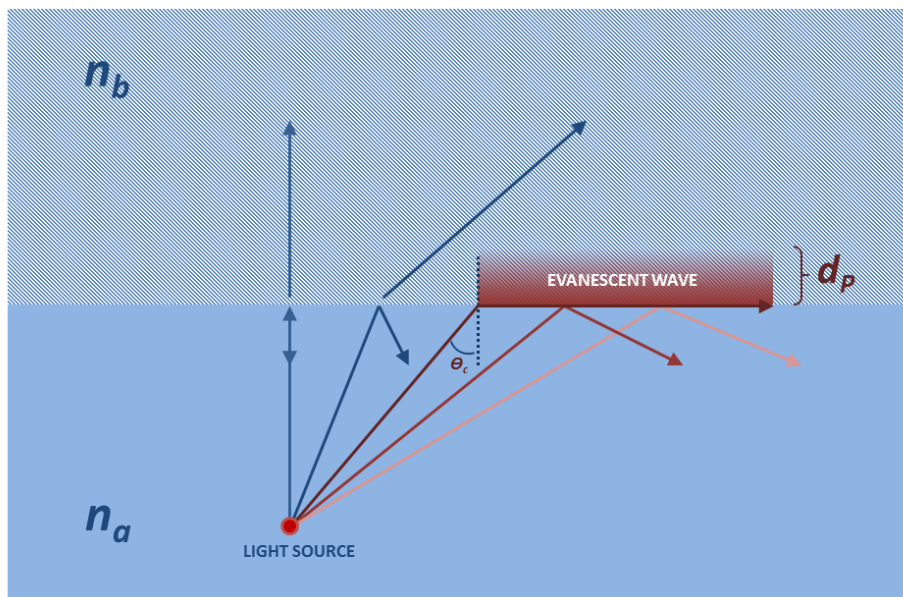

Fig. 68 – Scheme of reflected and transmitted light between two different media.

When total reflection takes place, infrared radiation does not abruptly decreases to zero intensity in the low-refractive index medium. An evanescent wave probes this medium on a characteristic penetration depth d_p given by Eq. (3).

$$d_P = \frac{\lambda}{2\pi(n_a{}^2 \sin^2\theta - n_b{}^2)^{1/2}} \qquad\qquad (3)$$

In equation 3, λ is the incoming wavelength, n_a and n_b are the refractive index of the different media and θ is the angle of incidence.

Attenuated total reflection (ATR) geometry makes use of this phenomenon. In this case, infrared radiation is guided in a prism whose faces are totally reflecting the radiation. If a sample of interest is deposited on one prism face, the infrared beam will undergo multiple reflection at the face in contact with the sample. The sample is therefore probed by the evanescent wave, which can be absorbed within the sample and allows for its characterization. The sensitivity is enhanced by the multiple reflections taking place at the prism surface.

Writing down the equations for the reflection coefficient at the surface gives a precise determination of the infrared intensity probing the sample, which allows for quantitative measurement. More details can be found in classical text books.[89,91,150,151,152]

6 – References

[1] C. Jordy, G. Cailon, N. Roumegous, T. Gacoin, F. Ozanam, A. Kocan, L. Touahir. Matière active à base de silicium greffé pour électrode négative d'accumulateur au lithium. FR 10 50613 (2010).

[2] T. Minami, M. Tatsumisago, M. Wakihara, C. Iwakura, S. Kohjiya, I. Tanaka. Solid state ionics for batteries. Springer, 2005.

[3] J.-M. Tarascon, M. Armand. Issues and challenges facing rechargeable lithium batteries. Nature 414 (2001) 359-367.

[4] M. Armand, J.-M. Tarascon. Building better batteries. Nature 451 (2008) 652-657.

[5] C.K. Chan, H. Peng, G. Liu, K. McIlwrath, X.F. Zhang, R.A. Huggins, Y. Cui. High-performance lithium battery anodes using silicon nanowires. Nature Nanotechnology 3 (2008) 31-35.

[6] D. Larcher, S. Beattie, M. Morcrette, K. Edström, J.-C. Jumas, J.-M. Tarascon. Recent findings and prospecst in the field of pure metals as negative electrodes for Li-ion batteries. Journal of Materials Chemistry 17 (2007) 3759-3772.

[7] H. Okamoto. Li-Si (Lithium-Silicon). Journal of Phase Equilibria and Diffusion 30 (2009) 118-119.

[8] Y. He, X. Yu, G. Li, R. Wang, H. Li, Y. Wang, H. Gao, X. Huang. Shape evolution of patterned amorphous and polycrystalline silicon microarray thin film electrodes caused by lithium insertion and extraction. Journal of Power Sources 216 (2012) 131-138.

[9] W.-J. Zhang. Lithium insertion/extraction mechanism in alloy anodes for lithium-ion batteries. Journal of Power Sources 196 (2011) 877-885.

[10] J. Li, J.R. Dahn. An in situ x-ray diffraction study of the reaction of Li with crystalline Si. Journal of The Electrochemical Society 154-3 (2007) A156-A161.

[11] L.Y. Beaulieu, K.W. Eberman, R.L. Turner, J.L. Krause, J.R. Dahn. Colossal reversible volume changes in lithium alloys. Electrochemical and solid state letters 4 (9) (2001) A137-A140.

[12] M. Ulldemolins, F. Le Cras, B. Pecquenard, V.P. Phan, L. Martin, H. Martinez. Investigation on the part played by the solid electrolyte interphase on the electrochemical performances of the silicon electrode for lithum-ion batteries. Journal of Power Sources 206 (2012) 245-252.

[13] J.H. Ryu, J.W. Kim, Y.-E. Sung, S.M. Oh. Failure modes of silicon powder negative electrode in lithium secondary batteries. Electrochemical and Solid State Letters 7(10) (2004) A306-A309.

[14] W.-J. Zhang. A review of the electrochemical performance of alloy anodes for lithium-ion batteries. Journal of Power Sources 196 (2011) 13-24.

[15] S.S. Zhang. A review on electrolyte additives for lithium-ion batteries. Journal of Power Sources 162 (2006) 1379-1394.

[16] E. Peled, D. Bar Tow, A. Merson, A. Gladkich, L. Burstein, D. Golodnitsky. Composition, depth profiles and lateral distribution of materials in the SEI built on HOPG-TOF SIMS and XPS studies. Journal of Power Sources 97 (2001) 52-57.

[17] D. Bar-Tow, E. Peled, L. Burstein. A study of high oriented pyrolytic graphite as a model for the graphite anode in Li-ion batteries. Journal of the Electrochemical Society 146 (1999) 824-832.

[18] J. Vetter, P. Novák, M.R. Wagner, C. Veit, K.-C. Möller, J.O. Besenhard, M. Winter, M. Wohlfahrt-Mehrens, C. Vogler, A. Hammouche. Ageing mechanisms in lithium-ion batteries. Journal of Power Sources 147 (2005) 269-281.

[19] L. Chen, K. Wang, X. Xie, J. Xie. Effect of vinylene carbonate (VC) as electrolyte additive on electrochemical performance of Si film anode for lithium ion batteries. Journal of Power Sources 174 (2007) 538–543.

[20] N.-S. Choi, K.H. Yew, K.Y. Lee, M. Sung, H. Kim, S.-S. Kim. Effect of fluoroethylene carbonate additive on interfacial properties of silicon thin-film electrode. Journal of Power Sources 161 (2006) 1254–1259.

[21] I. Solomon, M.P. Schmidt, H. Tran-Quoc. Selective low-power plasma decomposition of silane-methane for the preparation of methylated amorphous silicon. Physical Review B 38 (1988) 9895-9901.

[22] S.P.V. Nadimpalli, V.A. Sethuraman, S. Dalavi, B. Lucht, M.J. Chon, V.B. Shenoy, P.R. Guduru. Quantifying capacity loss due to soli-electrolyte-interphase layer formation on silicon negative electrodes in lithium-ion batteries. Journal of Power Sources 215 (2012) 145-151.

[23] L. Touahir, A. Cheriet, D.A. Dalla Corte, J.-N. Chazaviel, C.H. de Villeneuve, F. Ozanam, I. Solomon, A. Keffous, N. Gabouse, M. Rosso. Methylated silicon: a longer cycle-life material for Li-ion batteries. Journal of Power Sources 240 (2013) 551-557.

[24] B. Racine, A.C. Ferrari, N.A. Morisson, I. Hutchings, W.I. Milne, J. Robertson. Properties of amorphous carbon-silicon alloys deposited by high plasma density source. Journal of Applied Physics 90 (2001) 5002-5012.

[25] M.J. Chon, V.A. Sethuraman, A. McCormick, V. Srinivasan, P.R. Guduru. Real-time measurement of stress and damage evolution during initial lithiationof crystalline silicon. Physical Review Letters (2011) 107, 045503.

[26] B. Gao, S. Sinha, L. Fleming, O. Zhou. Alloy Formation in Nanostructured Silicon. Advanced Materials 13 (2001) 816-819.

[27] G.G. Amatucci, Nathalie Pereira. Fluoride based electrodes materials for advanced energy storage devices. Journal of Fluorine Chemistry 128 (2007) 243-262.

[28] L. Dupont, S. Grugeon, S. Laruelle, J-M. Tarascon. Structure, texture and reactivity versus lithium of chromium-based oxides films as revealed by TEM investigations. Journal of Power Sources 164 (2007) 839-848.

[29] P. Verma, P. Maire, P. Novák. A review of the features and analyses of the solid electrolyte interphase in Li-ion batteries. Electrochimica Acta 55 (2010) 6332–6341.

[30] B. Philippe, R. Dedryvère, J. Allouche, F. Lindgren, M. Gorgoi, H. Rensmo, D. Gonbeau, K. Edström. Nanosilicon electrodes for lithium-ion batteries: interfacial mechanisms studied by hard and soft x-ray photoelectron spectroscopy. Chemistry of Materials 24 (2012) 1107-1115.

[31] P. Verma, P. Novák. Formation of artificial solid electrolyte interphase by grafting for improving Li-ion intercalation and preventing exfoliation of graphite. Carbon 50 (2012) 2599-2614.

[32] S. Ciampi, J.B. Harper, J.J. Gooding. Wet chemical routes to the assembly of organic monolayers on silicon surfaces via the formation of Si-C bonds: surface preparation, passivation and functionalization. Chemical Society Reviews 39 (2010) 2158-2183.

[33] D. Bélanger, J. Pinson. Electrografting: a powerful method for surface modification. Chemical Society Reviews 40 (2011) 3995-4048.

[34] M.M. Chehimi. Aryl Diazonium Salts: New coupling agents in polymer and surface science. Wiley-VCH, 2012.

[35] Q. Pan, Y. Jiang. Effect of covalently bonded polysiloxane multilayers on the electrochemical behavior of graphite electrode in lithium ion batteries. Journal of Power Sources 178 (2008) 379–386.

[36] Q. Pan, H. Wang, Y. Jiang. Natural graphite modified with nitrophenyl multilayers as anode materials for lithium ion batteries. Journal of Materials Chemistry 17 (2007) 329–334.

[37] Q. Pan, H. Wang, Y. Jiang. Covalent modification of natural graphite with lithium benzoate multilayers via diazonium chemistry and their application in lithium ion batteries. Electrochemistry Communications 9 (2007) 754–760.

[38] C. Martin, M. Alias, F. Christien, O. Crosnier, D. Bélanger, T. Brousse. Graphite-grafted silicon nanocomposite as a negative electrode for lithium-ion batteries. Advanced Materials 21-46 (2009) 4735-4741.

[39] U. Lafont, L. Simonin, M. Gaberscek, E.M. Kelder. Carbon coating via an alkyl phosphonic acid grafting route: Application on TiO_2. Journal of Power Sources 174 (2007) 1104–1108.

[40] W. Xu, S.S. Sai, S. Vegunta, J.C. Flake. Surface-modified silicon nanowire anodes for lithium-ion batteries. Journal of Power Sources 196 (2011) 8582-8589.

[41] S. Alexander. Adsorption of chain molecules with polar head, a scaling description. Journal of Physics France 38 (1977) 983-987.

[42] P. Thissen, O. Seitz, Y.J. Chabal. Wet chemical surface functionalization of oxide-free silicon. Progress in Surface Science 87 (2012) 272-290.

[43] V.P. Tolstoy, I.V. Chernyshova, V.A. Skryshevsky. Handbook of infrared spectroscopy of ultrathin films. John Wiley & Sons, New Jersey, 2003.

[44] A. Lehner, G. Steinhoff, M.S. Brandt, M. Eickhoff, M. Stuzmann. Hydrolisation of crystalline silicon (111) and hydrogenated amorphous silicon surfaces: a comparative x-ray photoelectron spectroscopy study. Journal of Applied Physics 94-4 (2003) 2289-2294.

[45] W. Cai, Z. Lin, T. Strother, R.J. Hamers. Chemical modifications and patterning of iodine-terminated silicon surfaces using visible light. Journal of Physical Chemistry B 106 (2002) 2656-2664.

[46] A. Bansal, X. Li, I. Lauermann, N.S. Lewis, S. I. Yi, W.H. Weinberg. Journal of the American Chemical Society 118 (1996) 7225-7226.

[47] B.R. Weinberger, H.W. Deckman, E. Yablonovitch, T. Gmitter, W. Kobasz, S. Garoff. The passivation of electrical active sites on the surface of crystalline silicon by fluorination. Journal of Vacuum Science and Technology A 3 (1985) 887-891.

[48] P. Thissen, O. Seitz, Y.J. Chabal. Wet chemical surface functionalization of oxide-free silicon. Progress in Surface Science 87 (2012) 272-290.

[49] P. Allongue, V. Costa-Kieling, H. Gerischer. Etching of silicon in NaOH solutions. I. In situ scanning tunneling microscopic investigation of n-Si(111). Journal of the Electrochemical Society 140 (1993) 1009-1018.

[50] P. Allongue, V. Costa-Kieling, H. Gerischer. Etching of silicon in NaOH solutions. II. Electrochemical studies of n-Si(111) and (100) and mechanism of the dissolution. Journal of the Electrochemical Society 140 (1993) 1018-1026.

[51] E.R. Lippincott, A.Van Valkenburg, C.E. Weir, E.N. Bunting. Infrared studies on polymorphs of silicon dioxide and germanium dioxide. Journal of Research of the National Bureau of Standards 61 (1958) 61-70.

[52] P.G. Pai, S.S. Chao, Y. Takagi, G. Lucovsky. Infrared spectroscopic study of SiO_x films produced by plasma enhanced chemical vapor deposition. Journal of Vacuum Science Technology A 4-3 (1986) 689-694.

[53] G. Lucovsky, P.D. Richard, D.V. Tsu, S.Y. Lin, R.J. Markunas. Deposition of silicon and silicon nitride by remote plasma enhanced chemical vapor deposition. Journal of Vacuum Science and Technology A 4-3 (1986) 681-688.

[54] S.-Y. Lin. Vibrational modes of $a-SiO_2$:H and variation of local modes in different local environments. Journal of Applied Physics 82 (1997) 5976-5982.

[55] C.T. Kirk. Quantitative analysis of the effect of disorder-induced mode coupling on infrared absorption in silica. Physical Review B 38 (1988) 1255-1273.

[56] J. Lambers, P. Hess. Infrared spectra of photochemically grown suboxides at the Si/SiO2 interface. Journal of Applied Physics 94 (2003) 2937-2941.

[57] A. Ermolieff, F. Martin, A. Amouroux, S. Marthon, J.F.M. Westendorp. Surface composition analysis of HF vapour cleaned silicon by x-ray photoelectron s[ectroscopy. Applied Surface Science 48 (1991) 178-184.

[58] J. Saint, M. Morcrette, D. Larcher, L. Laffont, S. Beattie, J.-P. Pérès, D. Talaga, M. Couzi, J.-M. Tarascon. Towards a fundamental understanding of the improved electrochemical performances of silicon-carbon composites. Advanced Functional Materials 17-11 (2007) 1765-1774.

[59] S. Xun, X. Song, L. Wang, M.E. Grass, Z. Liu, V.S. Battaglia, G. Liu. The effect of native oxide layer on the electrochemical performance of Si nanoparticle-based electrodes. Journal of The Electrochemical Society 158 (2011) A1260-A1266.

[60] A. Fidélis, F. Ozanam, J.-N. Chazaviel. Fully methylated, atomically flat (111) silicon surface. Surface Science 444 (2000) L7-L10.

[61] A. Teyssot, A. Fidélis, S. Fellah, F. Ozanam, J.-N. Chazalviel. Anodic grafting of organic groups on the silicon surface. Electrochimica Acta 47 (2002) 2565-2571.

[62] T. Dubois, F. Ozanam, J.-N. Chazalviel. Electrochemical Society Proceedings 97-7 (1997) 296.

[63] X. Wang, R.E. Ruther, J.A. Streifer, R.J. Hamers. UV-induced grafting of alkenes to silicon surfaces: photoemission versus excitons. Journal of the American Chemical Society Communications 132 (2010) 4048-4049.

[64] A.B. Sieval, A.L. Demirel, J.W.M. Nissink, M.R. Linford, J.H. van der Maas, W.H. de Jeu, H. Zuilhof, E.J.R. Sudhölter. Highly stable Si-C linked functionalized monolayers on the silicon (100) surface. Langmuir 14 (1998) 1759-1768.

[65] M.R. Linford, C.E.D. Chidsey. Alkyl monolayers covalently bonded to silicon surfaces. Journal of the American Chemical Society 115 (1993) 12631-12632.

[66] R.L. Cicero, M.R. Linford, C.E.D. Chidsey. Photoreactivity of unsaturated compounds with hydrogen-terminated silicon(111). Langmuir 16 (2000) 5688-5695.

[67] X. Wallart, C. Henry de Villeneuve, P. Allongue. Truly quantitative XPS characterization of organic monolayers on silicon: study of alkyl and alkoxy monolayers on H-Si(111). Journal of the American Chemical Society 127 (2005) 7871-7878.

[68] P. Gorostiza, C. Henry de Villeneuve, Q.Y. Sun, F. Sans, X. Wallart, R. Boukherroub, P. Allongue. Water exclusion at the nanometer scale provides long-term passivation of silicon (111) grafted with alkyl monolayers. Journal of Physical Chemistry B 110 (2006) 5576-5585.

[69] B. Zdyrko, S.K. Varshney, I. Luzinov. Effect of molecular weight on synthesis and surface morphology of high-density poly(ethylene glycol) grafted layers. Langmuir 20 (2004) 627-6735.

[70] A. Faucheux, A.C. Gouget-Laemmel, C. Henry de Villeneuve, R. Boukherroub, F. Ozanam, P. Allongue, J.-N. Chazaviel. Well-defined carboxyl-terminated alkyl monolayers grafted onto H-Si(111): packing density from a combined AFM and quantitative IR study. Langmuir 22 (2006) 153-162.

[71] Q.-Y. Sun, L.C.P.M. de Smet, B. Van Lagen, M. Giesbers, P.C. Thuene, J. Van Engelenburg, F.A. De Wolf, H. Zuilhof, E.J.R. Sudhölter. Covalently attached monolayers on crystalline hydrogen-terminated silicon: extremely mild attachment by visible light. Journal of American Chemical Society 127 (2005) 2514-2523.

[72] A. Faucheux, A.C. Gouget-Laemmel, P. Allongue, C. Henry de Villeneuve, F. Ozanam, J.-N. Chazaviel. Mechanisms of thermal decomposition of organic monolayers grafted on (111) silicon. Langmuir 23 (2007) 1326-1332.

[73] J.H. Lee, H.B. Lee, J.D. Andrade. Blood compatibility of polyethylene oxide surfaces. Progress in Polymer Science 20-6 (1995) 1043-1079.

[74] B. Zdyrko, S.K. Varshney, I. Luzinov. Effect of molecular weight on synthesis and surface morphology of high-density poly(ethylene glycol) grafted layers. Langmuir 20 (2004) 6727-6735.

[75] Y. Uyama, K. Kato, Y. Ikada. Surface modification of polymer by grafting. Advances in Polymer Sciences 137 (1998) 1-39.

[76] R. Boukherroub, S. Morin, P. Sharpe, D.D.M. Wayner, P. Allongue. Insights into the formation mechanisms of Si-OR monolayers from the thermal reactions of alcohols and aldehydes with Si(111)-H[1]. Langmuir 16 (2000) 7429-7434.

[77] E. Perez, K. Lahlil, C. Rougeau, A. Moraillon, J.-N. Chazaviel, F. Ozanam, A.C. Gouget-Laemmel. Influence of the molecular design on the antifouling performance of poly(ethylene glycol) monolayers grafted on (111) Si. Langmuir 28 (2012) 14654-14664.

[78] S.J. Blanksby, G.B. Ellison. Bond dissociation energy of organic molecules. Accounts of Chemical Research 36 (2003) 255-263.

[79] B. de B. Darwent. Bond dissociation energy in simple molecules. National Standard Reference Data System – National Bereau of Standars (U.S.), 1970.

[80] A. de Klerk. Fischer-Tropsch Refining. John Willey & Sons, 2012.

[81] J. Fossey, D. Lefort, J. Sorba. Free radicals in organic chemistry. Wiley (1995).

[82] D.F. McMillen, D.M. Golden. Hydrocarbon bond dissociation energies. Annual Review in Physical Chemistry 33 (1982) 493-532.

[83] M. Baklanov, P.S.Ho, E. Zschech. Advanced Interconnects for ULSI Technology. John Willey & Sons, 2012.

[84] P. Harder, M. Grunze, R. Dahint, G.M. Whitesides, P.E. Laibinis. Molecular conformation in oligo(ethylene glycol-terminated self-assembled monolayers on gold and silver surfaces determines their ability to resist protein adsorption. Journal of Physical Chemistry B 102 (1998) 426-436.

[85] A.V. Rao, J.-N. Chazalviel, F. Ozanam. In situ characterization of the n-Si/acetonitrile interface by electromodulated infrared internal-relfection spectroscopy. Journal of Applied Physics 60 (1986) 696-706.

[86] J.-N. Chazalviel, A.V. Rao. Optical absorption by surfaces states and atomic reorganization effects at the semiconductor/electrolyte interface. Journal of the Electrochemical Society 134 (1987) 1138-1143.

[87] F. Ozanam, C. Da Fonseca, A.V. Rao, J.-N. Chazalviel. In situ spectroelectrochemical study of the anodic dissolution of silicon by potential-difference and electrochemical electromodulated FT-IR spectroscopy. Applied Spectroscopy 51 (1997) 519-525.

[88] J.-N. Chazalviel, B.H. Erné, F. Maroun, F. Ozanam. In situ infrared spectroscopy of the semiconductor | electrolyte interface. Journal of Electroanalytical Chemistry 509 (2001) 108-118.

[89] N.J. Harrick. Vertical double-pass multiple reflection element for internal reflection spectroscopy. Applied Optics 5 (1966) 1-3.

[90] A. Tardella, J.-N. Chazalviel. In situ chemical information at the semiconductor/electrolyte interface from infrared vibrational spectroscopy. Applied Physics Letters 47 (1985) 334-338.

[91] Y.J. Chabal. Surface infrared spectroscopy. Surface Science Reports 8 (1988) 211-357.

[92] A.J. Bard, L.R. Faulkner. Electrochemical methods: Fundamental and Applications. John Wiley & Sons, Inc.

[93] L.A. Matheson. The intensity of infrared absorption bands. Physical Review 40 (1932) 813-828.

[94] Y. Ikezawa, T. Ariga. In situ FTIR spectra at the Cu electrode/propylene carbonate solution interface. Electrochimica Acta 52 (2007) 2710-2715.

[95] F. Joho, P. Novák. SNIFTIRS investigations of the oxidative decomposition of organic-carbonate-based electrolytes for lithium-ion cells. Electrochimica Acta 45 (2000) 3589-3599.

[96] K. Nishikawa, M. Ota, S. Izuo, Y. Fukunaka, E. Kusaka. R. Ishii, J.R. Selman. Transient natural convection induced by electrodeposition of Li^+ ions onto lithium metal vertical cathode in propylene carbonate. Journal of Solid State Electrochemistry 8 (2004) 174-181.

[97] K. Nishikawa, Y. Fukunaka, T. Sakka, Y.H. Ogata, J.R. Selman. Measurements of concentration profile during charging of Li battery anode materials in $LiClO_4$-PC electrolyte. Electrochimica Acta 53 (2007) 218-223.

[98] D.E. Arrega-Salas, A.K. Sra, K. Roodenko, Y.J. Chabal, C.L. Hinkle. Progression of solid electrolyte interphase formation on hydrogenated amorphous silicon anodes for lithium-ion batteries. The Journal of Physical Chemistry C 116 (2012) 9072-9077.

[99] S. Grugeon, S. Laruelle, R. Herrera-Urbina, L. Dupont, P. Poizot, J.-M. Tarascon. Particle size effects on the electrochemical performance of copper oxides toward lithium. Journal of the Electrochemical Society 148 (2001) A285-292.

[100] X.H. Huang, J.P. Tu, X.H. Xia, X.L. Wang, J.Y. Xiang, L. Zhang, Y. Zhou. Morphology effect on the electrochemical performance of NiO films as anodes for lithium ion batteries. Journal of Power Sources 188 (2009) 588-591.

[101] X. Li, J. Yang, Y. Hu, J. Wang, Y. Li, M. Cai, R. Li, X. Sun. Novel approach toward a binder-free and current collector-free anode configuration: highly flexible nanoporous carbon nanotube electrodes with strong mechanical strength harvesting improved lithium storage. Journal of Materials Chemistry 22 (2012) 18847-18853.

[102] K. Striebel, E. Sakai, E. Cairns. Impedance studies of the $LiMn_2O_4$/$LiPF_6$-DMC-EC interface. Electrochemical Society Proceedings Volume 2000-21 (2001) 569-574.

[103] D.C. Marra, W.M.M. Kessels, M.C.M. van de Sanden, K. Kashefizadeh, E.S. Aydil. Surface hydride composition of plasma hydrogenated amorphous silicon: in situ infrared study of ion flux and temperatures dependence. Surface Science 530 (2003) 1-16.

[104] D.M. Goldie, S.K. Persheyev. Quantitative hydrogen measurements in PECVD and HWCVD a-Si:H using FTIR spectroscopy. Journal of Materials Science 41 (2006) 5287-5291.

[105] B. Key, M. Morcrette, J.-M. Tarascon, C.P. Grey. Pair distribution function analysis and solid state NMR studies of silicon electrodes for lithium ion batteries: understanding the (De)lithiation mechanisms. Journal of the American Chemical Society 133 (2011) 503-512.

[106] H. Kim, C.-Y. Chou, J.G. Ekerdt, G.S. Hwang. Structure and properties of Li-Si alloys: a first-principles study. The Journal of Physical Chemistry C 115 (2011) 2514-2521.

[107] T.F. Young, C.P. Chen, J.F. Liou, Y.L. Yang, T.C. Chang. Study on the Si-Si vibrational states of the near surface region of porous silicon. Journal of Porous Materials 7 (2000) 339-343.

[108] H. Touir, K. Zellama, J.-F. Morhange. Local Si-H bonding environment in hydrogenated amorphous silicon films in relation to structural inhomogeneities. Physicla Review B 59 (1999) 10076-10083.

[109] M. Niwano M. Terashi, M. Shinohara, D. Shoji, N. Miyamoto. Oxidation processes on the H_2O-chemisorbed Si(100) surface studied by in-situ infrared spectroscopy. Surface Sciences 401 (1998) 364-370.

[110] R. Dedryvère, L. Gireaud, S. Grugeon, S. Laruelle, J.-M. Tarascon, D. Gonbeau. Characterization of lithium alkyl carbonates by x-ray photoelectron spectroscopy: experimental and theoretical study. The Journal of Physcial Chemistry B 109 (2005) 15868-15875.

[111] K. Xu, G.V. Zhuang, J.L. Allen, U. Lee, S.S. Zhang, P.N. Ross Jr., T.R. Jow. Syntheses and characterization of lithium alkyl mono- and dicarbonates as components of surface film in Li-ion batteries. The Journal of Physical Chemistry B 110 (2006) 7708-7719.

[112] S. Matsuta, T. Asada, K. Kitaura. Vibrational assignments of lithium alkyl carbonate and lithium alkoxide in the infrared spectra an ab initio MO study. Journal of the Electrochemical Society 147 (2000) 1695-1702.

[113] Y. Wang, P.B. Balbuena. Theoretical insights into the reductive decomposition of propylene carbonate and Vinylene carbonate: density functional theory studies. The Journal of Physical Chemistry B 106 (2002) 4486-4495.

[114] P.B. Balbuena, Y. Wang. Lithium-ion batteries: solid electrolyte interphase. Imperial College Press (2004).

[115] C. Emmeluth, B.L.J. Poad. C.D. Thompson, G.H. Weddle, E.J. Bieske. Infrared spectra of Li^+-$(H_2)_n$ (n=1-3) cation complexes. The Journal of Chemical Physics 126 (2007) 204309.

[116] B. Simon, J.-P. Boeuve. Rechargeable lithium electrochemical cell. U.S. Patent 5,626,981 (1997).

[117] K. Tasaki, K. Kanda, T. Kobayashi, S. Nakamura, M. Ue. Theoretical studies on the reductive decompositions of solvents and additives for lithium-ion batteries near lithium anodes. Journal of the Electrochemical Society 153 (2006) A2192-A2197.

[118] D. Aurbach, K. Gamolsky, B. Markovsky, Y. Gofer, M. Schmidt, U. Heider. Electrochimica Acta 47 (2002) 1423-1439.

[119] L. El Ouatani, R. Dedryvère, C. Siret, P. Biensan, S. Reynaud, P. Iratçabal, D. Gonbeau. The effect of vinylene carbonate additive on surface film formation on both electrodes in Li-ion batteries. Journal of the Electrochemical Society 156 (2009) A103-A113.

[120] R. McMillan, H. Slegr, Z.X. Shu, W. Wang. Fluoroethylene carbonate electrolyte and its use in lithium ion batteries with graphite anodes. Journal of Power Sources 81–82 _1999. 20–26

[121] C. Jung. Electrochemical absorption effect of BF4 anion salt on SEI layer formation. Solid State Ionics 179 (2008) 1717-1720.

122 I.A. Profatilova, S.-S. Kim, N.-S. Choi. Enhanced thermal properties of the solid electrolyte interphase formed on graphite in an electrolyte with fluoroethylene carbonate. Electrochimica Acta 54 (2009) 4445-4450.

123 V. Etacheri, O. Haik, Y. Goffer, G.A. Roberts, I.C. Stefan, R. Fasching, D. Aurbach. Effect of fluoroethylene carbonate (FEC) on the performance and surface chemistry of si-nanowire li-ion battery anodes. Langmuir 28 (2012) 965-976.

124 I.A. Profatilova, T. Langer, J.P. Badillo, A. Schmitz, H. Orthner, H. Wiggers, S. Passerini, M. Winter. Thermally induced reactions between lithiated nano-silicon electrode and electrolyte for lithium-ion batteries. Journal of the electrochemical Society 159 (2012) A657-663.

125 J.E. Katon, M.D. Cohen. The vibrational spectra and structure of dimethyl carbonate and its conformational behavior. Cnadian Journal of Chemistry 53 (1975) 1378-1386.

126 B.P. Kar, N. Ramanathan, K. Sundararajan, K.S. Viswanathan. Conformations of dimethyl carbonate and its complexes with water: a matrix isolation infrared and ab initio study. Journal of Molecular Structure 1024 (2012) 84-93.

127 D. Aurbach, Y. Gofer, J. Langzam. The correlation between surface chemistry, surface morphology, and cycling efficiency of lithium electrodes in a few polar aprotic systems. Journal of the Electrochemical Society 136 (1989) 3198-3205.

128 D. Aurbach, M.D. Levi, E. Levi, A. Schechter. Failure and stabilization mechanisms of graphite electrodes. The Journal of Physical Chemistry B 101 (1997) 2195-2206.

129 H. Ota, Y. Sakata, A. Inoue, S. Yamaguchi. Analysis of vynilene carbonate derived SEI layers on graphite anode. Journal of the Electrochemical Society 151 (2004) A1659-1669.

130 N. Delpuech, N. Dupré, D. Mazouzi, J. Gaubicher, P. Moreau, J.S. Bridel. Correlation between irreversible capacity and electrolyte solvents degradation probed by NMR in Si-based negative electrode of Li-ion cell. Electrochemistry Communications 33 (2013) 72-75.

131 R. Mogi, M. Inaba, Y. Iriyama, T. Abe, Z. Ogumi. Study of the decomposition of propylene carbonate on lithium metal surface by pyrolysis-gas chromatography-mass spectroscopy. Langmuir 19 (2003) 814-821.

132 R. Marom, I. Halalay, O. Haik, E. Zinigrad, D. Aurbach. Revisiting $LiClO_4$ as an electrolyte for rechargeable lithium-ion batteries. Journal of the Electrochemical Society 157 (2010) A972-A983.

133 K.K. Sharma. Optics: principle and applications. Academic Press, Elsevier (2006).

134 H.R. Philipp, E.A. Taft. Optical constants of silicon in the region 1 to 10 eV. Physical Review 120 (1960) 37-38.

135 V.A. Sethuraman, M.J. Chon, M. Shimshak, V. Srinivasan, P.R. Guduru. In situ measurements of stress evolution in silicon thin films during electrochemical lithiation and delithiation. Journal of Power Sources 195 (2010) 5062-5066.

136 C.-Y. Chou, G.S. Hwang. Surface effects on the structure and lithium behavior in lithiated silicon: a first principle study. Surface Science 612 (2013) 16-23.

137 X.H. Liu, J.W. Wang, S. Huang, F. Fan, X. Huang, Y. Liu, S. Krylyuk, J. Yoo, S.A. Dayeh, A.V. Davydov, S.X. Mao, S.T. Picraux, S. Zhang, J. Li, T. Zhu, J.Y. Huang. In situ atomic-scale imaging of electrochemical lithiation in silicon. Nature Technology 7 (2012) 749-756.

138 M. Cross, M.J. Adams. Effects of doping and free carriers on the refractive index of direct-gap semiconductors. Opto-electronics 6 (1974) 199-216.

[139] K. von Rottkay, M. Rubin, S.-J. Wen. Optical indices of electrochromic tungsten oxide. Thin Solid Films 306 (1997) 10-16.

[140] N. Özer, M.D. Rubin, C.M. Lampert. Optical and electrochemical characteristics of niobium oxide films prepared by sol-gel process and magnetron sputtering: A comparison. Solar Energy Materials and Solar Cells 40 (1996) 285-296.

[141] E. Radvanyi, E. De Vito, W. Porcher, J. Danet, P. Desbois, J.-F. Colin, S.J.S. Larbi. Study of lithiation mechanisms in silicon electrodes by Auger Electron Spectroscopy. Journal of Materials Chemistry A 1 (2013), 4956-4965.

[142] C. Pereira-Nabais, J. Światowska, A. Chagnes, F. Ozanam, A. Gohier, P. Tran-Van, C.-S. Cojocaru, M. Cassir, P. Marcus. Interphase chemistry of Si electrodes used as anodes in Li-ion batteries. Applied Surface Science 266 (2013) 5-16.

[143] H. Li, X. Huang, L. Chen, G. Zhou, Z. Zhang, D. Yu, Y.J. Mo, N. Pei. The crystal structural evolution of nano-Si anode caused by lithium insertion and extraction at room temperature. Solid State Ionics 135 (2000) 181-191.

[144] U. Kasavajjula, C. Wang, A.J. Appleby. Nano- and bulk-silicon-based insertion anodes for lithium-ion secondary cells. Journal of Power Sources 163 (2007) 1003-1039.

[145] S.P.V. Nadimpalli, V.A. Sethuraman, S. Dalavi, B. Lucht, M.J. Chon, V.B. Shenoy, P.R. Guduru. Quantifying capacity loss due to solid-electrolyte-interphase layer formation on silicon negative electrodes in lithium-ion batteries. Journal of Power Sources 215 (2012) 145-151.

[146] P. Allongue, C. Henry de Villeneuve, J. Pinson, F. Ozanam, J.-N. Chazalviel, X. Wallart. Organic monolayers on Si(111) by electrochemical method. Electrochimica Acta 43 (1998) 2791-2798.

[147] S. Fellah, F. Ozanam, J.-N. Chazalviel, J. Vigneron, A. Etchebery, M. Schakovsky. Grafting and polymer formation on silicon from unsaturated Grignards: I- Aromatic precursors. The Journal of Physical Chemistry B 110 (2006) 1665-1672.

[148] S. Fellah, F. Ozanam, J.-N. Chazalviel, J. Vigneron, A. Etchebery, M. Schakovsky. Grafting and polymer formation on silicon from unsaturated Grignards: II- Aliphatic precursors. The Journal of Physical Chemistry B 111 (2007) 1310-1317.

[149] L.R. Tessler, I. Solomon. Photoluminescence of tetrahedrally coordinated a-$Si_{1-x}C_x$:H. Physical Review B 52 (1995) 10962-10971.

[150] N.J. Harrick. Internal Reflection Spectroscopy. Harrick Scientific Corporation, Ossining, New York, 1979.

[151] F.M. Mirabella Jr., N.J. Harrick. Internal Reflection Spectroscopy, Review and Supplement. Harrick Scientific Corporation, Ossining, New York, 1985.

[152] F.M. Mirabella Jr. Internal Reflection Spectroscopy, Theory and Applications. Marcel Dekker, Inc. New York, 1993.